Geophysical Processing with dense arrays in passive and active seismic configurations

Malgorzata Chmiel

Communauté
UNIVERSITÉ Grenoble Alpes

THÈSE

Pour obtenir le grade de

DOCTEUR DE LA COMMUNAUTÉ UNIVERSITÉ GRENOBLE ALPES

Spécialité : **Sciences de la Terre et de l'Univers et de l'Environnement** Arrêté ministériel du 25 mai 2016

Préparée au sein de **l'Institut des Sciences de la Terre (ISTerre)**
et de l'école doctorale **Terre, Univers, Environnement**

Traitement de données géophysiques en réseaux denses en configuration sismique passive et active

Présentée par

Małgorzata Chmiel

Thèse dirigée par **Philippe Roux, Directeur de Recherche CNRS**

Thèse soutenue publiquement le **2 mars 2017**,
devant le jury composé de :

Jean Virieux	Professeur	l'ISTerre, Grenoble	Président
Philippe Roux	Directeur de Recherche CNRS	l'ISTerre, Grenoble	Directeur de thèse
Alessia Maggi	Professeure	Univeristé Strasbourg	Rapporteur
Sébastien Chevrot	Directeur de Recherche CNRS	Université Toulouse	Rapporteur
Nikolai Shapiro	Directeur de Recherche CNRS	IPGP	Examinateur
Lapo Boschi	Maître de Conférences HDR	UPMC, Paris	Examinateur
Philippe Herrmann	Vice-Président de la Technologie	CGG, Massy	Examinateur
Thomas Bardainne	Chercheur Senior en Géophysique	CGG, Massy	Examinateur

Abstract

Title: Geophysical processing with dense arrays in passive and active seismic configurations.

In geophysics, spatially dense arrays enhance the spatial and frequential characterization of the various waves propagating in the medium. Of course, surface array is subject to strong surface waves. Surface waves highly impact the processing of geophysical data acquired at ground level. They can be considered as noise and subject to suppression as they mask sub-surface information. However, they can be useful for near-surface imaging if they are well retrieved. In any case, their characterization is crucial in active and passive exploration geophysics.

In passive microseismic monitoring, ambient surface noise consists of surface waves. The main goal of passive monitoring is to minimize the impact of surface waves on the actual microseismic data. The strong ambient surface noise lowers the sensitivity and the efficiency of detection and location methods. Moreover, current location and detection methods usually require strong a priori information (e.g., a velocity model or a template).

Active sources generate strong surface waves. In active seismic, current processing strategies often consist in manually picking surface wave arrivals in order to use or remove them. This is often a complex, time consuming, and an ambiguous task. However, it is needed for near- and sub-surface imaging. Surface waves can be particularly difficult to retrieve in sparse arrays.

We propose to apply the techniques of interferometry and beamforming (Matched Field Processing in particular) in the context of dense arrays. High trace density opens new possibilities in geophysical processing in both passive and active surveys. We show that the ambient noise can be explored in the case of microseismic monitoring to extract important information about the medium properties. Moreover, we develop a denoising approach to remove the noise sources at the surface and detect the microseismic event. Furthermore, we propose an automatic detection and location method with a minimum a priori information to retrieve the distribution of heterogeneities in the reservoir, in the well vicinity.

In active survey, we propose an interferometric, automatic approach to characterize the surface waves. We retrieve phase-sensitivity kernels of surface waves between any two points of the acquisition. These kernels are consequently used to obtain multi-mode dispersion curves. These dispersion curves make it possible to separate different modes of surface waves and provide near-surface information if inverted.

The above presented methodologies benefit from spatially dense arrays. Dense arrays of sources or receivers enable alternative, innovative applications in geophysical processing.

Résumé

En géophysique, les réseaux denses améliorent la caractérisation spatiale et fréquentielle des différents types d'ondes dans le milieu. Bien entendu, l'acquisition en surface est sujette aux ondes de surface qui sont très fortes. Les ondes de surface ont un fort impact sur les données géophysiques acquises au niveau du sol. Elles peuvent être considérées comme du bruit et être sujettes à la suppression puisqu'elles cachent l'information de sous-surface. Cependant, elles peuvent être utiles pour l'imagerie de proche surface si elles sont convenablement récupérées. Dans tous les cas, leur caractérisation est cruciale en géophysique d'exploration active et passive.

Dans la surveillance microsismique passive, le bruit de surface ambiant est composé d'ondes de surface. L'objectif principal de la surveillance passive est de minimiser l'impact des ondes de surface sur les données microsismiques. Le fort bruit de surface diminue la sensibilité et l'efficacité des méthodes de détection et de localisation. De plus, les méthodes actuelles de localisation et de détection nécessitent généralement la connaissance d'informations telles qu'un un modèle de vitesse ou un modèle d'événement.

Dans la sismique active, de fortes ondes de surface sont générés par des sources actives. Les stratégies actuelles de traitement sont généralement basées sur une sélection manuelle des ondes de surface afin de choisir lesquelles garder. Il s'agit là d'une tâche complexe, coûteuse et sujette à interprétation. Cependant, cette tâche est nécessaire pour l'imagerie de proche-surface et de sous-surface. Les ondes de surface peuvent être particulièrement difficiles à récupérer dans des acquisitions clairsemées.

Nous proposons d'appliquer les techniques d'interférométrie et de formation de voies (telles que le Matched Field Processing) dans le contexte des réseaux denses. Une densité de traces importante ouvre de nouvelles possibilités dans les traitements géophysiques, qu'ils soient actifs ou passifs. Nous montrons que le bruit ambiant peut être utilisé dans le traitement microsismique pour extraire des informations importantes sur les propriétés du milieu. De plus, nous développons une approche de débruitage qui permet de supprimer les sources de bruit à la surface et détecter les événements microsismiques. Nous proposons également une méthode automatique de détection et de localisation qui se base sur une quantité minimale d'information préalable qui permet de récupérer la distribution des hétérogénéités du réservoir, dans le voisinage du puits.

En ce qui concerne la sismique active, nous proposons une approche interférométrique et automatique de caractérisation des ondes de surface. Nous récupérons les noyaux de sensibilité de phase des ondes de surface entre deux points quelconques de l'acquisition. Ces noyaux de sensibilité sont par conséquent utilisés pour obtenir les courbes de dispersion multimodales. Ces courbes de dispersion permettent la séparation des différents modes des ondes de surface, et fournissent l'information de proche surface suite à une simple inversion.

Le réseau dense permet l'amélioration des méthodes présentées ci-dessus: elle permet des applications alternatives et innovantes dans le traitement du signal géophysique.

Dziękuję! Merci! Thank you!

I would like to thank my advisor Philippe Roux for his support, dynamism, enthusiasm and a clear scientific vision. Thanks to him, I enjoyed and appreciated a lot the three years of my PhD.

I would also like to thank my supervisors from CGG: Thomas Bardainne and Philippe Hermann for their help, reactivity and valorising scientific and technical advice during my PhD. Working in two different environments: CGG and ISTerre was an enriching experience and a great pleasure.

I would like to thank the rest of the Land Team in CGG. In particular, I would like to thank Baptiste Rondeleux, Philippe Feugère, Anne Berthaud, Paul Hardouin, Thomas Bianchi, Kaelig Castor, Mattheiu Guillouet, Julien Cotton, Eric Forgues, Benoit De Cacqueray and Laurie Delmas and the others for their kindness, scientific and technical help. Moreover, a big thanks to the "équipe de sportifs" for all the push-ups and pull-ups done together. It helped me a lot to get through the last months of my PhD.

A big thanks to ISTerre PhD students, in particular to Caro and Ana, my office-mates and my flat-mates, without whom Grenoble would not be such an enjoyable experience during my PhD years.

A special thanks to my jury, in particular the reviewers Alessia Maggi and Sébastien Chevrot, for their valuable comments that helped to improve this PhD.

Last, but not the least I would like to thank my Mum and my Sister for their great support in all the possible ways during my PhD. I would like to also thank my partner and his family for their support. Finally, a big thanks to my friends from Poland who were always supporting me no matter the distance.

Contents

List of Figures

List of Tables

Introduction

Presented works were carried out under the CIFRE convention (Conventions Industrielles de Formation par la Recherche). The idea of a contract CIFRE is to bring together "scientific and business thinking" by involving into a research project a company and a public laboratory. This PhD is a result of a cooperation between the company CGG (Compagnie Générale de Géophysique) and the Institute of Earth Sciences (ISTerre) in Grenoble.

The main activity of CGG is based in exploration geophysics. Exploration geophysics is a natural science, in which physical principles are applied to the search or evaluation of natural resources. CGG cartographies the subsoil to localize the natural resources via acquisition and imaging. This allows to better understand the complexity of the subsurface. The activity of CGG is concentrated on geology and geophysics, characterization and development of reservoirs. Two types of seismic acquisitions are used in CGG (Figure 1): passive seismic configurations which use uncontrolled sources (those who are present in the environment) and active configuration with controlled sources (such as vibro-truck).

a) Passive Seismic: Well Pad

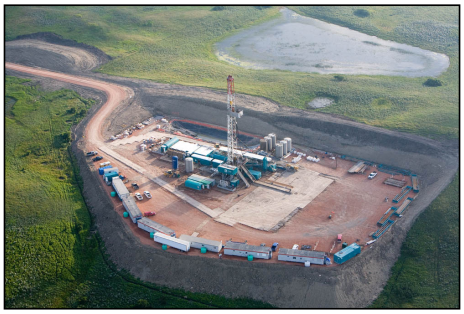

b) Active Seismic: Vibro-Truck

Figure 1: a) An example of a source of noise on a microseismic monitoring field: well-pad (the head of the well stimulated during this monitoring period) is one of the busiest/ "noisiest" spots on a field (picture from http://thebakken.com/). b) Seismic vibrator is a truck that generates low-power, long signal (courtesy: CGG).

A special case of the passive seismic is a microseismic monitoring of hydraulic fracturing operations. Hydraulic fracturing (in petroleum or geothermal reservoirs) is an intended dislocation of low permeability geological formations to increase their permeability and to make accessible natural resources such as shale gas. Hydraulic fracturing can be done using vertical, horizontal and inclined wells. First, rock is perforated with a perforation shot, next the fracking fluid is injected under high-pressure into formation to open more the pre-existing fractures and to create the new ones. These operations create fractures in rocks, which changes the local stress field and result in microseismic activity. The micro-cracks are destabilized and slip, which emits mechanic waves (P- and S-waves).

Microseismic monitoring from the surface consists of recording seismic waves in real time to determine information about the distribution of heterogeneities of the mechanical properties of the subsurface. A micro-seismic monitoring might ease the understanding of the position and the orientation of the fractures and also the underground field stress in general. It is used to optimize the exploration and to increase the productivity of the reservoir. The pressure on the wellhead can be adjusted as a function of the response of the sub-surface. An inversion process allows determining in a relatively reliable way the position, source mechanism of the fracture and the magnitude of the microseismic event.

There are a few challenges in microseismic monitoring from the surface. First, the position of the microseismic events is unknown. They need to be detected and localized. Due to cost considerations, when performing a monitoring of microseismicity from the Earth's surface, at the difference of downhole or sparse networks, only vertical sensors are generally deployed. This leads to the general use of P-waves in surface microseismic monitoring and in consequence an important incertitude of localizations at depth. Second, the surface ambient noise is stronger than the microseismic signal coming from the reservoir. Often, the information coming from the subsurface is masked by the strong surface noise. The origin of the noise can be natural (e.g.: wind) and anthropogenic (e.g.: road traffic). Figure 2a presents a strong microseismic event recorded on a set of 17 arrays of 48 receivers (794 receivers). Strong surface waves are recorded together with an actual microseismic signal. We may distinguish different noise sources. These can be located at the surface (e.g.: anthropogenic sources: road traffic, surface installations; or natural sources such as wind or at depth (e.g. downhole noise: microseismic events, signals emitted by the hydraulic fracturing operations, gas bubbles). Noise sources play an important role in passive seismic.

Strong surface ambient noise lowers signal to noise ratio of the recorded microseismic data and traditional location methods based on the first arrivals cannot be applied. Moreover, the absolute locations need an accurate velocity model to provide a correct position and time of origins of microseismic events. However, introducing a relative location might ease some issues. In case of location using only P-waves and relative location algorithms, it is possible to find a reliable event position while using a homogeneous velocity model. However, this location is

achieved with a false time of origin and with a significant vertical uncertainty. Moreover, a priori information might be needed (e.g.: a template - a pointed perforation shot or a pre-localized microseismic event). Also, existing methods often require a manual screening of detections in order to check their reliability and remove false detections.

Additionally, the process of hydraulic fracturation is quite controversial. It has been shown that sometimes hydraulic fracturing can caused unwanted side effects, such as an increase of the seismicity or environmental pollution in the area. Moreover, hydraulic fracturing in shale gas applications is still technically challenging. These are the reasons why it has been banned or not performed in many countries.

Subsurface information can also be gathered from active seismic experiments. Active seismic prospecting is based on the classical physical principles of reflection, refractions, transmission, and scattering of elastic waves in a layered solid half-space. In general, it consists of generating elastic waves by near-surface active sources (hammers, explosions, vibrator trucks) to record the created waves at the surface or in boreholes. Using different offsets, we may deduce the positions of refracting and reflecting interfaces by analyzing the travel times and identifying characteristic wavelets (Ewing and Press (1956)). This prospection is crucial in characterizing reservoirs of natural sources and optimizing their exploration.

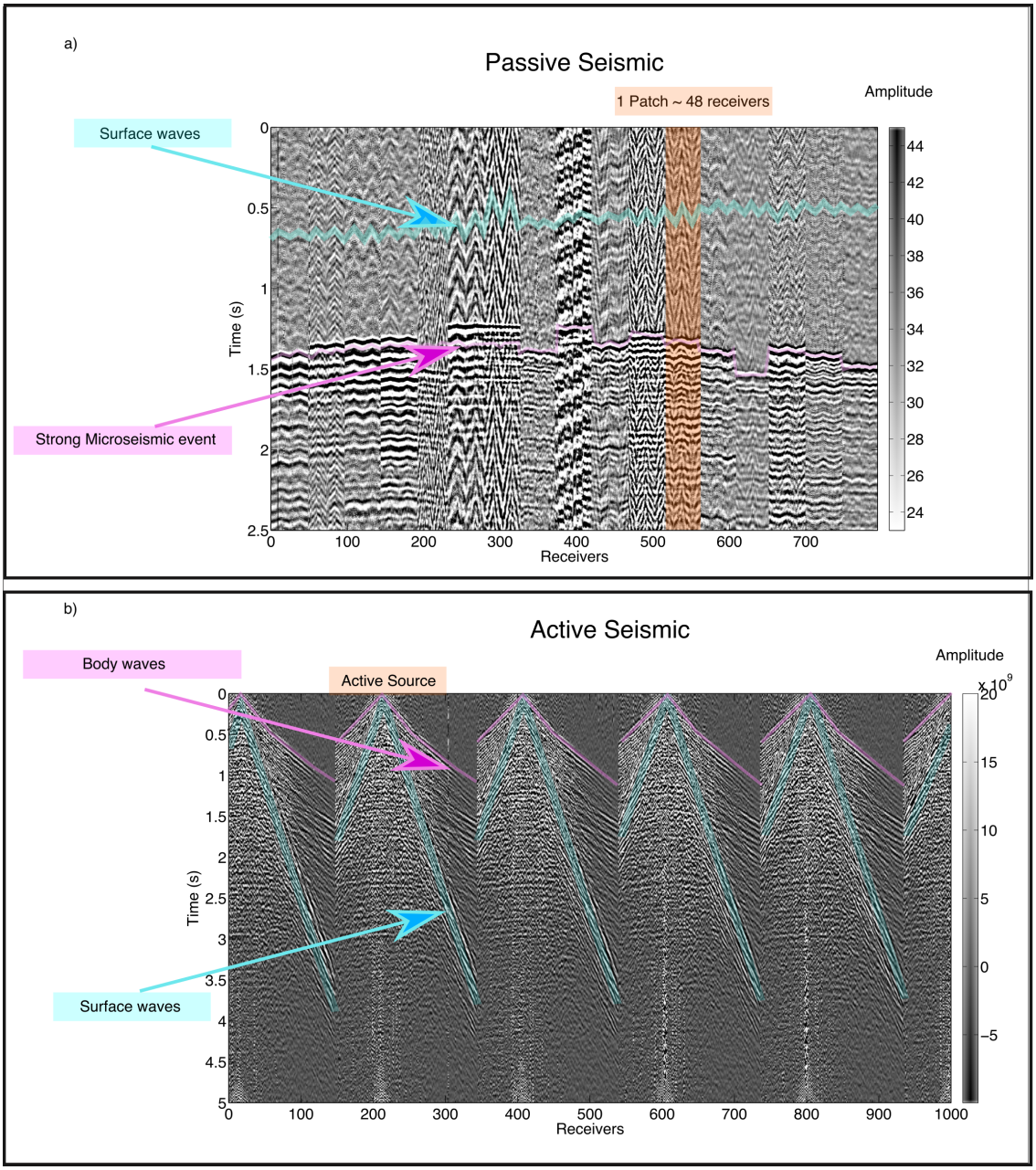

Figure 2: a) Passive seismic data: a strong microseismic event recorded on a set of 17 patches (794 receivers). b) An extract of active seismic data: source gather recorded on 1000 receivers.

Active sources (shots) generate not only body waves, but also near surface contaminations. Highly energetic surface waves (also called ground-roll) are the most important shot-generated noise. Often they are the strongest arrivals in active-seismic data. As in passive seismic, one component vertical sensors are usually used in active seismic. It means that the most common surface waves are the Rayleigh waves and they are considered to be noise. Different methods

are used to minimize the impact of the noise wavefield, depending on its properties. Figure 2b presents data generated by an active source and recorded on 1000 receivers (receivers are places in parallel lines). The shot generated wavefield is made of direct and back-scattered ground roll. The direct arrivals of surface waves can be explored with interferometry.

Of course, surface waves can also provide important information about the shallow structures. Phase- and group- velocities maps in a given frequency range can be inverted to obtain S-wave (sometimes P-wave) velocity models for the near surface. This can add more constraints to seismic migration and improve its results. However, obtaining the phase- and group- velocities maps for surface waves can be challenging. Many algorithms and acquisition strategies have been developed in order to extract them or use them more efficiently. Naturally, the optimal algorithms are the ones that provide high quality results in an automatic way.

Both passive and active methods are essential in exploitation of unconventional reservoirs. The optimal design of seismic surveys is crucial. Many studies have shown that the densier the acquisition the better the illumination of the sub-surface and the higher the signal-to-noise ratio after the application of stacking algorithms (Wombell et al. (2009), Pastori et al. (2016)). Dense seismic designs increase the geophysical value of data.

Since a few years, new methods started to appear in the academical environment. The methods which are based on the correlation of two signals. Different studies shown the possibility of use the correlation to extract important information about the medium.

It has been shown that it was possible to determine the Green's function between two sensors in the medium with noise cross-correlations (e.g.: Shapiro et al. (2005)) to image the Earth's structure. However, the wavefield responses between sensors can be constructed also using cross-correlations and active sources. This technique of creating coherent signals from a set of seismic recordings is called seismic interferometry. The technique of interferometry can be applied with active and passive sources. In both cases, the position of sources plays an important role in retrieving the Green's function between sensors through seismic interferometry. The equipartition criterion needs to be fulfilled which requires a regular and dense source distribution. However, even if the noise source distribution is not uniform and the noise correlation does not allow the extraction of the exact Green's function, it can provide results that are of significant physical importance through the reconstruction of specific arrivals (Sanchez-Sesma et al. (2006)). Still, the most fundamental thing is to locate and detect noise sources both at the surface and at depth in order to remove them or explore them. Another correlation based method (Matched Field Processing) was used to localize noise sources (Vandemeulebrouck et al. (2013)).

In active seismic, the direct arrivals of surface waves can be explored with interferometry. They origin from controlled sources, what gives more possibilities when it comes to interferometry. Their position and their time zero are known; also their density is important. These sources enable the recovery of the surface wave Green's function between two points using either correlation or convolution. Yet, the main contribution to interferometrically reconstructed inter-receivers

Green's function comes from stationary phase zone (two cones around extensions of the line that connects the two receivers).

Another studies that shown the extraction of physical information using correlation were conducted in ISTerre (Roux et al. (2013)). For example, some experiments in the laboratory shown the possibilty of extracting an empirical sensitivity kernel. This kernel is based on the product of the Green's function in the frequency domain (correlation or convolution) and it gives the propagation model of the waves in the acoustic medium.

The aim of this PhD is to explore the method based on correlations that have been developed in the academical environment to envisage the industrial challenges in the context of spatially dense networks. High trace density opens new possibilities in geophysical processing in both passive and active surveys.

We will focus on the exploration geophysics issues such as: localization of noise source, wave separation (signal from noise), near surface characterization, image in low frequencies. We investigate the use of the academical methods and expertise such as: localization of noise sources with beamforming (Matched Field Processing in particular), surface wave tomography from ambient noise with cross-correlations functions and imaging of the medium with sensitivity kernels.

This work consists of two parts: 1. Processing passive seismic data (Chapter 1 and Chapter 2), and: 2. Processing active seismic data (Chapter 3 and Chapter 4) in exploration geophysics with dense arrays.

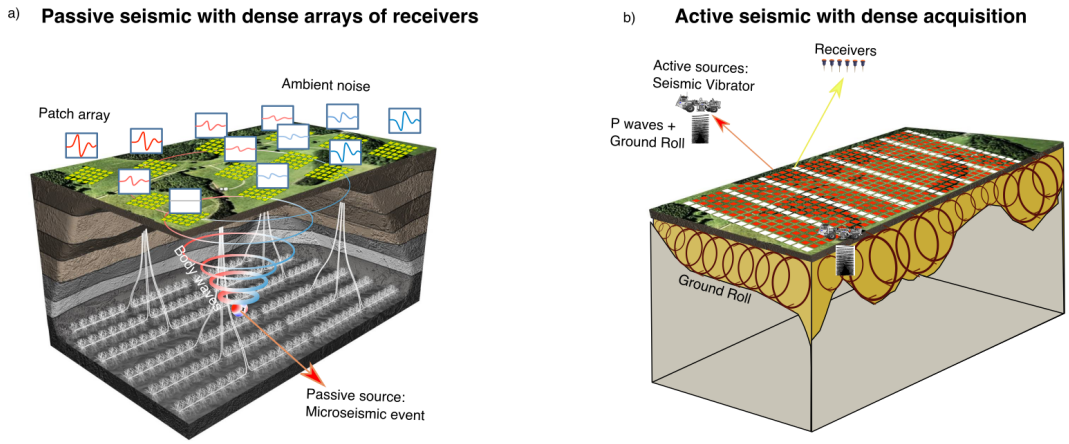

Figure 3: Dense acquisitions in exploration geophysics. a) Passive microseismic monitoring of hydraulic fracturing with patch arrays. b) Active seismic survey with "carpet shooting".

The first part focuses on passive seismic monitoring with patch acquisition. Patch design is

an aggregation of dense sub-networks (Figure 3a).

- Chapter 1 focuses on noise sources on the surface. A multi-scale methodology is presented to detect and locate surface noise sources while using array-processing methods. These surface noise sources allow retrieving local phase- and group- velocity maps of Rayleigh waves in an automatic way.

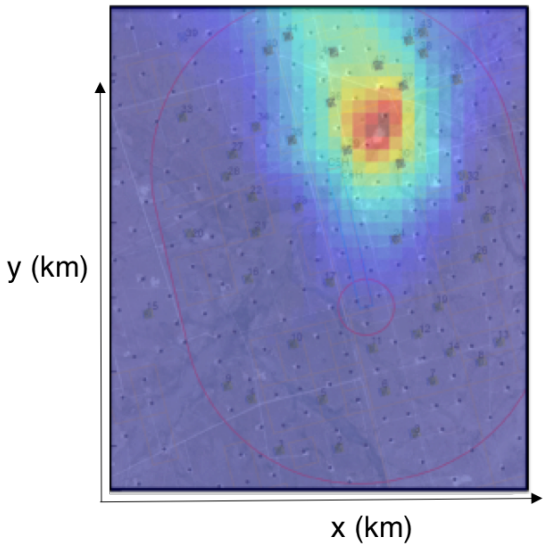

Figure 4: Tomography inversion for group velocities together with local phase velocities per patch obtained from the MFP in the 5 Hz to 7 Hz frequency range.

- Chapter 2 discusses the separation between the sources at the surface and at depth. Two approaches are considered: a suppression of surface waves and an automatic location of noise sources at depth with minimum information a priori.

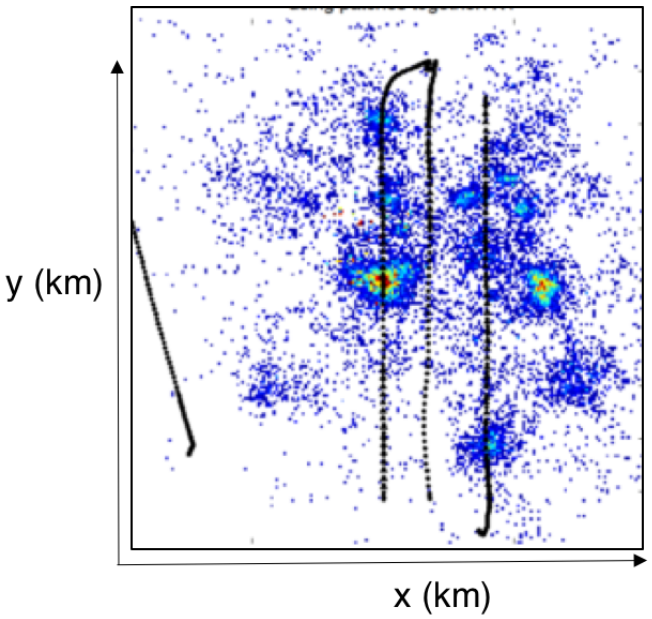

Figure 5: Detection and location using 17 patches with a homogenous velocity model and the Bartlett algorithm: horizontal view.

The second part describes a dense active seismic acquisition. The sources spacing is the same in both X and Y directions (which is known as a ”carpet shooting”) and the receivers are placed along parallel lines (Figure 3b).

- Chapter 3 presents different approaches for the stationary phase zone definition. It focuses mostly on phase sensitivity kernels. The phase sensitivity kernels are respectively extracted from correlations and convolutions. This chapter also investigates the convolutional and correlational approaches to retrieve the Green’s function.

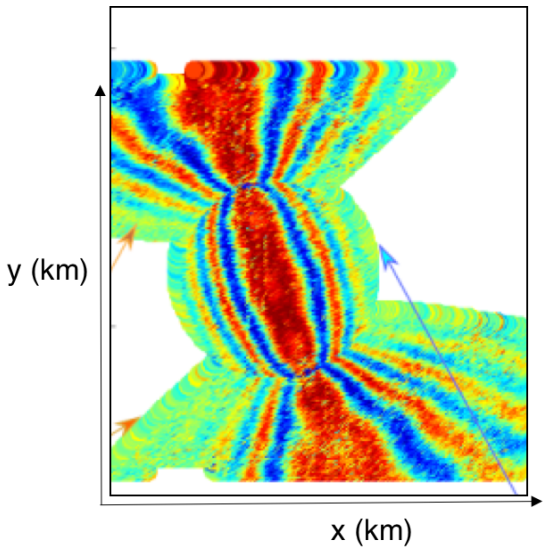

Figure 6: Data-based sensitivity Kernels from correlations and convolutions for two receivers (distance 2900 m) in the frequency (2-4) Hz.

- Chapter 4 introduces hyperbolic and ellipsoid transforms that are applied to data-based phase sensitivity kernels. It results in high-quality, phase velocity dispersion relation analysis of multimode Rayleigh waves between two points. Potential application to surface wave modes separation is also envisaged.

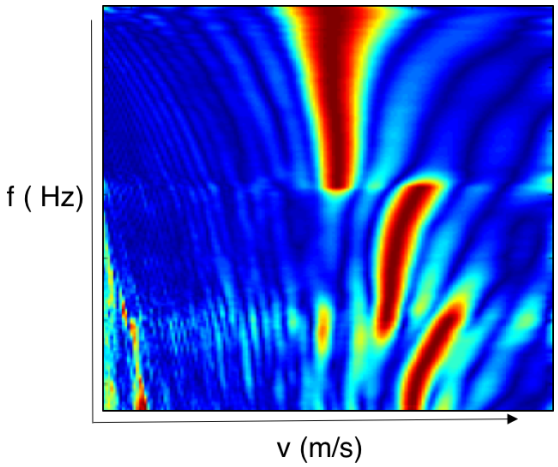

Figure 7: Dispersion relation analysis from correlation and convolution calculated with hyperbolic and ellipsoid transforms.

In the end, the results and methodologies are discussed and perspectives for future works are given.

Chapter 1

Extraction of phase and group velocities from ambient surface noise in a patch-array configuration.

This chapter is a retranscription of an article published during my PhD in Geophysics (Chmiel et al. (2016)). This article presents a multi-scale approach to retrieve local phase velocities and group velocities of surface waves using patch array acquisition.

1.1 Abstract

We investigate the use of ambient-noise data to extract phase and group velocities from surface-noise sources in a microseismic monitoring context. The data were continuously recorded on 44 patch arrays with an interpatch distance of the order of 1 km. Typically, a patch-array design consists of a few tens of patches each containing 48 strings of 12 single-vertical-component geophones densely distributed within the patch area. The specificity of the patch-array design allows seismic analysis at two different scales. Within each patch, highly coherent signals at small distances provide phase information at high frequency (up to 10 Hz), from which surface-wave phase velocities can be extracted. Between the pairs of patches, surface-wave group velocity maps can be built using correctly identified and localized surface-noise sources. The technique can be generalized to every patch pair using different noise sources identified at the surface. We note that incoherent but localized noise sources accelerate the convergence of the noise-correlation functions. This opens the route to passive seismic monitoring of the near surface from repetitive inversion of phase and group velocity maps.

1.2 Introduction

At typical seismic exploration frequencies (i.e., 1-60 Hz), ambient seismic noise can often be dominated by local anthropogenic noise sources. For example, stimulation of a hydrocarbon reservoir with hydraulic fracturing (injection of high pressure fluid into low permeability reservoirs as described in Evans (1966)) results in microseismic activity and strong surface noise propagation. Historically, downhole geophone tools have been used to monitor microseismic activity during stimulation programs (Rutledge and Phillips (2003)). However, in the past 10 years, we have seen the advent of dense surface networks to record the growth of hydraulic fractures. Moreover, it gives an opportunity to explore noise sources on the Earth's surface and surface waves recorded by these networks.

Together with the development of microseismic surface monitoring, some questions have arisen about the optimal design for surface acquisition (e.g., Hallo (2012)). Recently, a new deployment method of sensors at the surface using multiscale array designs has been proposed (Roux et al. (2014)). Receivers are located in dense patches that are sparsely distributed over the study area. Deployment of sensors at the surface using a patch-array design opens the route to alternative studies based on ambient surface-noise recording. Indeed, different surveys have demonstrated the possibility to extract coherent waves from noise signals, and in particular, to obtain the surface-wave contribution to the Green's function between receivers. Many studies have confirmed the utility of seismic noise for the investigations of the Earth interior at different scales both in time and space (e.g., Shapiro and Campillo (2004); Shapiro et al. (2005); Sabra et al. (2005); Brenguier et al. (2007)).

Undoubtedly, the distribution of noise sources has an important role in noise-correlation processing. At low frequencies (i.e., <1 Hz), the noise is dominated by natural sources (Campillo et al. (2011)). Various surveys have demonstrated that the distribution of natural noise sources becomes sufficiently isotropic with long-term averages of successive time windows. However, this averaging is needed over long periods of time (i.e., from a few months to a few years) to converge toward the Green's function and to perform surface noise tomography (e.g., Lin et al. (2007)).

In the most general case, the convergence of the noise correlation to the Green's function requires a fully random wavefield (Weaver (2005)). This condition is fulfilled by the equipartition regime of the diverse components of the elastic field, or by the presence of equally distributed random-source fields (Larose et al. (2004); Snieder (2004); Sabra et al. (2005); Weaver and Lobkis (2005)). In the simplest case, sources aligned with the receiver direction (i.e., sources at stationary-phase locations) give the same result (Roux and Kuperman (2004)). However, even if the noise distribution is not uniform and the noise correlation does not allow the extraction of the exact Green's function, it can provide results that are of significant physical importance through the reconstruction of specific arrivals (Sanchez-Sesma et al. (2006)). In the hydrocarbon

production context, data recording is often limited to a few days, although with a large number of sensors. This provides new possibilities for the use of noise cross-correlations to image the shallow subsurface or to monitor changes in the medium. Hohl and Mateeva (2006) demonstrated that reflectivity imaging with noise from a single line of ocean-bottom cable data is feasible in seismic exploration applications. Also, Bussat and Kugler (2011) and de Ridder and Dellinger (2011) were one of the firsts to perform ambient seismic field noise-correlation tomography for seismic exploration applications, from dense ocean-bottom recording networks. However, at typical seismic exploration frequencies (i.e., 1-60 Hz), ambient seismic noise can often be dominated by local anthropogenic coherent or incoherent sources (e.g., Olofsson (2010)). In this case, the reconstruction of the Green's function from ambient noise cannot be generalized due to the local and non-stationary character of anthropogenic noise sources. However, localized noise sources at the surface that create directive noise can also be explored with the concept of passive seismic-noise tomography (Roux (2009)), where they can be used to construct a velocity model map for S-waves (Mordret et al. (2013)).

Patch-array design allows array-processing techniques such as matched field processing (MFP) (Kuperman and Turek (1997)) to localize noise sources at the surface. This approach has been shown to be efficient in ocean acoustics for decades, and has found a recent application in monitoring geyser activity (Cros et al. (2011); Vandemeulebrouck et al. (2013)), while it has also been applied to passive monitoring in the context of oil and gas production (Corciulo et al. (2012)).

In the framework of surface geophone deployment using a patch-array design for microseismic monitoring purposes, we have used the available data for an alternative study that is based on ambient surface-noise tomography. In this study, we present a methodology to use directional seismic noise on a collection of patch arrays, from which local phase velocities and group-velocity maps for Rayleigh waves using short time windows (i.e., 15 min) are obtained in an automatic way. The specificity of the patch-array design is to allow seismic analysis at two different scales. Within each patch, highly phase-coherent signals provide phase information at short distances and high frequencies (i.e., up to at least 10 Hz), from which local surface-wave phase velocities can be extracted. Between two patches, there is still strong coherence at lower frequencies (i.e., up to at least 7 Hz), from which surface-wave group-velocity maps can be built.

The main goal of this study was to provide combined maps of group and phase velocities for surface waves from ambient-noise recordings in a seismic exploration context. The separate measurement of both local phase-velocity maps and group-velocity maps provides the local dispersive behavior in the propagation medium. Having both group- and local-phase velocity information in the area of interest allows us to better constrain the inversion of surface waves at depth, and to obtain more accurate S-wave velocity models. Although phase and group velocities can be deduced one from the other, the simultaneous inversion of these two velocities place tighter constrains on the possible models than those from the inversion of either alone. If phase and group velocities are measured differently, the error processes in the measurements are largely indepen-

dent (Shapiro and Ritzwoller (2002)). Potential applications to time-evolving static corrections can also be envisaged, as surface-wave inversion can be performed using local sources over short periods of time.

In the following, we describe the patch-network deployed above a hydrocarbon reservoir, and we analyze the data over 5 days of continuous recording. We present a description of matched field processing (MFP), and in particular, of the minimum variance distortionless response (MVDR). Then, we propose two workflows: 1) using phase information obtained through the MFP technique, we retrieve the local phase velocity per patch, and we localize the dominant noise sources at the surface; 2) using the set of previously located noise sources, we obtain the group velocities between patches.

1.3 Ambient-noise source localization

In this study, we use data from the monitoring of shale-gas hydraulic fracturing that were acquired using a patch-array design, with 44 patches sparsely distributed over an area of 48 km2, for a total of 2087 individual traces. Typically, a patch-array design consists of a few tens of patches. Each patch consists of 48 groups of 12 single-vertical-component geophones densely distributed within the patch area. The records from the 12 geophones are stacked to increase the signal to noise ratio at every receiver station (i.e., the output from each patch is 48 traces). In this survey a typical patch had 4 receiver lines, 36 m apart, with 12 receiver stations per line, 12 m apart inline, for a total patch size of 108 m x 132 m (Figure 1.1). The average distance between two patch arrays was around 1 km.

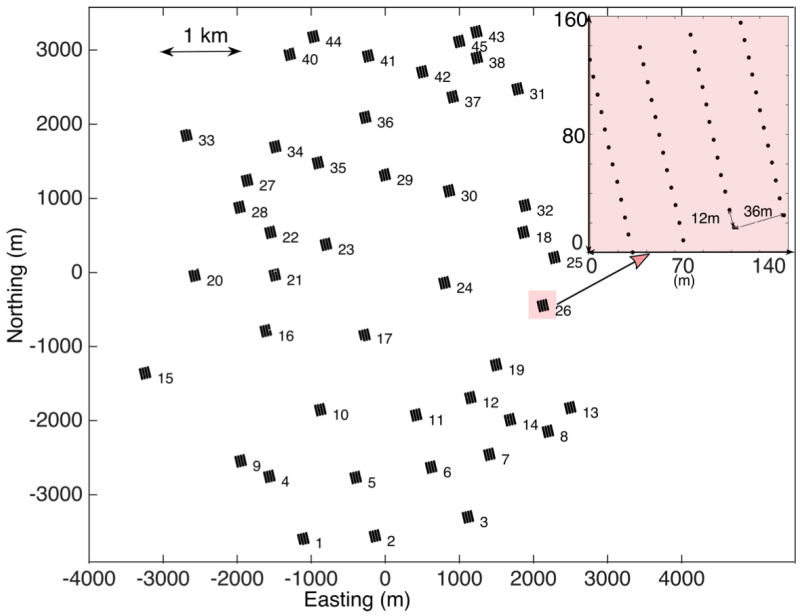

Figure 1.1: Experimental configuration with a set of 44 patches designed for microseismic monitoring over a 42-km2 area in Texas, USA. The average distance between neighboring patches was 1 km. The x-y coordinates are relative to the center of the network. The red box (top right) shows a close-up of the receiver distribution within patch number 26. The in-line distance between receivers was 12 m and 36 m in the cross-line direction for a total of 48 receivers on 4 lines of 12 receivers each. Each receiver is, in fact, a sum of 12 tightly clustered vertical geophones.

1.3.1 Matched Field Processing – theory

Matched field processing is an array-processing method that was developed to localize low-amplitude quasi-monochromatic sources in the context of ocean acoustics (Kuperman and Turek (1997)). MFP is the generalization of the traditional plane-wave beamformer (Jensen et al. (2011)) that can be applied to any complex medium, as long as spatially coherent phase information can be extracted between near-by sensors. In practice, using coherent signals recorded by an array of receivers, the phase delays between sensors are matched to a set of model-based Green's functions. These are calculated from "trial source" locations on a 2D or 3D spatial grid. MFP produces the probability that a source is present at a given grid location.

Matched field processing has found recent geophysics applications in different domains, such as geyser activity (Cros et al. (2011)) and microseismic activity (Corciulo et al. (2012)). MFP is particularly suited to seismic data where the noise sources spread and/or overlap in time, which thus prevents unambiguous picking of distinct seismic arrivals.

In this study, we describe an adaptation of this array localization method to isolate surface-noise sources that are mostly due to human or industrial activities. In the most general case, the time-domain data vector $\vec{d}(t)$ is recorded by the N receivers $r_1, \ldots, r_N$ within a given array. In

the frequency domain, the phase information at frequency ω is obtained from the complex data vector $\vec{d}(\omega) = (d_1, \ldots, d_N)$ which contains the data amplitude and phase recorded over the *N* sensors within the patch.

In some cases, only the phase of the recorded signal is used. Indeed, the phase is more sensitive than the amplitude when it comes to coherent processing (Jensen et al. (2011)). Normalizing the Fourier component of each sensor by its amplitude is equivalent to giving the same weight to each sensor in the localization process. This is justified in the case of short arrays with high coherence, as will be demonstrated for signals recorded within a single patch.

The cross-spectral density matrix (CSDM)

$$K(\omega) = \vec{d}(\omega)\vec{d}^{H}(\omega) \tag{1.1}$$

where *H* is the Hermitian transpose (the conjugate transpose), captures the relative spatial phase difference between the sensors. Using one noise segment only as described in the equation 1.1, the rank of the CSDM is equal to 1. However, a full-rank CSDM matrix is required to use the adaptive operator (so called minimum variance distortionless response: MVDR), which will be presented in the following. To obtain a full-rank CSDM, the construction of the CSDM matrix is modified according to equation 1.2 as:

$$\bar{K}(\omega) = \frac{1}{M}\sum_{i=1}^{M} \vec{d_i}(\omega)\vec{d_i}^{H}(\omega) = \frac{1}{M}\sum_{i=1}^{M} K_i(\omega) \tag{1.2}$$

where $\vec{d_i}$ is the data vector associated with different noise sub-segments.

Noise sources should be incoherent and stationary between successive noise segments. Note that, in practice, we need a number of noise segments *M* equal at least to twice the number of receivers *N* in the array to produce a full-rank CSDM. Next, we define a modeled Green's function vector $\vec{d}(\omega, a) = (d_1(\omega, a), \ldots, d_N(\omega, a))$ as the wavefield received on the array at frequency ω from the trial point source position a in the medium. In the simplest case, a homogeneous velocity model is used, in which case, the MFP simply reverts to beamforming. In particular, this is sufficient when using low frequencies, because large wavelengths are insensitive to short-scale medium heterogeneities (Shearer (2009)).

The modeled Green's function in a two-dimensional or three-dimensional medium for each element j of the array is given by:

$$d_j(\omega, a) = \exp\left(i\Theta_j(\omega, a)\right) \tag{1.3}$$

where Θ_j is the phase delay between the trial-point source position *a* and receiver r_j. In the case of a homogeneous medium, equation 1.3 becomes:

$$d_j(\omega, a) = \exp\left(\frac{i\omega x_{ja}}{c}\right) \tag{1.4}$$

where *c* is the medium velocity, and x_{ja} is the distance between each receiver position $r_1, \ldots, r_N$ and the trial-point source position *a*.

Of course, more complex Green's functions can be required as forward models, particularly in the case of layered media, as different frequencies sample different depths, and the velocity c in equation 1.4 can vary as a function of the frequency.

To reveal the position of the dominant source, different MFP operators can be used to match the observed CSDM *K* with the model vector $\vec{d}(\omega, a)$. One of these is a linear operator, the Bartlett processor, which is given by:

$$B_{Bartlett}(\omega, a) = \sum_{\omega} |\vec{d}^{H}(\omega, a) K(\omega) \vec{d}(\omega, a)| \tag{1.5}$$

As can be seen in equation 1.5, the Bartlett processor is a product of the modeled Green's function with the CSDM. Physically speaking, the Bartlett processor is equivalent to the cross-correlation between the recorded wavefield and the modeled one. As for any linear-phase-based algorithm, diffraction laws, and thus the wavelength, limit its spatial resolution. However, it behaves as a robust and stable processor for source detection.

Higher spatial resolution can be obtained with adaptive MFP techniques. We refer to these as adaptive because the data processing involves the construction of weight vectors based on the phase coherence of the recorded data. Among these techniques, the minimum variance distortionless response (MVDR) was inspired by Capon (1969). MVDR is based on a maximum-likelihood method for matching vector data with a calculated model (Cros et al. (2011); Corciulo et al. (2012)). This adaptive method is a non-linear processor of the received fields, as it requires CSDM inversion that introduces a phase-sensitive nonlinear factor (Jensen et al. (2011)). The output of the MVDR is given by:

$$B_{MVDR}(\omega, a) = \sum_{\omega} \frac{1}{|\vec{d}^{H}(\omega, a) K^{-1}(\omega) \vec{d}(\omega, a)|} \tag{1.6}$$

Both the Bartlett and MVDR processors produce ambiguity surfaces that show a probability distribution of the noise sources. The area with the maximum amplitude of the ambiguity surface is called the focal spot, as those shown in Figure 1.4. We will elaborate on this in the following sections. Note also that the average over independent frequencies in both processors improves the contrast in the final image.

Matched field processing methods are based on phase-delay measurements, for which spatial coherence is required. Time-frequency spectrograms were calculated and averaged over all of the patches for 24 h (Figure 1.2 a). These show that seismic noise is present in the frequency range < 20 Hz. Figure 1.2b shows an example of a 30-s recording of ambient seismic noise on all of the elements of patch 11.

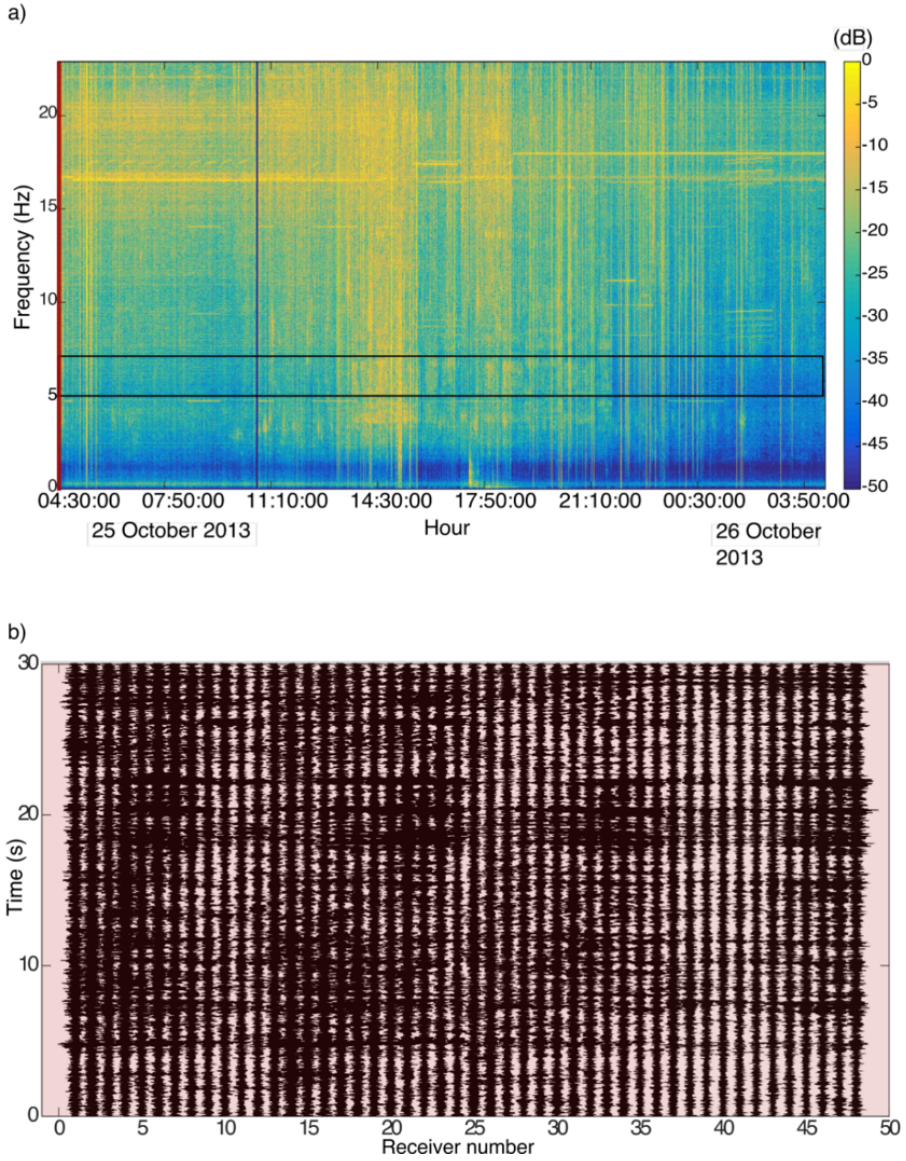

Figure 1.2: (a) Spectrogram of 24 h of data spatially averaged over all of the patches recorded from 05:00 hours on October 25. The color scale represents the normalized spectral amplitude, in dB. The black rectangle demonstrates the frequency band between 5 Hz and 7 Hz. (b) Time recording (30 s) of ambient seismic noise recorded over 1 h for patch 11.

Tests showed that good spatial coherence was observed in the frequency interval from 2 Hz to 15 Hz. However, we restricted this analysis to the frequency band between 5 Hz and 7 Hz. The choice of this frequency band ensures a satisfying balance between the spatial resolution of the MFP output and the robustness of the MFP processor when the homogeneous velocity approximation is applied.

Figure 1.3 shows the spatial coherence in the frequency band between 5 Hz and 7 Hz. Taking

patch 11 as an example, this represents the cross-correlated signals that were recorded for the longest distance between two receivers inside the same patch (interdistance = 173 m) using 3 min of records per hour, successively processed over the 5 days of data recording. The spatial coherence for patch 11 remained stable within one-hour time window over the five days of acquisition. High-amplitude coherence is noticeable, including two anomalous time periods during days 4 and 5.

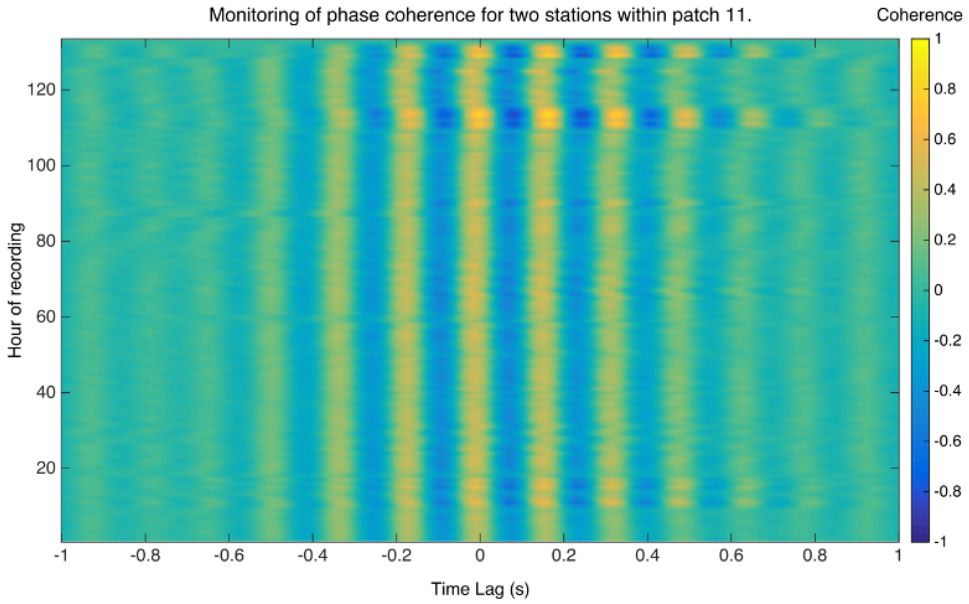

Figure 1.3: Time evolution of the phase coherence calculated over 5 days of data between the most distant receivers within patch 11 (inter-distance, 173 m). The x-axis corresponds to the time-domain correlation using 1 h of ambient noise centered for the frequency band of 5 Hz to 7 Hz. The y-axis shows the time evolution of the noise correlation over 130 h.

1.3.2 Matched field processing – ambiguity maps

To calculate the MFP maps shown in Figure 4, an averaging time window of 15 min was used. To increase the rank of the CSDM, we used 30 subsegments of 30-s duration. For each segment, the individual vector data $\vec{d}(\omega)$ was calculated with the corresponding CSDM, and all of the CSDM K_i were averaged as in 1.2.

The difficulty with all MFP processors is the requirement for a priori knowledge of the velocity model to generate an adequate Green's function. However, we can also say that this adds a degree of freedom to MFP algorithms. We can use the velocity per patch as an independent parameter and optimize it using the output of the Bartlett processor. This velocity is a local phase velocity characterizing the medium properties within one patch. This idea will be developed in the

next section. For now, the MFP is calculated for each patch separately with optimized velocities, which gives one ambiguity surface per patch (Figure 1.4 a-c). These ambiguity surfaces reveal the most probable directions for the surface-noise sources. To find the position of the dominant noise source for all of the patches, all or part of the ambiguity surfaces need to be combined (Figure 1.4 d). This combination is performed by adding (as the arithmetic average for the Bartlett processor) or multiplying (as the geometric average for the adaptive MVDR processor) the MFP maps obtained from each patch separately.

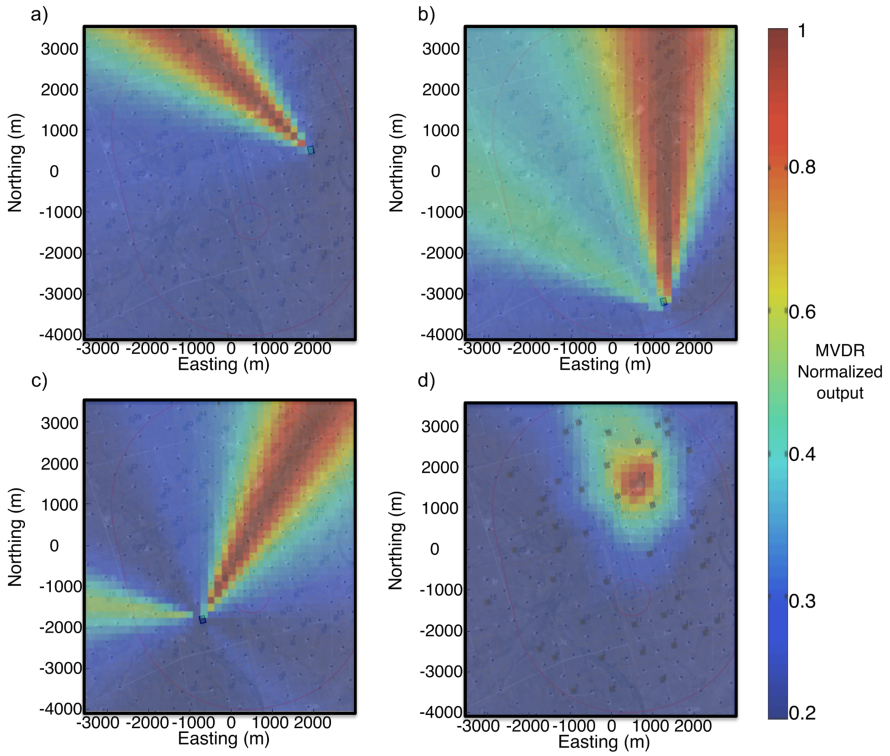

Figure 1.4: Matched field processing results for patches 18 (a), 3 (b), and 10 (c) using the MVDR processor. Each ambiguity map was obtained using a different phase velocity (800 m/s, 1000 m/s, 850 m/s, respectively) in the frequency band of 5 Hz to 7 Hz, and shows the direction of the noise source located at the surface using a single patch for the MFP localization. To further constrain the position of the dominant noise source, a geometrical average was performed on all of the MFP maps for 44 patches (d). The ambiguity maps are superimposed upon aerial views of the field.

Indeed, the linear Bartlett provides an ambiguity surface where the maximum amplitude (between 0 and 1, according to equation 5, as both the CSDM K and the replica vectors are normalized) corresponds to the maximum likelihood of the dominant source. The linearity of the Bartlett processor justifies the use of the arithmetic average as a way to combine ambiguity surfaces from different patches. In the case of the MVDR, the ambiguity maps are multiplied by each other, as their individual amplitudes are arbitrary due to the nonlinear nature of the processor. This geomet-

ric average improves the contrast of the final maps when all of the possible patches are combined. The MFP was applied to the ambient-noise data to monitor the noise-source distribution during the 5 days of recording, using time windows of 15 min in the 5 Hz to 7 Hz frequency band. The duration of this time window was chosen arbitrarily and resulted from a balance between: (1) long time windows, to enhance the coherence between sensors; and (2) short time windows, to limit the drop in the coherence caused by source motion. Obviously, the distribution of the noise sources changes over time. However, it was possible to distinguish repetitive periods with only one dominant noise source (e.g., two examples in Figure 1.5). Note that these noise sources are located within the network area between the patch arrays. The juxtaposition of the MFP maps with an aerial view allows us to identify the dominant noise sources as surface footprints due to human activity. In particular, the position of the main noise source identified in Figure 1.5a corresponds exactly to the head of the well stimulated during this monitoring period.

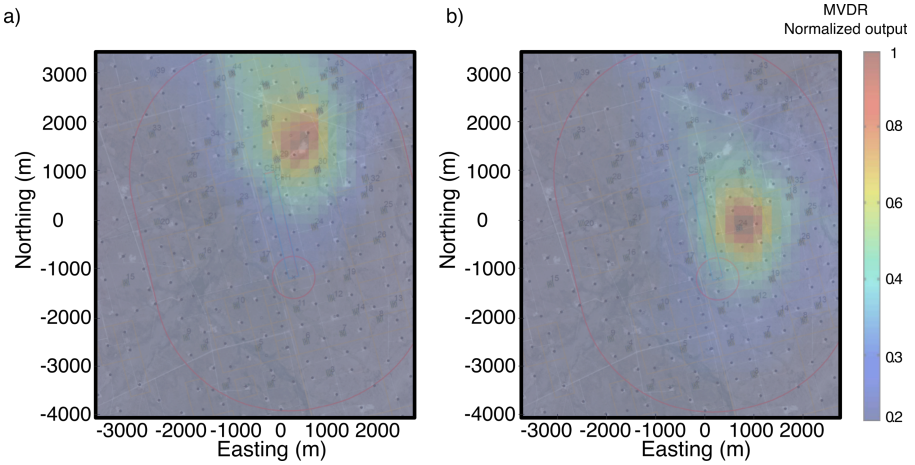

Figure 1.5: Final ambiguity maps obtained from the geometric average performed between all of the patches with the MVDR, for two different 15-min periods of recorded data in the frequency band of 5 Hz to 7 Hz. The MFP amplitudes were normalized by the maximum of the output. The two final ambiguity maps reveal the position of the well pad (a), and traffic in the field (e.g., a truck that circled around one of the well pumps for a few minutes) (b).

1.4 Local phase velocity and group velocity

1.4.1 Local phase velocity

The medium velocity c per patch is required to calculate the model vector associated to the trial-source position (equation 1.4). In practice, the velocity is introduced in the MFP as an unknown parameter. This means that we can optimize the local phase velocity for each patch using the MFP output amplitude. To do so, we propose the following workflow:

1. Preprocessing of the data with spectral whitening in the chosen frequency band (here between 5 Hz and 7 Hz). As this analysis is based only on the phase of the signal, the amplitude spectrum of each sensor is normalized to 1.

2. Calculation of the full CSDM K using sub-segments of 30 s (15-min-averaging window). We use 30 s subsequent noise recordings to calculate the CSDM K. Each of the 30 s segments adds new and independent information to the CSDM, which is a square matrix with dimensions equal to the number of receivers within one patch (typically 48 in the present experimental configuration). When the number of sub-segments is not sufficient to ensure a full-rank and invertible CSDM K, we may add a diagonal matrix with constant amplitude ϵ to the CSDM, where ϵ is the norm of CSDM K divided by 100 $\epsilon = \frac{||K||}{100}$.

3. Definition of a vector of phase velocities c in the range of 400 m/s to 1200 m/s. For each local phase velocity c, we calculate the modeled Green's function.

4. Matching of the modeled Green's function with the CSDM K using the Bartlett processor. The maximum value of the Bartlett output gives the optimal phase alignment for all of the receivers within one patch at a given local phase velocity c. The maximum value of the Bartlett output can be used as a criterion for the selection of the correct local phase velocity (i.e., the higher the Bartlett value, the better the phase alignment).

When applied to each patch separately, this workflow provides information about the local phase velocity in a given averaging time window, from which a phase-velocity map can be drawn (Figure 1.6). The distribution of the local phase velocities for the monitored area shows a trend, with lower velocities in the North-West, and higher velocities in the South-East. The application of this method to the 5 days of recording allowed us to monitor changes in the distribution of the local phase velocity per patch. This showed that standard deviation of the local phase velocities do not exceed 10% during the recording interval (Figure 1.7).

When applied to different frequencies, this technique provides the local dispersion curves for Rayleigh waves. Dispersion of surface waves is mostly due to a vertically stratified medium. Different wavelengths sample different layers of the subsurface with different mechanical properties, which means that the shape of dispersion curves is related to geologic profiles (Pei (2007)).

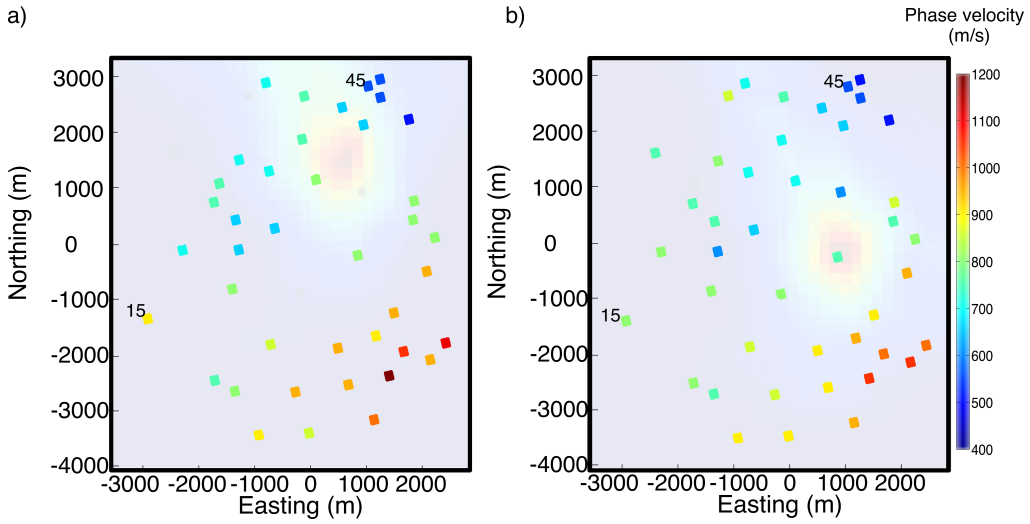

Figure 1.6: Local phase velocities for surface waves obtained for each patch from the MFP algorithm. The two maps were obtained using different 15-min periods of data in the frequency band of 5 Hz to 7 Hz with a single dominant noise source. These two sources correspond to those identified in Figure 1.5(a, b). In both maps, the trend toward larger phase velocities from North to South is clearly visible.

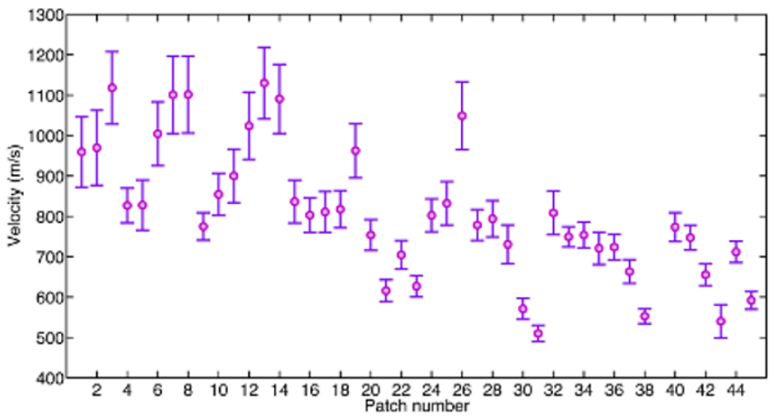

Figure 1.7: Local phase velocities per patch averaged over 5 days of data, together with standard deviations for the frequency band of 5 Hz to 7 Hz. Patches located in the south-eastern part of the medium showed higher velocities and stronger fluctuations over the 5 days of recording time. However, note that the local standard deviation is never higher than 10% of the average.

Two examples are shown in Figure 1.8 for two patches in the North and South-West of the network. As expected from the typical dimensions of the patch, the resolution of the dispersion curves is satisfactory from frequencies above 3 Hz. In the case of low frequencies, the resolution

is limited by the patch diagonal (i.e., the maximal distance between two receivers within one patch). The patch diagonal should be larger than half of the wavelength to provide a sufficient angular resolution of the MFP output. Note the presence of noise in the dispersion curves at higher frequencies (around 10 Hz), when the sensor distances within the patches reach the aliasing limit.

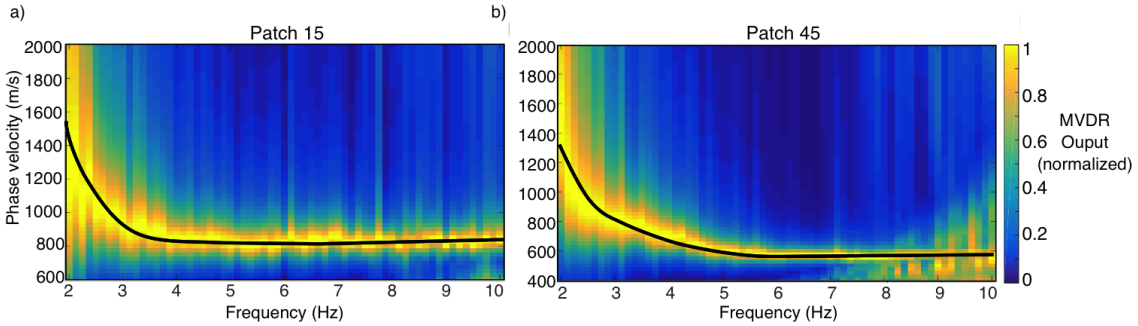

Figure 1.8: Dispersion curves for Rayleigh waves displayed as phase velocity versus frequency between 2 Hz and 10 Hz for patches 15 (a) and 45 (b) (see corresponding numbers in Figure 1.6). Each curve was obtained using the MVDR algorithm. The dispersion curves are normalized at each frequency.

1.4.2 Group velocity maps

The combination of all of the MVDR maps from different patches reveals the position of the dominant surface-noise source. When correctly identified and localized, this surface-noise source provides information about the group velocity between the different patches in the propagation medium. Indeed, Roux (2009) showed that directive ambient seismic noise can be used for passive seismic tomography. Note that local group velocities can also be obtained for each patch using the dispersion curves of the local phase velocities. As phase velocities do not vary with frequency in the band of 5 Hz to 7 Hz (Figure 1.8), the group velocities are equal to local phase velocities in this frequency band.

Here, we use the previously located noise sources on the surface for tomography inversion of the Rayleigh waves over the whole area of interest. We are still working with 15-min-averaging windows and 30-s subsegments. We use 10 localized sources to obtain the group velocity map, so in total, a window of 150 min is used to obtain the group velocity map presented in Figure 1.10. Here, the following workflow is proposed:

1. Preprocessing of the data with spectral whitening in the chosen frequency band, which is between 5 Hz and 7 Hz. This frequency equalization causes each receiver to have a similar amplitude noise spectrum, which reduces the bias in the extraction of the travel-time measurement from the noise-correlation function (Roux (2009)).

2. Next, cross-correlation of the data between pairs of patches, with the central receiver of one patch as the reference. We cross-correlated 30-s subsegments of the signal, and averaged these over 15 min, which is consistent with the previous steps.

3. Normalization of each component of the correlation function accordingto the energy of the preprocessed signals. In the case of directive seismic noise, the cross-correlation function shows only a single causal (or anticausal) coherent signal (Figure 1.9a). We verified that the time delays between the cross-correlation functions for each patch pair did not depend on the choice of the central receiver in one or the other patch.

4. Application of move-out to the cross-correlation functions, to realign the surface-wave arrivals for sensors in the same patch, using the local phase velocity, which is given by:

$$\Delta t_{pj} = \frac{x_{r_j S} - x_{r_0 S}}{c_p} \tag{1.7}$$

where c_p is the phase velocity for the considered patch, $x_{r_j S}$ is the distance between receiver r_j in one patch and the source position *S*, and $x_{r_0 S}$ is the distance between the central receiver r_0 in the patch and the source position *S*.

We take the maximum of the final ambiguity map as the optimal noise-source position S. However, in most cases, correction is made to the move-out to take into account the extended shape of the noise source. This correction consists of optimizing the source position separately for each pair of patches on a 1-km-squared grid projected around the maximum of the ambiguity map. Different move-outs (corresponding to each position on the 1-km-squared grid) are applied to the noise cross-correlation functions for each patch pair separately. The time-delayed correlation functions are stacked over each patch, to produce two wavelets. The optimal source position for a set of patches maximizes the amplitude of the envelopes of two wavelets (Figure 1.9b). The difference in travel times Δt_g the envelopes leads to the group velocity measurements, as explained below (Figure 1.9c).

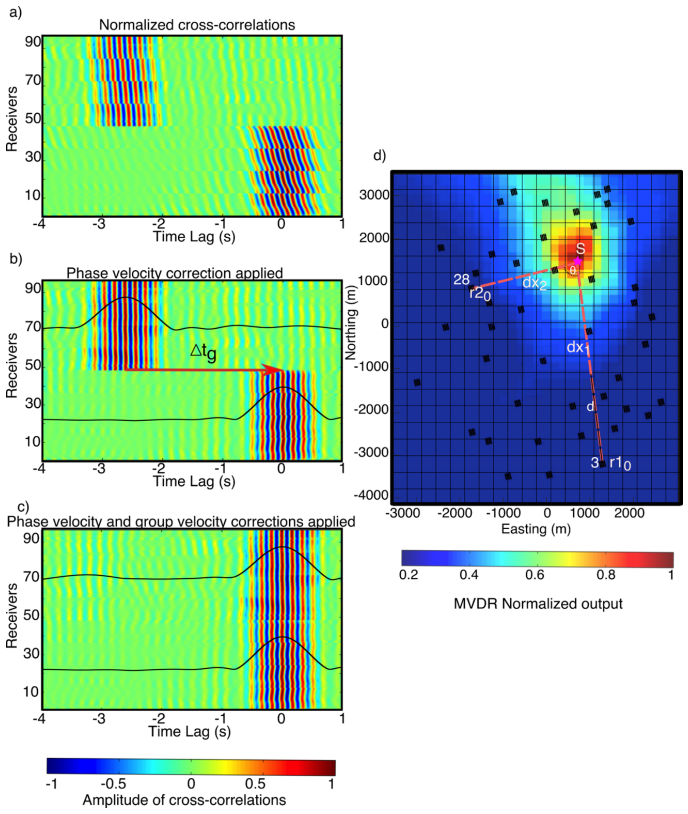

Figure 1.9: (a) Normalized noise cross-correlation functions between patches 3 and 28. (b) Re-aligned cross-correlations according to local phase velocity corrections per patch. The envelopes of the stacked cross-correlation functions are given in black. (c) The travel-time difference Δt_g between the two envelopes gives information about the group velocity difference between the two patches. (d) Spatial map with patches 28 and 3, and the dominant noise source. Two ray paths (in red) correspond to great-circle propagation between the source S and the center r_{1_0} and r_{2_0} of each patch. The travel time Δt_g in (b) corresponds to the travel-time difference between the two ray paths. The angle θ is the angle between the source and center of the two patches and d is a difference in ray-path distances.

For each pair of patches, the remaining time shift Δt_g between the two envelopes of the stacked correlation functions can be attributed to the travel-time difference between the wavelets when they propagate from the source S to the center of each patch. We can represent Δt_g as an integral of slowness along two different ray paths between source *S* and the center r_{1_0} and r_{2_0} of each patch:

$$t_g = \int_S^{r_{1_0}} \frac{1}{c_1} dx_1 - \int_S^{r_{2_0}} \frac{1}{c_2} dx_2 \tag{1.8}$$

5. Finally, surface-wave tomography inversion is performed from the collection of travel-time Δt_g and the set of ray paths obtained between each pair of patches for the different noise-

source locations that were isolated from the ambient-noise data. Each ray is projected on the 300 m x 386 m grid. It means that each ray between the source *S* and the center of each patch: r_{1_0} and r_{2_0} is represented as a discrete sum of local ray units dx_1, dx_2. Each ray unit dx_1, dx_2 crosses one cell of the 300 m x 368 m grid (Figure 1.9d).

For pairs of patches that are not aligned with the source position, some constraints are introduced before inversion, to ensure a reasonable a priori model: we exclude the cells in the vicinity of a source and we limit the pair of patches to angles $\theta < 150°$ between the source and the patches and to differences in ray-path distances $d > 10\%$ of the longer path (Figure 1.9d). Note that these criteria are data dependent and were chosen in an empirical way. These constraints reduce the total amount of input that can be used for inversion for a given source location. In practice, 10 different source locations were extracted in 150 min, for a total of 463 different travel-time Δt_g, and their corresponding paths (Figure 1.10a). Of course, the use of more trial sources would increase the spatial coverage for inversion.

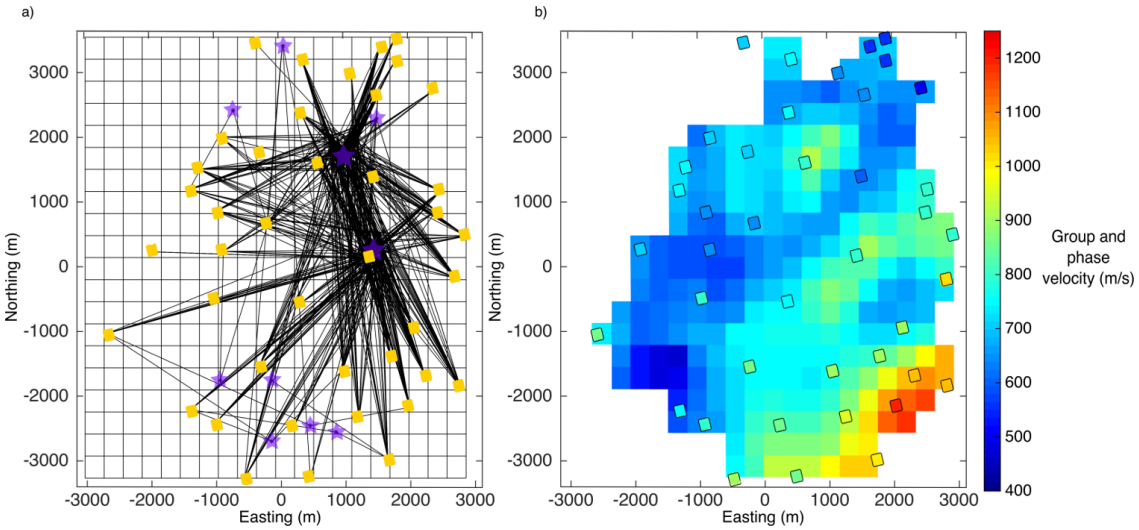

Figure 1.10: Travel-time tomography inversion from the patch-array distribution. (a) Map showing the patch-array network projected on a regular grid with the combination of distances between a source and a pair of patches (according to Figure 1.9d). A total of 10 different noise sources were used to perform the tomography inversion (source positions are marked as purple stars). (b) Tomography inversion for group velocities together with local phase velocities per patch obtained from the MFP in the 5 Hz to 7 Hz frequency range. The x-y coordinates are relative to the center of the grid.

The tomography inversion is performed using a Bayesian approach based on Tarantola (1987), with great-circle propagation approximation. Local slowness is linearly inverted on a spatial 300 m x 386 m grid from the travel-time data, with an a priori error covariance matrix that decreases

exponentially with distance over five cells for spatial regularization. Figure 1.10b shows a group-speed map obtained for Rayleigh waves in the 5 Hz to 7 Hz frequency band using a total of 150 min of ambient-noise recording. The group velocity map is in agreement with the local phase velocities measured at the same frequency. This map can then be obtained at different frequencies between 3 Hz and 10 Hz (although this is not included here), to build a subsurface structural model for shear-wave velocity.

1.5 Discussion

All of the ingredients of the methodological approach presented here were previously developed in recent studies, either in the context of ambient-noise seismology or passive geophysics exploration. Basically, the two main ingredients are: (1) the use of MFP to localize ambient-noise sources within the network (Corciulo et al. (2012); Vandemeulebrouck et al. (2013)); and (2) the use of directive ambient noise to achieve surface-wave tomography on a dense array of seismometers (Roux (2009)).

In general, the use of beamforming (or MFP) requires phase coherency among the different stations of the network. The average inter-station distance then drives the frequency band of interest, as spatial aliasing can become an issue. For example, around the San Andreas Fault, with 30 stations spread over a 40-km2 area, beamforming was limited to surface waves in the micro-seismic band (around 0.2 Hz: Roux et al. (2011)). On the other hand, with 400 stations in a 1-km2 zone, MFP was successfully used around 6 Hz for the detection and localization of weak incoherent signals buried in noise (Corciulo et al. (2012))

The group velocity map shows large variations over the area of interest. However, the assumption of great-circle propagation of surface waves gives satisfactory results. The mean variance of the reconstructed times was 5%, which means that the reconstructed group velocity model agrees with the travel-time data. We can consider this map as a first iteration in an iterative tomography procedure for off-great-circle path propagation (Woodhouse and Wong (1986)). Other methods can also be considered to correct the effect of straight ray propagation, such as the Eikonal tomography (Lin et al. (2009)) or frequency-dependent ray tracing and a wavelet-based sparsity-constrained tomographic inversion (Fang et al. (2015)).

Also, the tomography results can be improved with the use of more noise sources at the surface, with, in the ideal case, sources that do not overlap in time and are widely distributed in space. Of course, difficulties arise when several noise sources are in competition at the same time. This is probably the case when platforms, roads, and injection wells work together as incoherent seismic sources. Attenuation can then be helpful to separate the louder from the weaker noise sources locally. Dominant and stable surface sources originating from human activities may be less attenuated than micro-seismic sources at depth that are related to injection or extraction processes. Corciulo et al. (2012) explored this stronger-versus-weaker sources approach. If

multiple sources are present at the same time (with a nearly isotropic noise-source distribution), the cross-correlation between patches can directly provide the travel-time separation between the patch centers, as expected from the noise correlation theorem (Roux et al. (2005)). This can potentially further simplify the surface-wave tomography inversion.

The approach used in the present study allows the extraction of both local phase velocities and group velocities. These are retrieved in separate manners, but provide complementary information. The workflow for local phase velocity extraction is completely automatic, whereby no a priori information is needed. Working on a local scale within dense patches provides robust information on the phase velocity and surface-noise source localization up to at least 10 Hz. We chose to work in the frequency band between 5 Hz and 7 Hz where surface noise shows high spatial coherence. For most patch-arrays, there seems to be no velocity dispersion in this frequency band; the dispersion curves are reaching their plateau. This means that the subsurface is vertically homogenous on a certain depth interval that corresponds to the central wavelength around 6 Hz ($\sim$100 m). Note that our method has a limited depth resolution associated to this finite bandwidth. Extracting dispersion curves outside of this band (which depends on surface noise spatial coherence properties) can allow us to image the subsurface at shallower or greater depth.

Ambiguity maps for the source location and a local phase velocity per patch are extracted in a joint way. The combination of ambiguity maps reveals the position of the dominant noise source at the surface. This can be used to obtain group velocity information between patches. This workflow can be biased by several uncertainties associated with surface-source localization, ray-path propagation, and parameterization of the linear inversion. In practice, the source localization method is relatively robust due to the combination of several ambiguity surfaces for all, or at least part, of the patches. We verified that 100 random, independent perturbations of +/-10% from the optimal local phase velocity per patch results in a maximal total shift of +/-30 m longitudinally and +/-50 m laterally from the optimal source position. This confirms that the proposed method for surface-noise source localization is robust.

The local phase velocities can be obtained up to 10 Hz and can give detailed information about local subsurface properties, including shallow layers. The group velocities provide a general overview of the medium up to 7 Hz (deeper layers). Together, local phase velocities and group velocities add additional, strong constraints on the geological subsurface structure. They are measured in a separate manner, which means that error processes in the measurements are independent, so their simultaneous inversion is significantly better than the use of either alone.

1.6 Conclusions

The patch-array design at the surface gives a possibility to use different, alternative approaches by using ambient noise correlations. Localized, punctual noise sources provide significant physical importance and, what is more, they accelerate the convergence towards the noise-correlation

function. Contrary to low-frequency ambient-noise tomography that classically requires long averaging periods (i.e., several hours to days), a duration of 15-min was sufficient to produce the phase velocity maps and 150-min to produce the group velocity maps in this study. The use of directional sources seems to be more adapted in land exploration geophysics due to limited time of recording and the presence of strong human-related noise sources. The human-related sources such as pumps, wells and drilling platforms generate noise, which propagates as surface waves. These sources of opportunity are often situated within the network area. Thanks to the acquisition with patch arrays, ambient noise tomography is no longer limited to random noise sources outside of the monitoring area.

In practice, the patch-array distribution allows us to work efficiently at two different scales. Locally, phase velocities can be inverted in the frequency range of 3 to 10 Hz at least in order to obtain local static corrections correcting for near surface effects. However, group velocities add an important constraint to the inversion up to 7 Hz. This multi-scale approach paves the way to substantially more accurate inversion of surface waves and production of wide and accurate maps of static corrections due to strong constraints coming from both local phase velocities and group velocity maps. We are able to extract information about the subsurface using only the ambient noise recorded during acquisition and the present methodology; no extra costs are needed.

The spatial coherence associated with this local incoherent source will build rapidly over time, and can be used as a coherent source by the patch-array design. To multiply the number of "controlled" and localized sources, noise can for example be generated by a truck that continuously and locally circles in one position in the field for a few minutes. After a few minutes of continuous seismic ambient noise generated locally by the truck (i.e., typically 5 or 10 min), this one could then move to another position with the same strategy. The methodology we describe here opens the route to environmental monitoring of the subsurface from the repetitive inversion of phase and group velocity maps with ambient-noise surface sources.

Chapter 2

Matched Field Processing in microseismic monitoring.

In this chapter we present another application of Matched Field Processing in microseismic monitoring using patch array acquisition.

2.1 Hydraulic fracturing and microseismic monitoring

Hydraulic fracturing consists of injecting high-pressure fluid into porous reservoirs to increase their permeability. It is used to enhance the efficiency of geothermal systems (Enhanced Geothermal Systems: Deichmann and Giardini (2009) Dorbath et al. (2009)) or to stimulate hydrocarbon reservoirs.

In general, vertical wells are deviated and drilled almost horizontally to pass through the reservoir. Then the rock is perforated with explosives that are called perforation shots. Next, a propant is injected into the well to stimulate pre-existing fractures. Hydraulic fracturing stimulation of a horizontal well is usually done in multiple stages with known volume and fluid components (Davies et al. (2012)). Fluid injection and production change stress and modify pore pressure in the formation. This may induce microseismic activity in the proximity of the reservoir. Historically, downhole geophone tools have been used to monitor microseismic activity during the stimulation programs (Rutledge and Phillips (2003)). Monitoring with downhole arrays needs close observation wells. Signal-to-noise ratio is high, only if the well is not located within the focal plane (Figure 2.1). In the past 10 years, we have seen the advent of dense surface networks to record hydraulic fracture growth. Surface microseismic monitoring requires increased array apertures and source coverage. Within this constraint, it gives comparable results to downhole techniques in terms of detection sensitivity and resolution (Lakings et al. (2006); Eisner et al. (2010)).

The physics of induced microseismic events is the same as of the earthquakes, only in a micro scale. Microseisms are defined by their origin times and hypocenters. Microseismicity induced by

hydraulic fracturing is usually observed at (1000-3000) m depth (the depth of stimulation wells). In most cases, their magnitude is lower than -2. Signal to noise ratio depends on the level of the ambient noise, distance and radiation pattern of the event – Figure 2.1. Due to cost considerations, in surface microseismic monitoring only vertical sensors are generally deployed. This leads to the use of only P-waves for surface microseismic monitoring. Using P-waves and advanced location algorithms allows locating accurately microseismicity, although this location is achieved with a false time of origin and with a significant vertical uncertainty.

One of the biggest challenges in microseismic monitoring from the surface is the presence of strong seismic noise. The origin of this surface noise might be: instrumental, natural (e.g., wind, rain) and anthropogenic (e.g., pumps, infrastructure, traffic). These are named noise, as they do not provide any subsurface information (Scales and Snieder (1998)). Usually the noise above 1 Hz is caused by local atmospheric conditions and human activity. Also, it has been shown that seismic noise can go up to (60-70) Hz (e.g., wind noise: Young et al. (1996)).

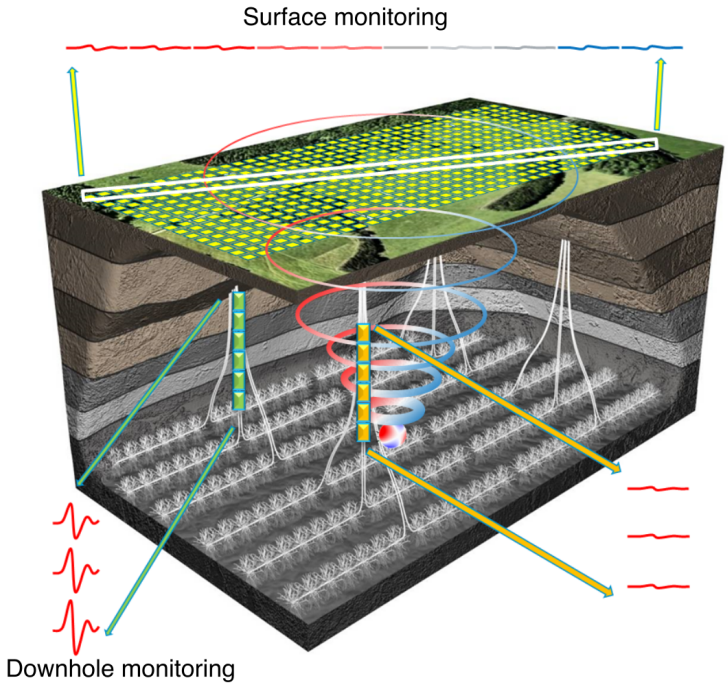

Figure 2.1: Microseismic monitoring of hydraulic fracturing. Monitoring with downhole arrays needs close observation wells. Surface array are easy to deploy and provide high coverage (image: courtesy: Statoil).

2.1.1 Current processing: relative joint detection and location of microseismic events

Traditional location methods based on the first arrivals cannot be applied in microseismic monitoring due to low signal to noise ratios. However, there are many different approaches for detecting and locating microseismic events recorded on the Earth's surface.

The detections and localization of microseismic method give more possibilities if data are acquired with multi-component sensors (P- and S- waves available). It easies the optimization of the velocity model and reduces the uncertainty of the localizations. Multi-component recording enables the use of direction or polarization analysis method. However, microseismic surveys are usually 1C (Duncan (2005), Lakings et al. (2006)). It implies the use of inversion or migration based methods. Duncan (2005) implemented a travel-time migration based method, which is based on a stack of waveform. Chambers et al. (2010) proposed a migration approach: ray-based diffraction stack method with surface arrays to locate microseismic events in Valhall Field. Zhebel and Eisner (2014) took into account a source mechanism correction including moment tensor inversion. Corciulo et al. (2012) proposed another method with Matched Field Processing to locate microseismic sources at the exploration scale using the ambient-noise data.

The absolute location methods generally need an accurate velocity model to provide a correct position and time of origins of microseismic events. However, introducing a relative location might ease some issues. Master event approach was developped by Evernden (Evernden (1969a), Evernden (1969b)). In 1994, Got et al. proposed a relative location method of microseismic events under a Kilauea volcano. This relative approach is successfully applied also in microseismic monitoring (e.g. Grechka et al. (2015)).

In this chapter, we work with two datasets that were acquired with the 1C patch acquisitions. The data were previously processed using a relative method of joint detection and localization (Roux et al. (2014)). This relative migration-based approach involves three steps: beamforming, joint detection and joint location (Figure 2.2). First, an event is correlated with a template. This template acts as an empirical Green's function; it can be a picked perforation shot, whose position is known. Events situated in the proximity of the template share almost identical move-outs. The correlation of the data with the template applied a first moveout to align the events (Figure 2.2a). All locations are relative to the template's hypocenter. The origin time and hypocentral coordinates of the events are found with a grid search in a volume surrounding the template: each perturbation on the template's coordinate is translated as a move-out applied to the correlation functions. A polarity correction is applied to the traces to ensure a constructive stacking. The most precise sign corrections consist in finding the focal mechanism. Other less precise corrections are: the square of amplitudes or an envelope of a microseismic trace. The stack of the corrected traces is a time and space dependent curve, whose 4D maximum provides hypocentral coordinates and origin time.

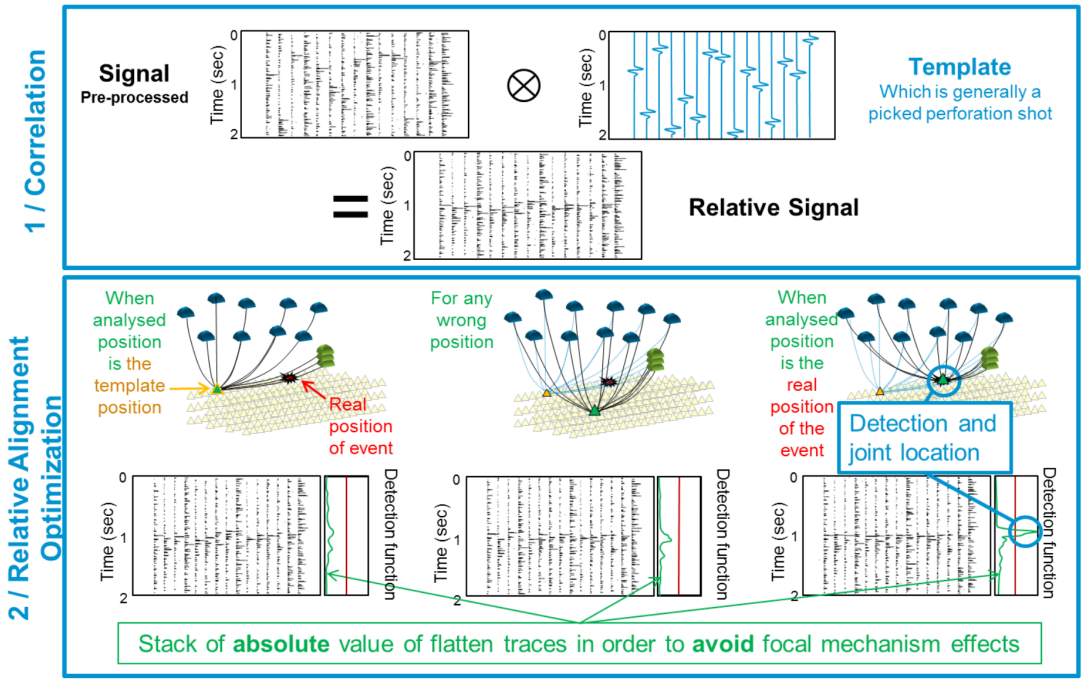

Figure 2.2: Relative detection and location of microseismic events: to detect and locate microseismic events a relative migration-based approach is used that involves three steps: a) beamforming, b) joint detection and c) joint location.

Obviously, relative location simplifies many issues. Effectiveness of this method depends less on a velocity model or statics. It means that we might successfully use a homogenous velocity model with the relative method. However, this method requires a manual screening of detections in order to check their reliability and remove false detections.

We also observe a raise of location methods that impose on coherency of waveform stacking (e.g., The Source Scanning Algortihm (SSA) Kao and Shan (2004)) or spatial phase coherency (e.g., Matched Field Processing (MFP) Jensen et al. (2011)).

In this chapter, we present applications of Matched Field Processing (MFP) in microseismic monitoring. It is a coherence based method.

The spatially coherent part of the microseismic noise can be appropriately summed to detect and localize the areas of downhole noise. This approach was explored before by Corciulo et al. (2012) to find weak sources at depth that were related to the extraction process. However, we explore other possibilities of MFP in surface microseismic monitoring. First, we use the Multirate Adaptive Beamforming (MRABF) in an automatic way to suppress surface waves. This allows reducing the number of false events and finding new events. We also propose a purely automatic approach to detect and locate microseismic activity with MFP. The previously described relative

location and detection method is used to verify our results. It helps to assess the reliability of the introduced techniques.

2.2 Attenuation of seismic noise in microseismic monitoring from surface acquisition

In this section, we demonstrate an efficient and automatic way to attenuate seismic noise in microseismic monitoring Chmiel et al. (2015). To attenuate the undesired recorded noise we develop a solution that combines acquisition and processing. On the acquisition side we make use of distributed patch arrays for signal redundancy purposes as well as having the means for spectral signal, noise discrimination and separation. In this section, we use data from the same acquisition, as presented in Chapter 1 (44 patches were sparsely distributed on a 41 km2 area during five days).

The processing strategy consists in a high resolution, data driven, spectral characterization of the noise in the frequency - spatial domain followed by a surgical, narrow band, signal preserving noise suppression. This method is based on Multirate Adaptive Beamforming (MRABF) approach developed first by Cox (2000). This method can be used to increase the signal to noise ratio, to detect low frequency microseismic events or small amplitude high frequency microseismic events. To apply this method, we do not need any a priori information. The only assumption made is that there are some coherent/incoherent noise sources at the surface. This assumption is typically the case when looking at real data.

2.2.1 MRABF - Theoretical description

In the previous chapter, we used Matched Field Processing algorithms: Bartlett and MVDR to locate noise sources on the surface. In this section, we present another algorithm: Multirate Adaptive Beamforming (MRABF) to separate noise sources. Clearly, the noise field is complex. We may observe noise sources overlapping in time and in space. Still, it is possible to separate different noise sources using their spatial coherence. The MRABF technique allows distinguishing and localizing different noise sources through the use of a projection algorithm that is performed using the eigenvector decomposition of the CSDM. Let's remind that the final CSDM $\bar{K}$ is the arithmetic mean for all the snapshots:

$$\bar{K} = \frac{1}{M} \sum_{i=1}^{M} K_i \tag{2.1}$$

where M – is the number of the snapshots.

The rank of CSDM usually equals the number of noise segments (snapshots) that were used. In order to separate one or more sources in the seismic data, the rank of the matrix $\bar{K}$ should be

no less than the number of noise sources to be separated. If we want to separate different sources one can decompose the matrix $\bar{K}$ according to:

$$\bar{K} = U\Lambda V^H = \sum_{m=1}^{M} U_m \Lambda_m V_m^H \tag{2.2}$$

where U and V are the orthonormal, (N,N), eigenvector matrices and Λ the diagonal, (N,N), eigenvalue matrice. The Hermitian properties of the $\bar{K}$ matrix ($\bar{K} = \bar{K}^H$) implies $U = V$.

We can use the individual eigencomponents in MFP in order to reveal the secondary noise sources. For example, if we want to use the i-th eigenvalue, we create a new CSDM using only this value, which reads:

$$K_{new} = U_i \Lambda_i V_i^H \tag{2.3}$$

And then the Bartlett algorithm is calculated using matrix $\bar{K}_{new}$.

Figure 2.3 shows a distribution of the eigenvalues for CSDM calculated with 15 minutes of data. The CSDM was averaged over 30 snapshots in the frequency band: (5-7) Hz and the eigenvalues are averaged over all the patches. One can see that the first eigenvalue is strongly separated from the others-it corresponds to the principal noise source on the surface. The distribution of the eigenvalues clearly shows the rank of the CSDM (rank = 30). The eigenvalues higher than the rank of the CSDM constitute a plateau of the distribution.

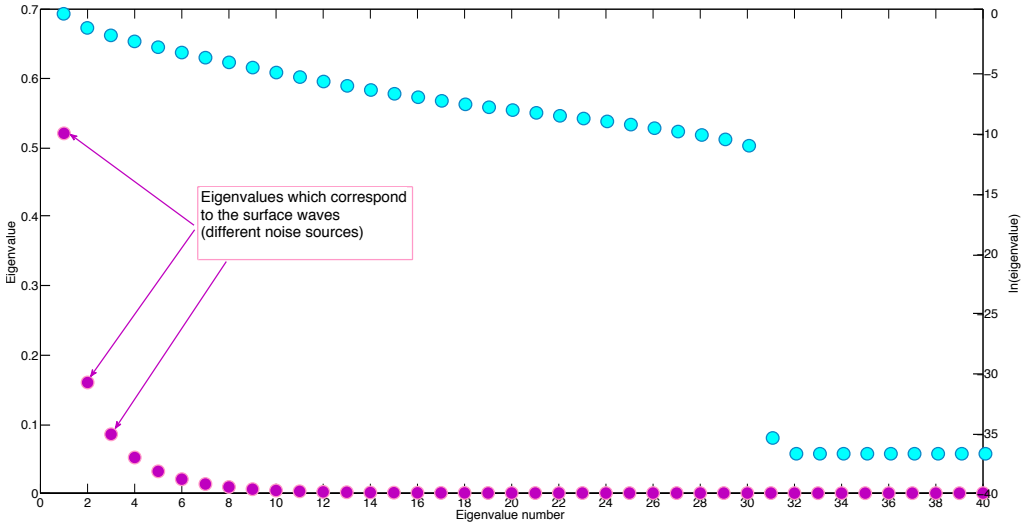

Figure 2.3: Eigenvalues calculated for the frequency band (5-7) Hz averaged over all the patches. This distribution allows distinguishing between different noise sources. The representation of the natural logarithm of eigenvalues (in blue) shows the rank of the CSDM, which is 30. The eigenvalues higher than the rank of the CSDM constitute a plateau of the distribution.

We now use the 1st, the 2nd and the 3rd eigencomponent to separate noise sources on the surface (Figure 2.4). Each ambiguity map is normalized by its maximum. The use of the first

eigencomponent improves the resolution of the main focal spot (Figure 2.4b). The secondary noise sources are revealed with the higher eigenvectors, using a selection of patches that point out the same source direction (Figure 2.4c, d). Of course, it might happen that the singular value decomposition is not perfect. Two eigenvalues might correspond to the same source or one eigenvalue might point to two sources. Also, the distribution of eigenvalues might differ from patch to patch.

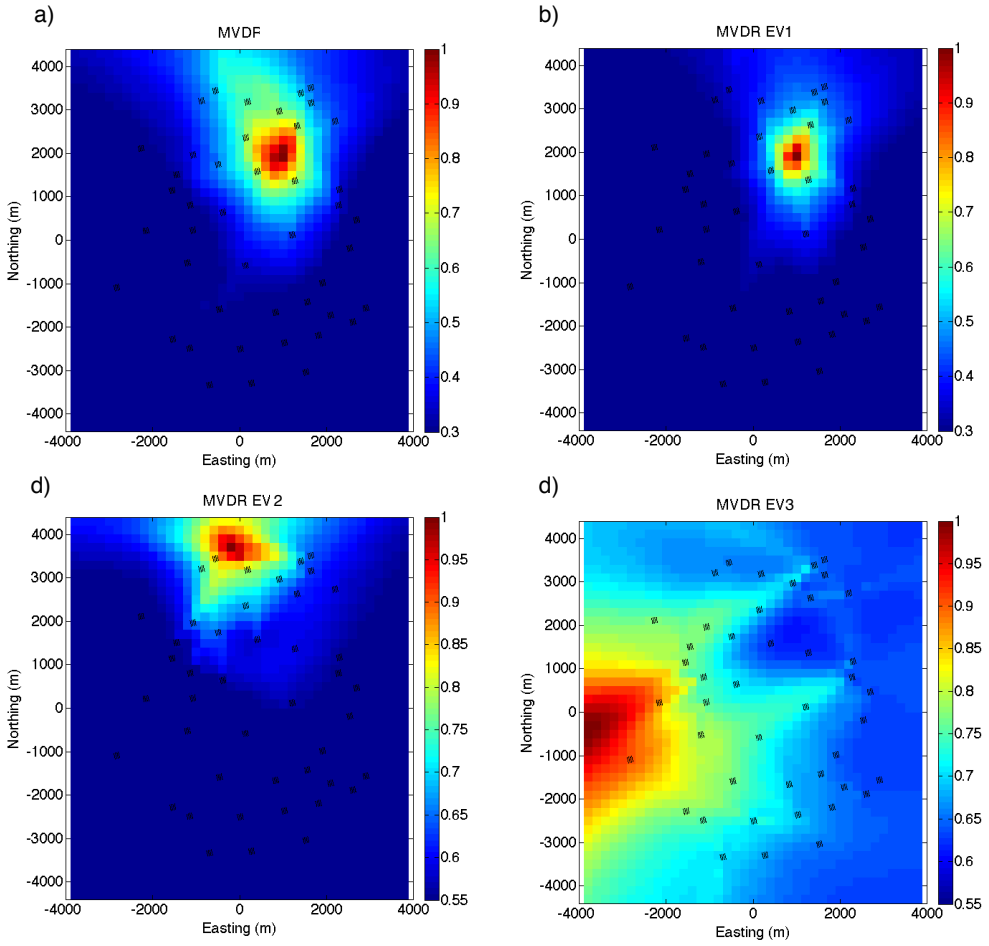

Figure 2.4: a) This ambiguity map was obtained using multiplication of all the maps per patch calculated with MVDR for 15 minutes of data. Amplitudes were normalized by the maximum of an output. The final ambiguity maps reveals a position of the primary noise source on the surface. b) Using the first eigenvectors allows improving the resolution of the MVDR output. The use of higher eigenvectors: b) the 2nd and c) the 3rd reveals the position of the secondary noise sources on the surface.

2.2.2 Algorithm to attenuate seismic noise in Microseismic monitoring

We now present an algorithm to attenuate seismic noise. The method is a fast and automatic means to attenuate coherent seismic noise whose source is located at the Earth's surface. The work-flow steps are: (1) calculate Fourier transform for a given time window, (2) determine the Cross-Spectral Density (CSDM) for each frequency and each array, (3) perform Singular Value Decomposition on the CSDM, (4) remove the eigenvalues that correspond to the most energetic noise sources at the surface: create a projected signal, (5) recreate signal in the time domain from the projector.

We discussed the fist two points in the previous sections. We now go back to the Singular Value Decomposition (equation 2.2) and discuss it in more details. We focus on the removal of the eigencomponents corresponding to the most energetic sources.

We can decompose the CSDM according to:

$$\bar{K}_{new} = K_{nn} + K_{ns} + K_{ss} = \vec{n} \cdot \vec{n^H} + (\vec{n} \cdot \vec{s^H} + \vec{s} \cdot \vec{n^H}) + \vec{s} \cdot \vec{s^H} \tag{2.4}$$

where $\vec{s}$ is the signal component and $\vec{n}$ is the noise component of the data vector $\vec{d} = \vec{s} + \vec{n}$.

To discriminate between noise and signal we make the following assumptions:

1. The noise is statistically invariant over consecutive time windows, so that the average of the K_{nn} is invariant over time.

2. The signal occurrence is sparse in time, so that the average of the K_{nn} decreases with the number of time windows involved.

3. The noise to suppress is often more energetic than the signal ($K_{ss} < K_{nn}$)) to the point it often hides the microseismic events.

4. The signal and noise do not statistically correlate, so that the average K_{ns} is close to zero.

Under the assumptions, 1, 2, 3, 4) listed above, the noise removal procedure we have implemented assumes that the noise CSDM K_{nn} corresponds to the Low Rank approximation of the average data CSDM $\bar{K}$: $K_{nn} = K_{LR}$.

The Low Rank approximation of the CSDM is obtain from its Singular Value Decomposition:

$$\bar{K} = U\Lambda V^H = U_p \Lambda_p V_p^H + U_{N-p}\Lambda_{N-p}V_{N-p}^H = \vec{n} \cdot \vec{n^H} + (\vec{n} \cdot \vec{s^H} + \vec{s} \cdot \vec{n^H}) + \vec{s} \cdot \vec{s^H} \tag{2.5}$$

One can decompose Λ as the sum of two diagonal matrices $\Lambda = \Lambda_p + \Lambda_{N-p}$. With Λ_p made of the *p* most significant eigenvalues and Λ_{N-p} made of the *N-p* remaining one's. The p^{th} Low rank approximation $\bar{K}_{LR}$ of $\bar{K}$ reads then: $\bar{K}_{LR} = U_p \Lambda_p V_p^H$.

To remove the dominant sources, we create a new signal projecting the largest eigenvectors out of the vector $\vec{d}$. We apply the projector $I - U_p V_p^H$ to the data $\vec{d}$ to construct the projected signal $\vec{z}$ as defined in Cox (2000):

$$\vec{z} = [I - U_p V_p^H]\vec{d} \tag{2.6}$$

where I is the identity matrix.

The last step of the algorithm is to recreate the projected (denoised) signal in the time domain, while performing the Inverse Fourier Transform.

2.2.3 Case study 1: A perforation shot

We now present an application of the denoising algorithm with microseismic data. To test this method, we follow a routine:

1. Choose a strong microseismic event.
2. Choose the length of the time window to be denoised and divide 30 s of data into corresponding number of segments (number of segments = 30/lenght of the time window).
3. Whiten and filter each segment in a frequency band: (2-80) Hz.
4. Denoise each segment per patch in a frequency band: (2-20) Hz.
5. Stack the data after applying a linear moveout.
6. Calculate the SNR of the stack before and after denoising.

To calculate the SNR we take the ratio of root mean square amplitude of the signal (one period around the maximum of the stack) to the rest of the signal (noise). This denoising method does not require any a priori information. However, there are certain parameters that need to be specified, such as: (1) the length of a denoised time window, (2) the number of eigenvalues to be removed. There is a trade-off between the lenght of the time window, period of surface waves and array aperture, that needs to be taken into account. Table 2.1 presents the change of the SNR as a function of the length of denoised time window. In the presented example, the optimal length of the time window is 3 s (Table 2.1, Figure 2.5) and application of this algorithm increases the SNR up to 140%. Also, we compare results of the denoising as a function of the eigenvalues to be removed (Table 2.1). We observe that removing only the first eigenvalue is notably sufficient to increase the SNR, although we can improve results by removing the second eigenvalue.

Table 2.1: Attenuation of surface waves. Noise reduction as a function of parameters: length of the time window and number of eigencomponents to be removed.

Length of the time window (s)	SNR original signal	SNR denoised signal (1 EV)	Noise reduction (1 EV)	SNR denoised signal (2 EV)	Noise reduction (2 EV)
1	10.0	14.9	1.5	10.9	1.1
2	10.2	16.4	1.6	16.5	1.6
3	10.0	21.7	2.2	24.0	2.4
5	15.7	23.4	1.5	27.3	1.7
6	14.6	29.5	2.0	27.8	1.9
10	14.8	27.5	1.9	29.7	2.0
15	18.0	27.8	1.5	24	1.3

The presented method allows attenuation of coherent and incoherent noise in an automatic and efficient way. We need no a priori information to use this technique and only two parameters need to be specified. Our results prove that this algorithm increases signal to noise ratio up to 140%. In addition, it allows broadening the frequency band of processing, i.e. to include lower frequencies. Therefore, in the case of microseismic monitoring it gives a possibility to detect more low frequency events. Also, it will reduce the impact of noise, so it will lower the number of false detections.

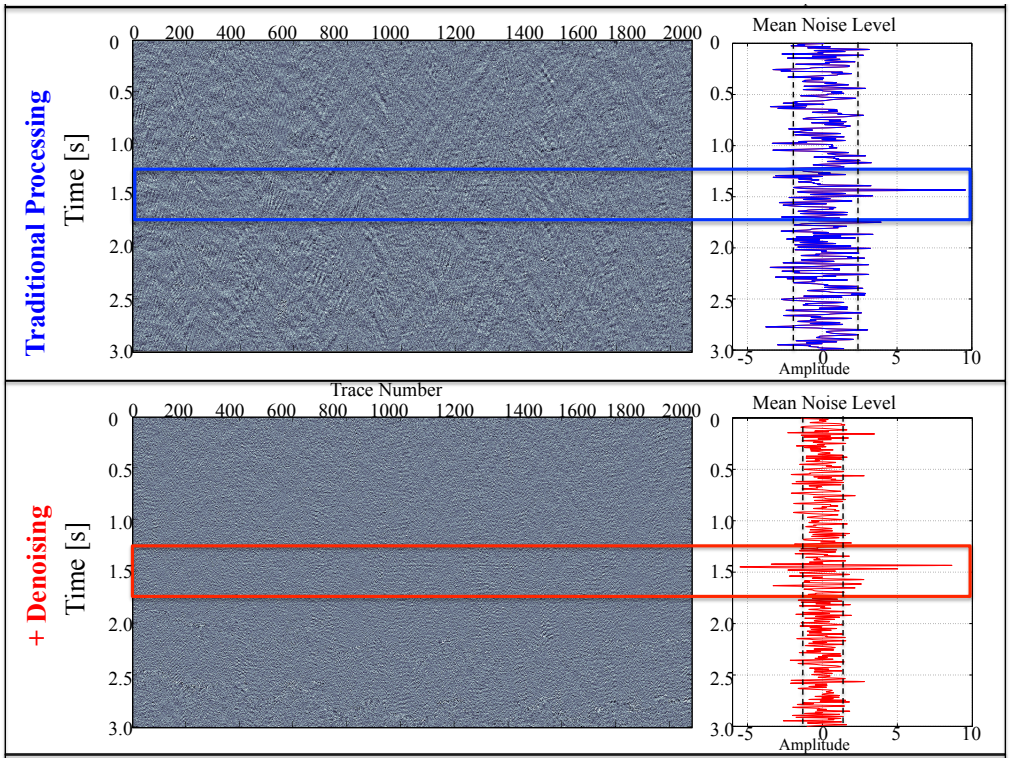

Figure 2.5: Attenuation of surface waves. The efficiency of the algorithm depends on the choice of parameters. In this example: short time window = 3 s; long time window = 30 s ; number of eigencomponents to be removed = 2. Surface waves suppression was performed in the frequency band of (2-20) Hz. In both cases data was whiten and filtered in the frequency band: (2-80) Hz.

This method allows real time processing and can be easily applied to any data set. The application can be generalized to active seismic data and other acquisition methods.

2.2.4 Case study 2: New detections.

In this example we focus on the detection of weak microseismic events. Low-magnitude microseismic events are estimated in higher frequencies (Maxwell (2014)). In order to find new, low magnitude microseismic events, we decided to work in the frequency band (50-70) Hz with 30 min of data corresponding to one of the fracturation stages. To test this method, we follow a routine:

1. We calculate CSDM matrix per patch in the given frequency band using sixty snapshots of 15 s (15 min).

2. We create a new signal by projecting out the first eigenvalue of the CSDM matrix.

3. We recreate the signal in the time windows of 15 s.

The distribution of the eigenvalues averaged over all the patches for the two CSDMs is presented on Figure 2.6. The first eigenvalue for both CSDMs are of a similar value and they are separated from the rest of the distribution. We make an assumption that this eigenvalue is connected with noise.

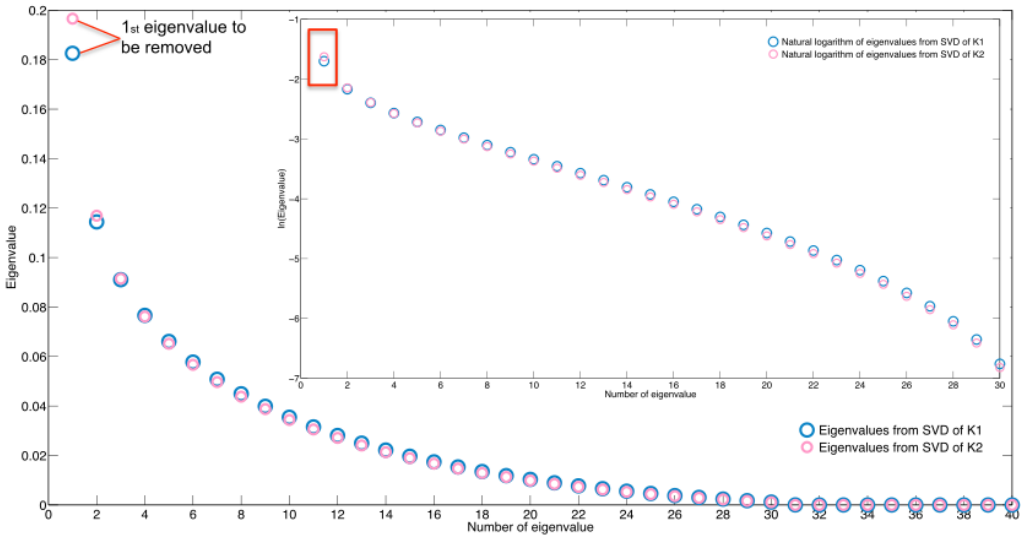

Figure 2.6: Distribution of eigenvalues for the frequency band of (50-70) Hz averaged over all the patches. Two CSDM matrixes were calculating using 15 minutes of data each and two projectors were created with a removal of the first eigenvalue to denoised the data

Next, we use the relative detection and location methods (describe in 2.1.1). We perform two tests: using the original and the denoised data. Before the noise suppression we find a swarm of 17 microseismic events within the processed stage (Figure 2.7). Two additional weak amplitude microseismic events are detected after the removal of the first eigencomponent and these are located within the swarm of the events.

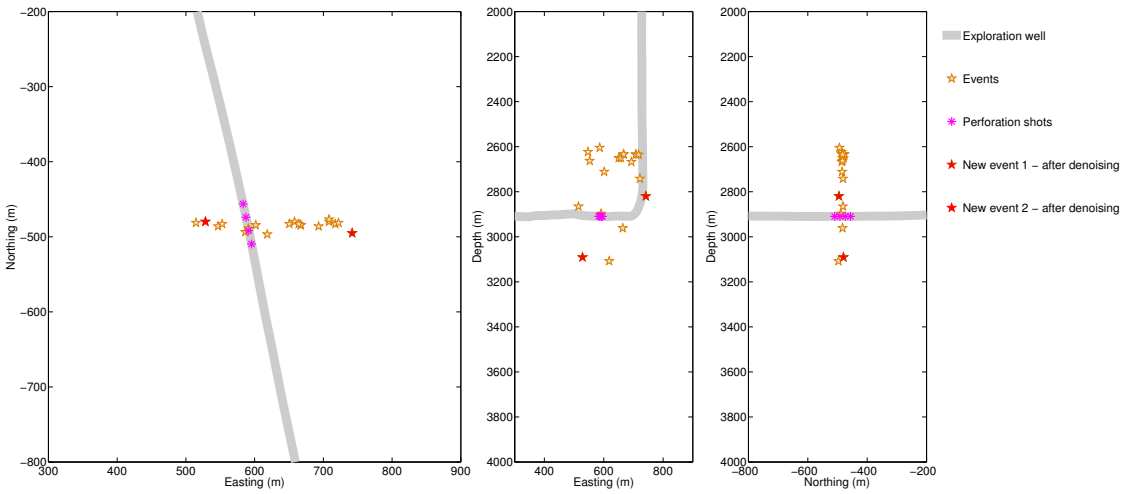

Figure 2.7: Results obtained using relative method of joint detection and location of microseismic events. A swarm of 17 microseismic events was found (in yellow) within the processed stage. After the removal of the first eigenvalue two additional weak microseismic events were found (in red).

To confirm the reliability of the detection, we use the Bartlett algorithm with the projected CSDM to detect the events and a homogenous velocity model vp = 4610 m/s. The MFP algorithms are applied on a time window of 3 s. The time window is centered at the time of the origin of the two new events. We construct a projected signal $\vec{z}$ by projecting the 1^{st} eigenvector out of the vector data $\vec{d}$ (equation 2.6). Then, we create a new CSDM using the projected signal:

$$K_{projection} = \vec{z}\vec{z}^{H} \tag{2.7}$$

Now, we can use the projected CSDM with the Bartlett processor to localize new events. We calculate the Bartlett value for each position in 3D regular grid.

$$B_{Bartlett}(\omega, a) = \sum_{\omega} |\vec{d}^{H}(\omega, a) K_{projection}(\omega) \vec{d}(\omega, a)| \tag{2.8}$$

where $\vec{d}(\omega, a)$ is a modeled Green's function between receivers in patches and a position in space calculated with homogenous velocity model. For the sake of simplicity we do not use the full elastic Green's function, we replace it with an appropriate 3D acoustic approximation. The modeled Green's function contains only P-wave phase term (the data were acquired using only vertical geophones) and it reads:

$$\vec{d}^{H}(\omega, a) = exp(i\omega \frac{x_{ja}}{c}) \tag{2.9}$$

where c is the medium velocity, and x_{ja} is the distance between each receiver position and the trial-point source position a. In the following sections we use the same approximation of the Green's function in MFP using the P-waves.

The Bartlett processor is calculated per patch. It means that we obtain a 3D ambiguity map per patch (similarly to Chapter 1). Obviously, not all the patches focalize on the depth. In order to obtain a final ambiguity map, we sum the Bartlett's output for selected patches. The position of the first microseismic event (Figure 2.8a) is obtained with 26 patches, while the second microseismic event (Figure 2.8b) with 38 patches. Each ambiguity map is normalized by its maximum. Figure 2.8 shows the cross-sections of the ambiguity maps taken at the maximum's position.

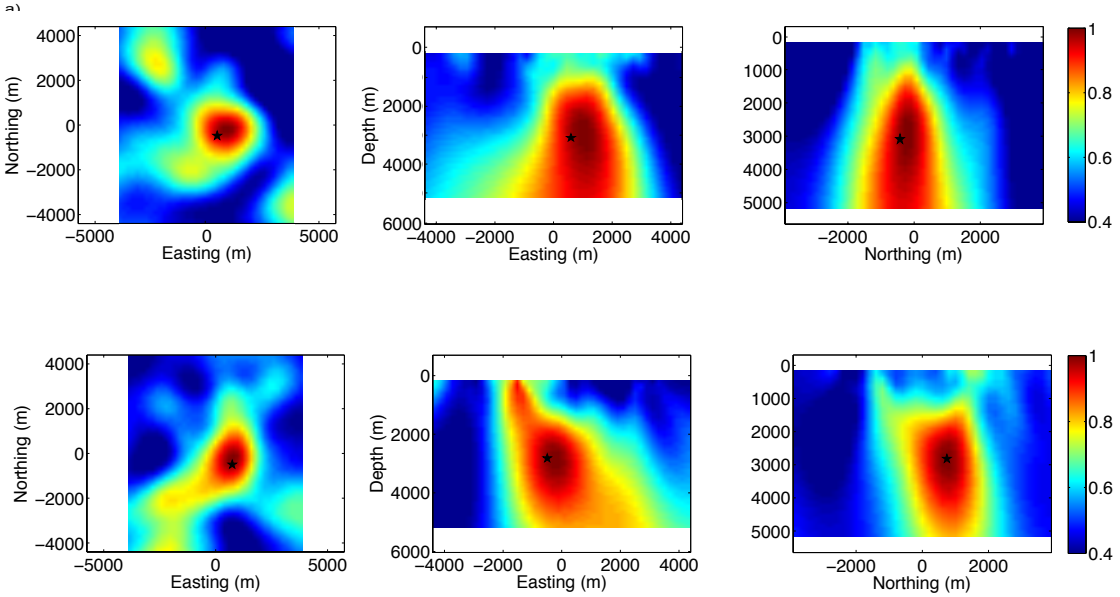

Figure 2.8: Cross-sections of the ambiguity maps calculated with Bartlett algorithm taken at the maximum's position (frequency band of (50-70) Hz). Using a projecting signal and combining together a selection of patches - 26 in a) and 38 in b) – we obtain a position of the secondary source at the depth. The difference between positions found with the relative method (black stars) and MRABF technique might be due to a velocity model. The presented coordinates are relative to the center of the acquisition

The results of locations using two methods (the relative and MRABF with Bartlett algorithm) are quite coherent. The maximum of the focal spot corresponds to the position obtained with the relative method. The difference between positions might be caused by the use of a homogenous velocity model and the absence of static corrections in absolute location.

2.2.5 Another acquisition with patches: Continuous detection after denoising

Now, we continue the analysis of the application of MFP methods in microseismic monitoring. However, we use another dataset. In this configuration a set of 35 patches was used for microseismic monitoring over a 54-km2 area in Oklahoma, USA (Figure 2.9a). The horizontal

position of the wells is presented in brown. The average distance between neighboring patches was 1 km. The distance between receivers was 37 m in the x direction and 12 m in the y direction for a total of 48 receivers on 4 lines of 12 receivers each (Figure 2.9b). Each receiver is, in fact, a sum of 12 tightly clustered vertical geophones. The x-y coordinates are relative to the center of a perforation stage. As a center of the stage we consider an averaged position of the perforation shots within the stage. On Figure 2.9c we see a time recording of 30 seconds of ambient seismic noise recorded at the patch 17 (47 receivers, signal recorded with the frequency sampling of 500 Hz).

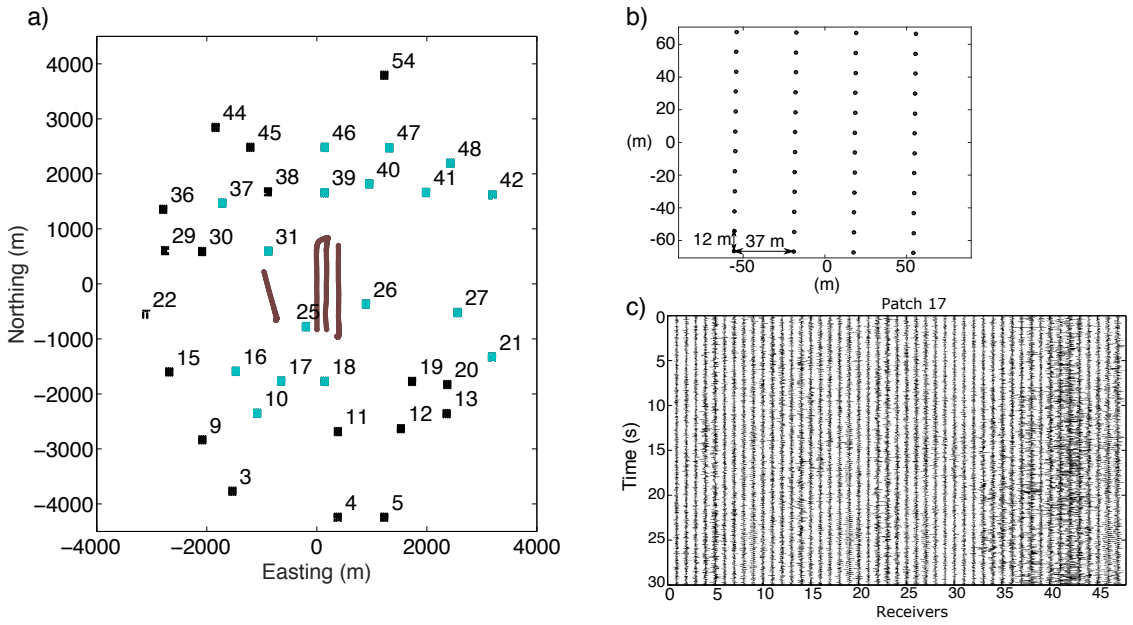

Figure 2.9: a) Experimental configuration with a set of 35 patches designed for microseismic monitoring over a 54-km2 area in Oklahoma, USA. The average distance between neighboring patches was 1 km. The x-y coordinates are relative to the center of the stage. b) Patch 11: The distance between receivers was 37 m in the x direction and 12 m in the y direction for a total of 48 receivers on 4 lines of 12 receivers each. Each receiver is, in fact, a sum of 12 tightly clustered vertical geophones. The x-y coordinates are relative to the center of the patch. c) Time recording (30 seconds) of ambient seismic noise recorded at the patch 17 (47 receivers, signal recorded with the frequency sampling of 500 Hz).

The data that we use correspond to one stage (213 min of data) of the hydraulic fracturing operations. There are four perforations shots within the stage. Figure 2.10 presents a spectrogram of the data averaged over all of the patches. The spectrum shows more energy in lower frequencies ($\sim$5-20 Hz). Note a strong, wide bandwidth energy peak between 120-140 min.

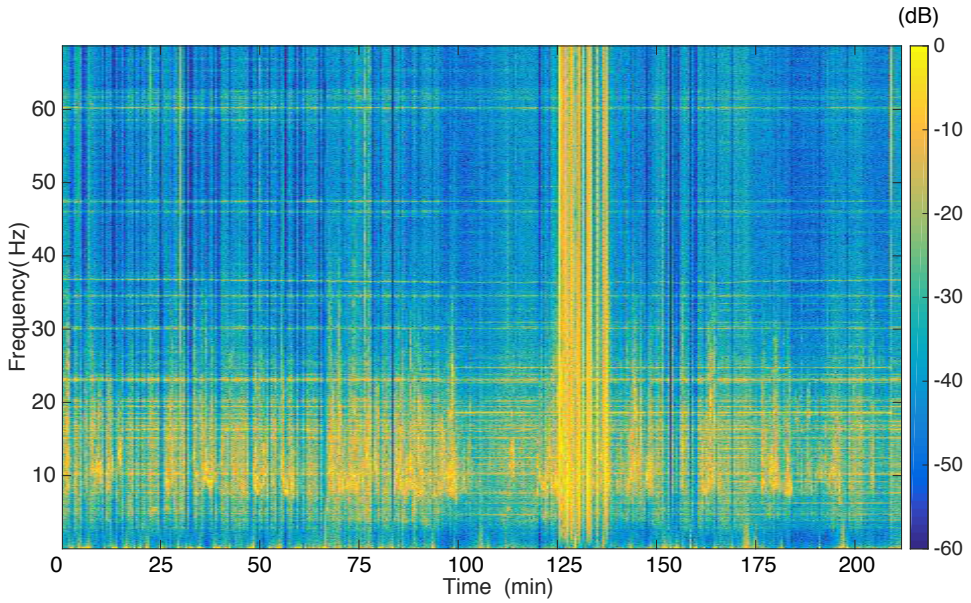

Figure 2.10: Spectrogram of 213 minutes of the data (stage 7) spatially averaged over all of the patches. Color scale represents normalized spectral amplitude, in dB

We now present some statistical information in order to quantify the role of the denoising in the continuous relative detection. We apply the denoising method on the 50 min of data:

1. We divide the signal into 12.5 min time windows. We calculate the CSDM per patch for each 12.5 min in the given frequency band. To calculate one CSDM we use 50 snapshots of 15 seconds.

2. We create a new signal by projecting out the first eigenvalue of the CSDM matrix.

3. The signal is recreated in the time windows of 15 seconds.

Signal is processed within a frequency band (2-70) Hz and the surface waves suppression is performed in a frequency band (2-20) Hz. Then, we apply a relative algorithm of joint detection and location to the continuous data with a homogenous velocity model vp = 4467 m/s. We compare the results of detections before and after the application of denoising algorithm (Figure 2.11).

The use of the denoising algorithm reduces the number of false detections by 18%. It means that the screening of events could be faster and less ambiguous. Moreover, the number of microseismic events is increased by 12% (Figure 2.11a). However, this method does not completely preserve the amplitude. We observe an average 15% increase of the amplitude of the stack, together with an average 7% loss (Figure 2.11b). Possible improvements should consist in adding a criterion to distinguish before surface waves and body waves (e.g., a focalisation of the 3D

beamformer in the depth). Of course, the number of eigenvalues to be removed depends on the frequency band: in lower frequencies where most of the energy comes from the surface waves we need to remove more eigenvalues in order to focalise on the depth. In higher frequencies removing only the first eigenvalue (or none) might be sufficient to detect low-magnitude microseismic events.

To sum up, the presented method of denoising can improve the results of microseismic detection. Thanks to the removal of surface noise sources, we can broaden the frequency range of processing. This method turned to be useful in finding new microseismic events and in reducing a number of false detections. It does not need any a priori information and it is easy to implement. The future works should consist in finding an amplitude preserve criterion.

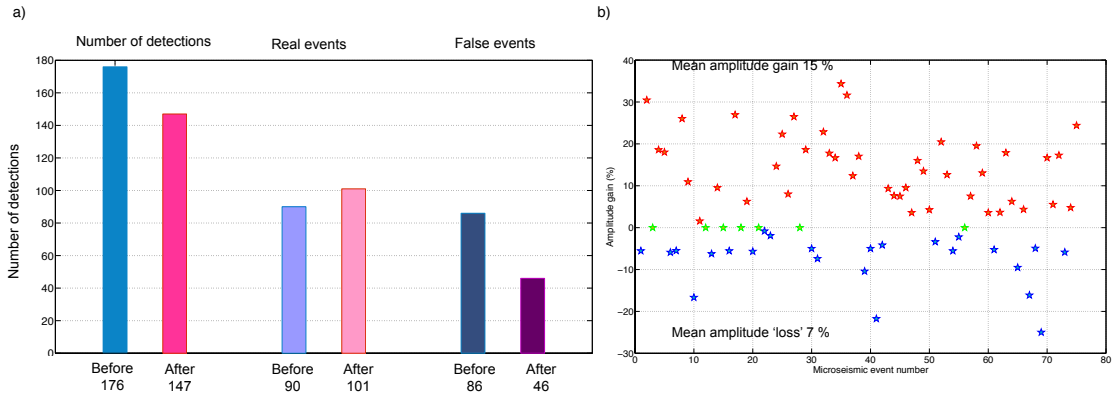

Figure 2.11: a) Comparison of the number of detections before and after the application of the denoising algorithm. b) Comparison of the SNR between original data and denoised data.

2.3 Microseismic activity: Automatic detection and location with Bartlett algorithm

In the previous sections, we focused on the MRABF approach: removing sources on the surface that generate surface noise in order to focus on the microseismic sources in the depth. However, in some cases we lowered the amplitude of the stack. It might mean that the first eigencomponents carry information about the microseismic signal. It indicates that we can locate microseismic events without separating different components of the CSDM. We can directly detect microseismic activity by using appropriate algorithms based on Bartlett and MVDR processor and individual time windows. In this chapter we discuss a new approach for microseismic detection and location.

2.3.1 Velocity optimization

First, we consider an optimization of the apparent P-wave velocity per patch. The optimal velocity maximizes the output of the Bartlett processor (similarly as in the Chapter 1 with surface waves). To optimize the P-wave velocity, we use signal originating from one of the perforation shots. The position of the perforation shot and its approximate origin time are known. We work with a time window $\vec{d}(t)$ of 1.5 s defined from the origin time of the perforation shot.

We normalize the complex data vector $\vec{d}(\omega)$ by its amplitude for each frequency, to give the same weight to each sensor in the location process. Note, that here CSDM $K(\omega)$ is calculated with only one data vector $\vec{d}(\omega)$:

$$K(\omega) = \vec{d}(\omega)\vec{d}^{H}(\omega) \tag{2.10}$$

Then, we calculate the Bartlett processor in a 3D spatial grid centered at the position of the perforation shot.

$$B_{Bartlett}(\omega, a) = \sum_{\omega} |\vec{d}^{H}(\omega, a)K(\omega)\vec{d}(\omega, a)| \tag{2.11}$$

where a - distance between receivers in a patch and a position on a 3D grid.

The optimal velocity for the relative location is vp = 4466 m/s. We define a vector of apparent velocities v_i in the range of 2466 m/s to 6466 m/s. For each velocity v_i, we calculate the modeled Green's function. The Bartlett processor is calculated for each patch on a spatial grid 1300 m x 1300 m x 1300 m with a step 100 m. The optimal velocity is the one that maximizes the Bartlett output within the grid. The Bartlett output is incoherently summed over 30 frequencies in a frequency band (10-60) Hz.

2.3.2 Spatial smoothing processing

The rank of matrix $K(\omega)$ in equation 2.10 equals to 1. CSDM is a singular matrix in this example, so we cannot use the MVDR algorithm. However, we might apply a Spatial Smoothing Processing (Shan and Kailath, 1985) in order to increase the rank of matrix $K(\omega)$. Spatial Smoothing Processing (SSP) consists of defining smaller sub-arrays within an array of receivers. In the considered acquisition, there are N receivers within one patch array. We define regular sub-patches with L receivers. The vector data $\vec{d}^{\alpha}(\omega)$ for L receivers, where L < N yields:

$$\vec{d}^{\alpha} = (d_1, \ldots, d_L) \tag{2.12}$$

Now, CSDM calculated for a sub-array:

$$K(\omega) = \vec{d}^{\alpha}(\omega)(\vec{d}^{\alpha}(\omega))^{H} \tag{2.13}$$

We perform a spatial average over the sub-patches:

$$\bar{K_{\alpha}} = \frac{1}{P}\sum_{i=p}^{P} K_P^{\alpha} \tag{2.14}$$

where P is the number of sub-patches within a patch.

A new vector replica $\vec{d}_l^{\alpha}(\omega, a)$ is calculated for an array of L elements that is centred in the middle of a patch.

$$\vec{d}_l^{\alpha}(\omega, a) = \exp\left(\frac{i\omega a_l}{c}\right) \tag{2.15}$$

where a_l - distance between the receiver r_l within an array and a position in 3D grid, c – optimized velocity per patch.

The MVDR algorithm is calculated with the inverse of a spatially averaged matrix $\bar{K}$:

$$B^{\alpha}_{MVDR}(\omega, a) = \sum_{\omega} \frac{1}{|\vec{d}^{\alpha}(\omega, a)^H \bar{K_{\alpha}}^{-1}(\omega)\vec{d}^{\alpha}(\omega, a)|} \tag{2.16}$$

The MVDR output is incoherently summed over 30 frequencies in a frequency band (10-60) Hz.

Figure 2.12 presents a re-location of the perforation shot with a) Bartlett and b) MVDR with SSP method on a regular grid 1300 m x 1300 m x 1300 m with a spatial step 100 m. Three patches (16, 38, 47) with optimized velocities: 3466 m/s, 3966 m/s, 2966 m/s were used. In order to obtain a final ambiguity map, we use the arithmetic mean for the Bartlett's output and the geometric mean for the MVDR's output. The cross-sections of the ambiguity maps are taken at the maximum's position. The black stars show the theoretical position of the perforation shot.

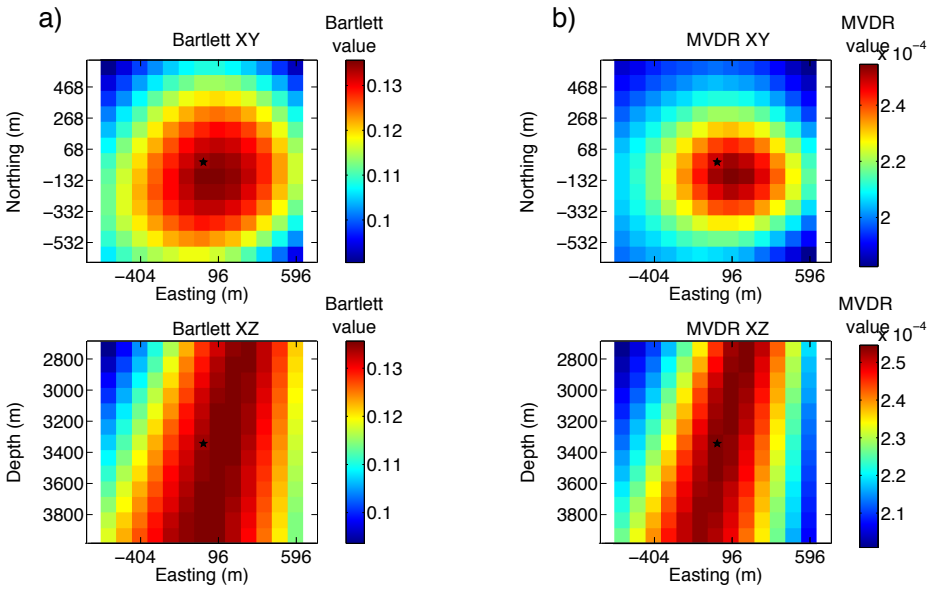

Figure 2.12: Re-location of a perforation shot with a) Bartlett and b) MVDR method with SSP. Three patches (16, 38, 47) with optimized velocities: 3466 m/s, 3966 m/s, 2966 m/s were used. Figures show the focal spots calculated with the two algorithms on a regular grid 1300 m x 1300 m x 1300 m with a spatial step 100 m. The black stars show the theoretical position of the perforation shot.

Note a higher spatial resolution of the MVDR output. This is due to the SSP that was applied for the MVDR (a sub-patch of dimensions: 2x6). The horizontal misfit between the theoretical and found position of the perforation shot is: 250 m for the Bartlett processor; and: 180 m for the MVDR processor. The horizontal misfit for the location obtained with the relative method is of 130 m. The delocalization of the perforation shot might be due to the use of a homogenous velocity model that does not fully explain the propagation of the P-waves. However, we should interpret these results not as a punctual event, but as a zone of microseismic noise. The position of the perforation shot is located within the focal spot of both Bartlett and MVDR ambiguity maps. It means that we can detect and locate microseismic activity only by using Bartlett or MVDR algorithm. However, in the following, we do not use the SSP for locations due to its lower stability in comparison to Bartlett processor.

2.3.3 Minimization algorithm

In the previous sections, we used a grid search to locate sources at the surface and at depth. However, grid search is not the most efficient solution. It is possible to detect sources using a minimization algorithm. We use a MATLAB minimization function called "fminbndsearch". It uses the simplex search method of Lagarias et al. (1998) to find the minimum. It is a constrained multivariable nonlinear programming solver that seeks the minimum of a problem specified by:

$$min_{x,y,z} f(x,y,z) \text{ such that } x_1 < x < x_2,\ y_1 < y < y_2,\ z_1 < z < z_2 \tag{2.17}$$

This function returns a scalar and depends on 3 variables: coordinates x, y, z. In practice, this function looks for a position in space that maximizes the value of Bartlett algorithm (that means: minimizes the value of $-Bartlett(x,y,z)$). This method is fast; it does not depend on the dimensions or on a spatial step of the grid. Note that this method does not provide the ambiguity map (as did grid search), but only coordinates of a point that corresponds to the maximum of the ambiguity map.

Now, we develop a detection and location workflow based on the minimization algorithm:

1. We select 17 patches in the vicinity of the well (Figure 2.9, patches in blue).

2. We work with 2.5 s sliding windows (with an overlap of 0.5 s). For each time window we calculate the CSDM.

3. Then, the minimization algorithm looks for a position (x_0, y_0, z_0) within specified limits that minimizes the value of $-Bartlett(x,y,z)$. The limits are relative to the center of the stage: (x_c, y_c, z_c). The horizontal limits are large: $x_c - 2000\ m < x_0 < x_c + 2000\ m$ and $y_c - 2000\ m < y_0 < y_c + 2000\ m$. The vertical limits are restricted to events only on the depths $z_c - 500\ m < z_0 < z_c + 500\ m$

2.3.4 Detection with Bartlett algorithm and a homogenous velocity model

Before we present the results of detection and locations, we discuss the use of a homogenous velocity model with an absolute location. We now consider a pre-located strong microseismic event recorded on 17 patches (794 receivers in total (Figure 2.13a)). We apply a linear moveout LMO to the microseismic event using the position of the event and a velocity. We apply a linear moveout correction to each trace:

$$t_j = \frac{v}{d_j} \tag{2.18}$$

Where: v is a velocity per patch and d_j is the distance between a localized microseismic event position and a position of a receiver r_j.

First, we use the previously optimized apparent velocities of P-waves. On Figure 2.13b we observe that the arrivals are aligned per patch, however patches are not aligned between each other. The apparent velocity per patch aligns the arrivals within a patch array. However, in order to align the arrivals between the patches we should introduce another velocity that would correct the discrepancy between the patches. We may compare this situation to phase- and group-velocities of surface waves: phase velocities are not enough to align arrivals between the patches (Chapter 1, figure 1.9). It was necessary to find group velocities between a pair of patches to align the inter-patch arrivals. However, in the case of body waves we should be able to align all the arrivals with one velocity model.

This is the reason why we repeat the same test using a homogenous velocity model (vp = 4467 m/s): Figure 2.13c. The arrivals are well aligned using the homogenous velocity approach. We observe a clear change of polarities (negative polarities for the first 390 receivers and positive polarities for the rest) that is due to the focal mechanism. If we sum these arrivals, the stack will be partly destructive due to the change of polarity. The alignment with homogenous velocity is not perfect; there are some residues due to the part of geology that is not explained with a homogenous velocity and the influence of the near surface. However, it still might be used in microseismic event detection and location with MFP.

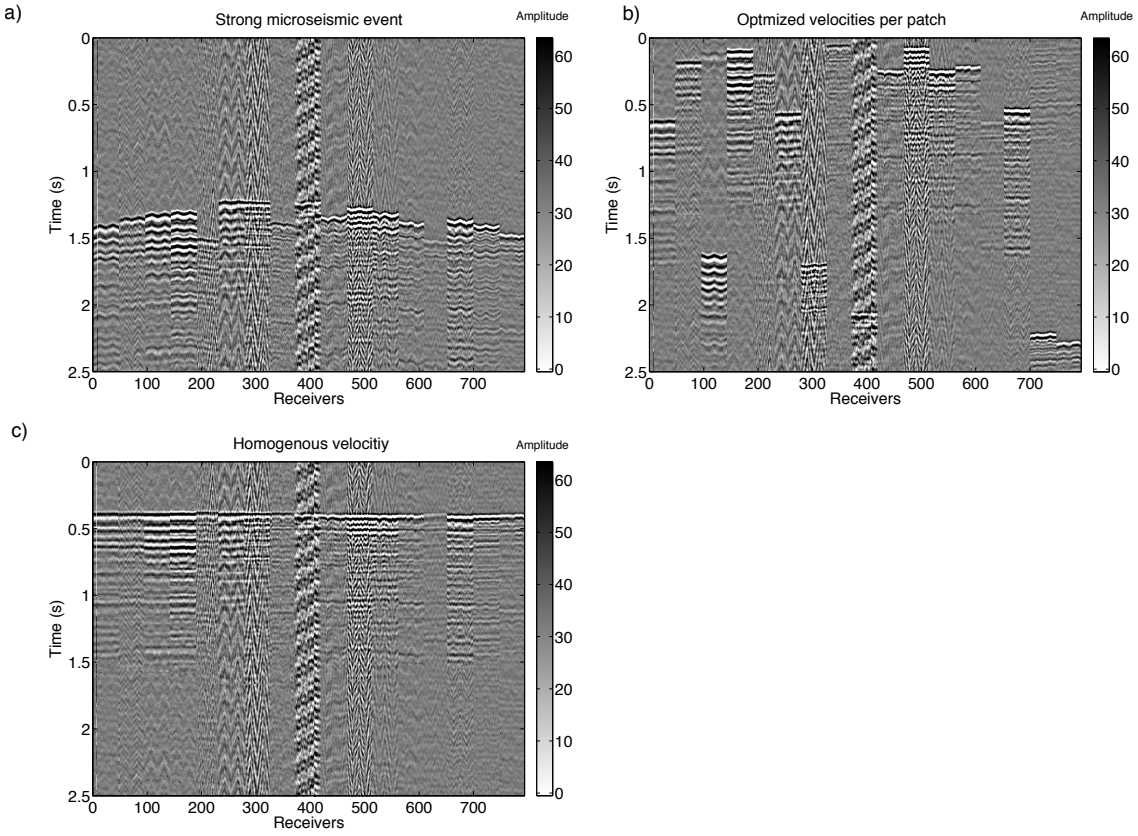

Figure 2.13: a) A strong microseismic event recorded on a set of 17 patches. Microseimic event aligned with a LMO using: b) Optimized velocities per patch; c) A homogenous velocity model (4466 m/s).

We now apply the detection and location algorithm to continuous microseismic data (2.5 h of recording) to detect and localize microseismic activity. We take exactly the same data range that was processed with a relative detection and location method in order to compare our results.

Automatic detection and location of microseismic noise: patches used jointly

First, patches are processed in a joint manner. The complex data vector $\vec{d}(\omega) =$ $= (d_1(\omega), \ldots, d_{NP}(\omega))$ contains the data amplitude and phase recorded over the N sensors within the P patches ($N \cdot P$ elements, here: 794 receivers in total). We normalize each component by its amplitude. Then, the CSDM is calculated using one data vector for all the patches. Finally, we match a modeled Green's function obtained with a homogenous velocity model to the CSDM using Bartlett processor. The criterion of the localization is purely geometrical: we assume that the algorithm located correctly some microseismic activity if the position is found within the grid (locations on the borders are excluded). The detection and location was performed in the (10-60) Hz frequency band using an incoherent sum over 30 frequencies.

This method turned out to be highly sensitive. The joint use of patches strongly decreases the coherence of surface noise, while preserving the coherence of downhole signals. It results in numerous detections. To correctly interpret the results, we project all the locations on a regular grid. One cell of the grid has dimensions of 10 m x 10 m x 10 m. Figure 2.14 shows all the detections projected on the grid. The color-scale corresponds to the sum of Bartlett amplitudes of all the detections within one grid-cell. Weak Bartlett's amplitudes are due to a lower coherence and different polarities between the patches, and the averaging of the Bartlett's value over an important number of receivers (794). Figure 2.15 shows a histogram of all detections. The majority of the events is detected with a Bartlett amplitude of 0.005. There are single detections with stronger Bartlett amplitude (up to 0.14), but for the simplicity of the display we represent detections up to 0.02. This histogram can be used to improve the final image by selecting detections within a give range of amplitudes (not shown here).

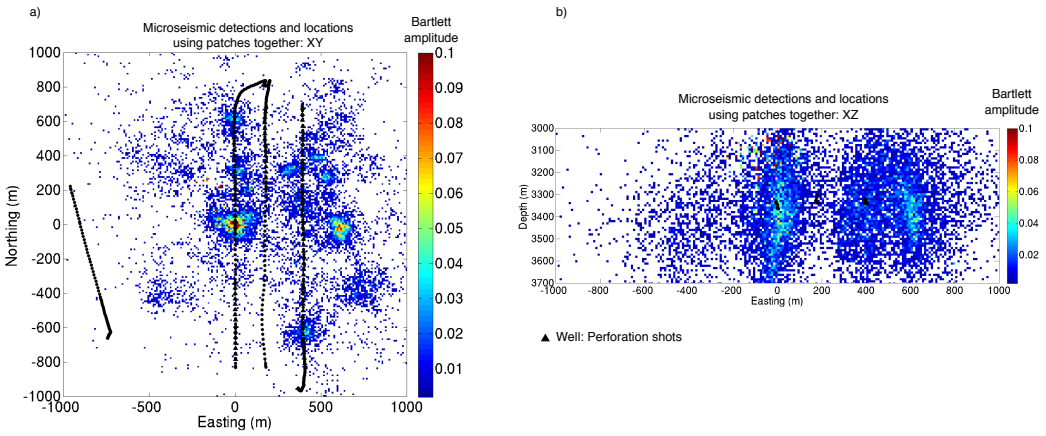

Figure 2.14: Detection and location in a joint manner using 17 patches with a homogenous velocity model and the Bartlett algorithm: a) horizontal view and b) vertical view. Results of detection and location are projected on within 10 m x 10 m x 10 m cells.

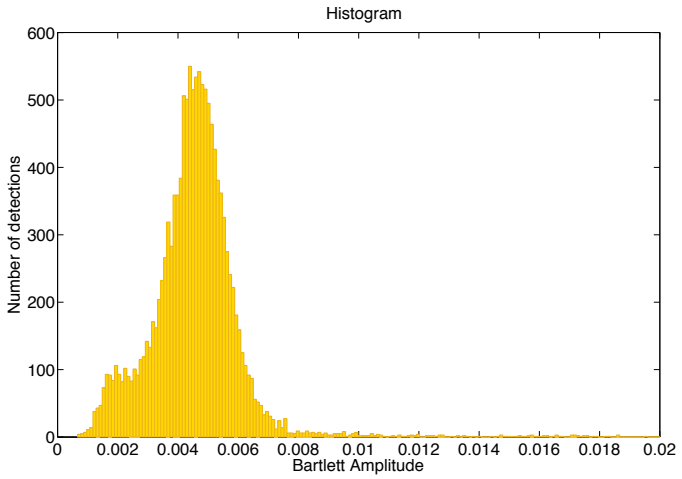

Figure 2.15: Histogram of Bartlett values of detections in a joint manner using 17 patches with a homogenous velocity model and the Bartlett algorithm.

The length of the time window (2.5 s) is large compared to the duration of an actual microseismic event. Microseism event is a signal of an impulsive character in time. By using 2.5 s time windows we integrate information from all the arrivals in this time window. It means, that we can detect the actual, punctual miroseismic events, but also other downhole signals (for example: Long-Period, Long-Duration seismic events (Das and Zoback (2013)). Moreover, any leaks in a casing of a well (fluid injection leaks, gas leaks) can produce detectable signal. Also, gas bubbling up through liquid in the wellbore can cause noise (Koerner and Carrol (1979)). These signals consists of downhole noise and can be detected with the presented method. Note that one time window can provide only one detection.

Figure 2.14 shows a few zones of higher downhole activity. The main one corresponds to the microseismic activity around stimulated area (Figure 2.16). It is located in the position exactly corresponding to the hydraulic fracturing operations (perforation shots). We also observe some other cluster of events that are grouped mainly around the well. Note that in spite of the large horizontal limits in the processing, all the activity is located within the vicinity of the well. Microseismic monitoring has proven that hydraulic fractures are complex, with fractures often showing a long fracture length. Moreover, hydraulic fractures often interact with pre-existing fractures in the reservoir which might create an entire fracture network (Maxwell et al. (2011)).

On Figure 2.16 we see the zoom on the primary downhole noise zone. We represent previous results of the relative detection and location in pink (400 events). The positions of the punctual events are located within the main noise zone found with our method. We also represent the temporal evolution of the microseismicity in this zone (we choose the detections located < 150 m from the center of the stage). Here, we sum the detections over 2.5 s due to the overlap of the times windows.

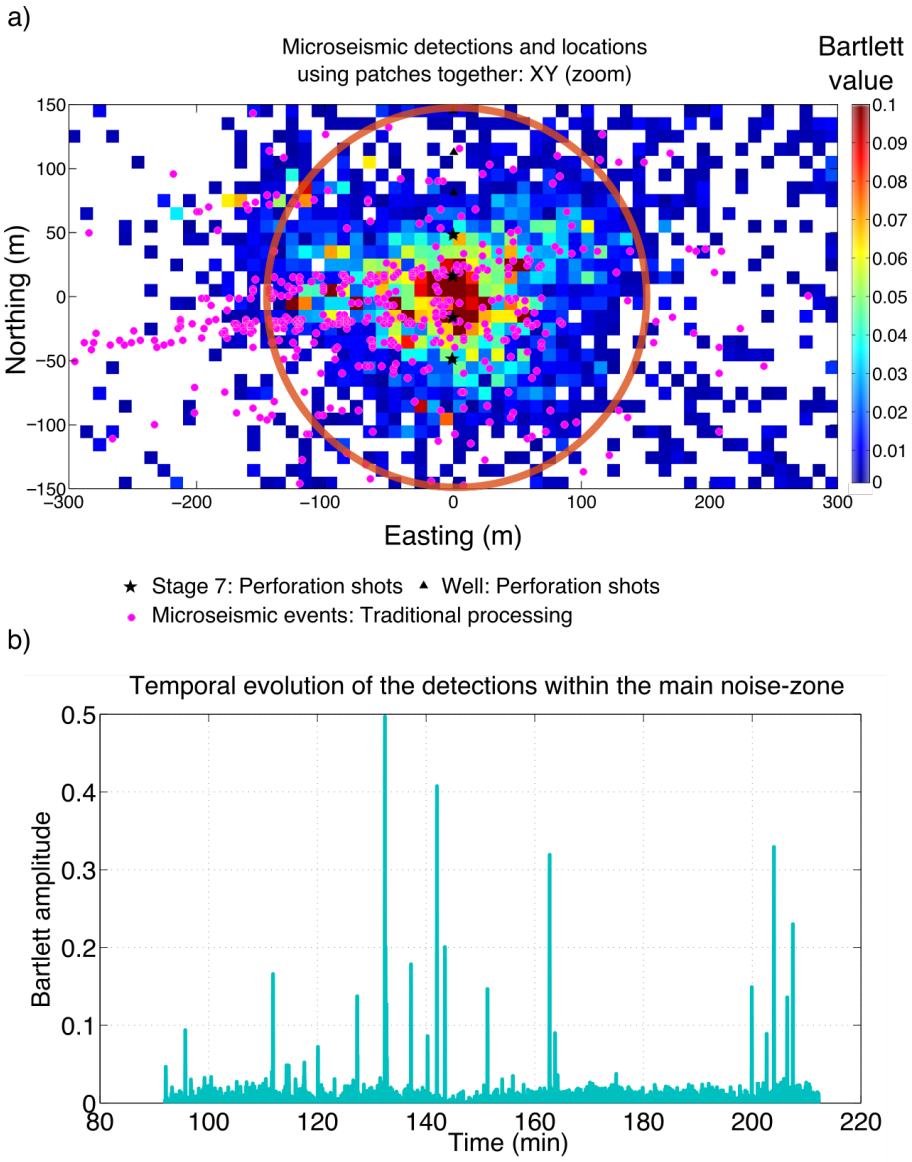

Figure 2.16: Zoom on the principal microseismic activity zone: a) spatial evolution of detections. The red circle represent the spatial limit of the detections (< 150 m) used to calculate the temporal evolution in b).

Note this method does not provide directly the origin time of the event. Similarly to the spatial dimension, we detect microseismic activity in a certain time range, not as a punctual event. Note that the peak of detections corresponds to the peak of amplitude spectrum; they appear at the same time ∼130 min (Figure 2.10).

This approach provides spatial and temporal information about the medium with a minimum of a priori knowledge. The only a priori is the homogenous velocity. Also, this method is completely automatic. Using an optimized velocity model could increase the values of Bartlett output. However, our idea was to show how much information we can retrieve about the medium by using

a completely automatic approach with almost no a priori.

Automatic detection and location with Bartett algorithm: patches used separately

In this section we also use the minimization of the $-Bartlett(x, y, z)$ function to locate and detect microseismic events. However, in this example we work patch by patch. At first, we represent the location obtained with a single patch. Figure 2.17 represents all detections for patch 10, 20, 26 and 39. The color-scale corresponds to the Bartlett amplitudes. If patches are used individually, they are more sensitivity to noise sources on the surface than on the depth. Here, we represent all the detections with a partial geometrical exclusion: we do not represent events that are located on the borders of the XY grid. However, those located on the border of the Z grid are presented.

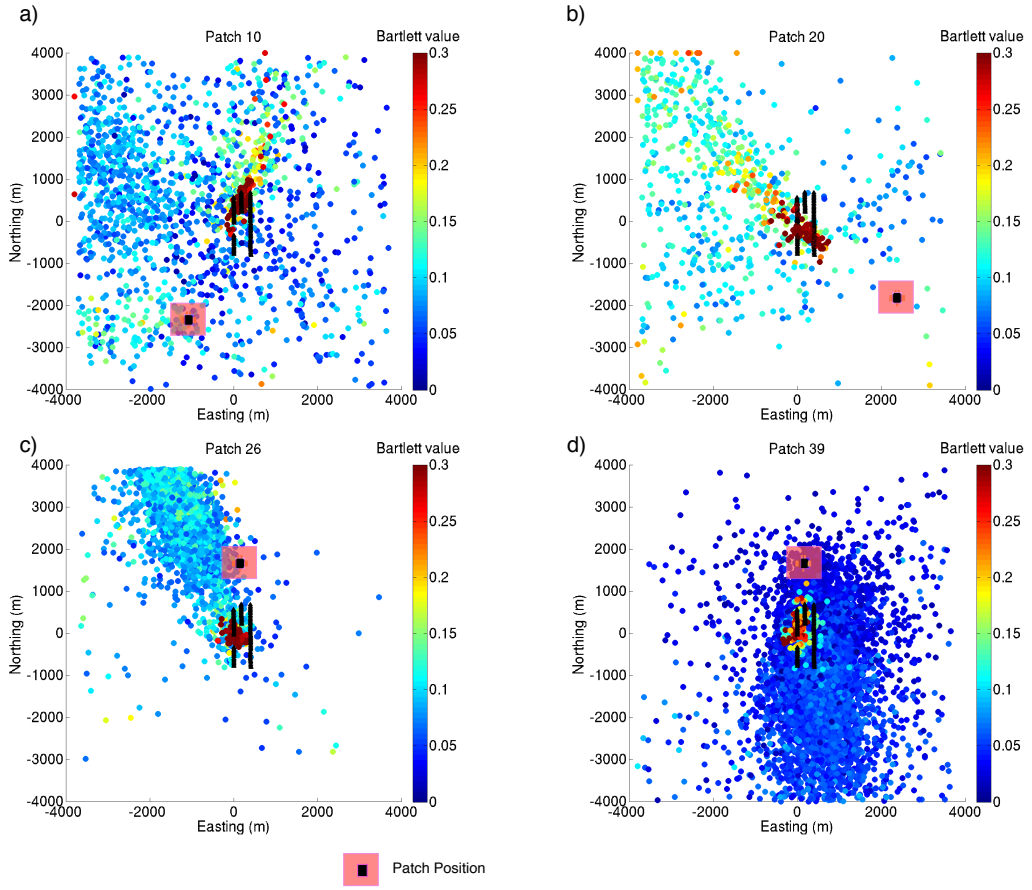

Figure 2.17: Detection and location per patch with a homogenous velocity model and the Bartlett algorithm. Horizontal views for patch: a) 10, b) 20, c) 26, c) 39.

The algorithm is forced to focalize on the depth. The detections of the surface sources are placed on the upper border of the Z grid with low amplitudes. We observe that the actual mi-

croseismic noise is detected but delocalized. However, we are able to extract some information about the downhole signals even with one patch. Note the contrast in amplitudes for the detections around the well area (in red: high amplitudes) and on the outside (in blue: low amplitudes). Now, we use the 17 patches to detect microseismic signals, but in a separate manner. The minimization algorithm seek positions that maximize the sum of Bartlett processors per patch:

$$min_{x,y,z} f(x,y,z) = min(-\sum_i Bartlett_i(x,y,z)) \tag{2.19}$$

such that $x_1 < x < x_2, y_1 < y < y_2, z_1 < z < z_2$. Where $Bartlett_i(x,y,z)$ it is the Bartellt value calculated for a patch.

The results of detections are presented on Figure 2.18. On Figure 2.18a we show only the locations that are not on the XY grid borders (but can be on located the Z grid border) and on Figure 2.18b we show the locations that are not on the Z grid border. The color-scale corresponds to the Bartlett amplitudes of microseismic detections. If we work per patch, we observe relatively strong Bartlett amplitudes (due to a higher coherence inside a patch, the same polarity, and a normalization by a low number of elements within one patch). We observe better focalizations of events compared to the results per single patch. The noise zones on the surface (blue points) and on the depth (red points) are easily distinguishable.

This method is more sensitivity to the noise on the surface, which results in a low number of detections at depth (73 detected microseismic events). It means that noise from the surface is strongly coherent within a patch, even in the frequencies above 10 Hz. However, this method is still obtained with a minimum of a priori, it's automatic, it does not need any template. We also tested this detection method combining it with the denoising algorithm. It increases the sensibility of detection, although events are delocalized. We also tested a relative approach but it did not increase the sensitivity of the method.

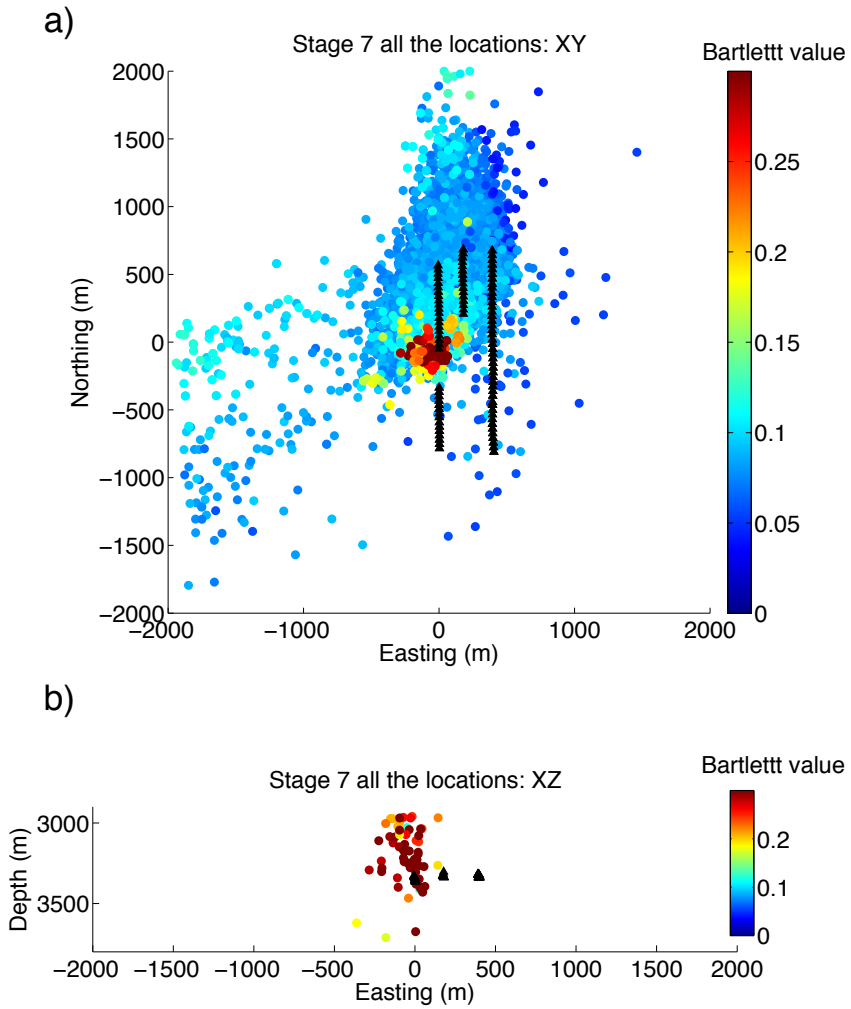

Figure 2.18: Detection and location per patch in a separate manner using 35 patches with a homogenous velocity model and the Bartlett algorithm: a) horizontal view and b) vertical view.

2.4 Conclusions

In this chapter we presented different applications of Matched Field Processing in microseismic monitoring. Benefitting from the acquisition with patches we developed methods that are automatic and require almost no a priori information.

The proposed denoising algorithm can reduce the impact of surface waves on microseismic data. As a consequence, the number of false detections is reduced. Moreover, it can help to find new events that were buried in noise. This technique does not need any a priori information and requires only three user-specified parameters. Future works could consist in finding a criterion for the removal of eigencomponents. The number of eigenvalues to be removed ideally should be introduced as a function of frequency. One of the possible criterions could be a focalization on the depth. This would help to preserve the microseismic signal.

We also presented two approaches for direct detection and location of microseismic noise with MFP. Grid-search allows visualizing the results of the detection in space. The spatial smoothing processing permits the use of MVDR algorithm with a single time window. It enhances the resolution of the ambiguity map, although this algorithm is less robust than the Bartlett processor. This is why we use Bartlett algorithm to detect and locate microseismic events. To enhance the efficiency of calculations, we introduced a minimization algorithm.

Surface noise is highly coherent within a patch. However, the joint use of patches strongly decreases the coherence of surface noise, while preserving the coherence of downhole signals. In consequence, we observe significantly more detections if patches are used in a joint manner (one vector data for all the receivers).

We use a homogenous velocity model in the MFP. It allows us to successfully localize areas generating microseismic noise. The results of our processing might help to better understand the origin of the downhole noise and to distinguish between possible noise sources (e.g., downhole noise, microseismic activity or long-period, long duration seismic events). Moreover, it might help to imagine complex fracture networks in the reservoir. This method is easy to apply and opens a route to continuous, easily implemented, purely automatic reservoir monitoring. Possible applications can be envisaged in monitoring of volcanic, geyser or other seismic activity.

In the perspective, we migh use an optimized velocity model for localization or a relative approach with MFP. Furthermore, it would be interesting to compare the results with geological maps and injection curves.

Chapter 3

Producing data-based sensitivity kernels from convolution and correlation in exploration geophysics.

This chapter presents interferometric techniques used with dense active seismic configuration. We present different approaches to define a stationary phase zone. Especially, we focus on sensitivity kernels: model- and data- based. Moreover, we study the retrieval of surface wave Green's functions with correlations and convolutions.

3.1 Active seismic acquisition

The data used in this study was acquired during a survey of the natural gas over a 42-km2 area in Tunisia (Figure 3.1). The data was recorded on 10 710 vertical receivers using 51 808 sources (seismic vibrator trucks). Seismic vibrator is a truck that generates a long and a low-power signal, which is called the sweep (Figure 3.2). The sweep is generated within a limited bandwidth, during a long time (Postel et al. (2005)). A single vibrator is sweeping a broad bandwidth from 2 Hz to 100 Hz during 20 s. This signal is sent into the Earth and then cross-correlated with the recorded data to reveal reflection events. Very low frequencies are hard to obtain in active experiments: the use of active sources in low frequency regime might be too destructive. However, low frequency improves the vertical resolution and facilitates the exploration of deep targets.

The sources spacing is the same in both x and y directions (30 m) which is known as a "carpet shooting". The receivers are placed in parallel lines with a spacing 150 m in the x direction and 30 m in the y direction. One trace is a sum of 6 tightly clustered vertical geophones.

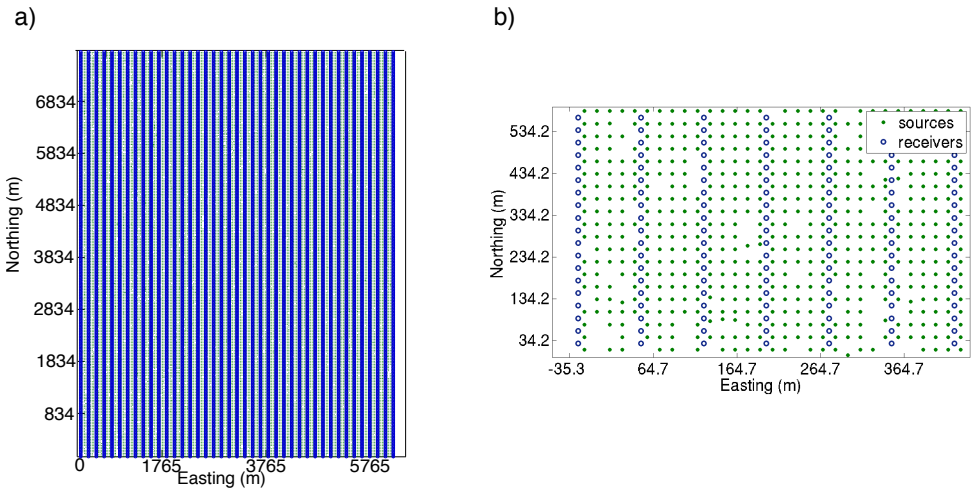

Figure 3.1: a) Active seismic acquisition. In this survey the technique of carpets shooting was applied for a natural gas survey over a 42-km2 area in Tunisia. The x-y coordinates are relative to the position of source with minimum Easting and Northing coordinates. b) Zoom on the area of 2-km2 of the active seismic survey. The sources spacing is the same in both x and y (30 m). The receivers are placed in parallel lines with a spacing 150 m in x direction and 30 m in y direction. The presented coordinates are relative to the position of the first source.

Figure 3.2: Seismic vibrator. This truck emits the sweep into the Earth in the frequency range: (5-250) Hz (courtasy: CGG).

3.1.1 Surface waves in active seismic acquisition

In exploration geophysics, surface waves are often the strongest arrivals. Due to the common use of only vertical sensors the most important surface waves are the Rayleigh waves. Usually,

they are the most energetic part of the seismic recording. In general, surface waves (also called ground-roll) are considered to be noise. Surface waves are dispersive, it means that their phase velocity changes with frequencies. Their dispersion depends on the complexity of the near surface field.

Different methods are used to minimize the impact of the noise wavefield, depending on its properties. Usually, the signals are stacked along the reflection moveout to cancel the shot generated noise as well as the ambient noise. The effectiveness of the noise cancellation increases with the trace number. Trace density is therefore an effective solution to reach the highest signal to noise ratio at all depth levels.

Of course, surface waves can also provide important information about the shallow structures. Phase- and group- velocities maps in a given frequency range can be inverted to obtain S-wave (sometimes P-wave) velocity models for the near surface. This can add more constraints to seismic migration and improve its results. However, obtaining the phase- and group- velocities maps for surface waves can be challenging. Traditional surface wave tomography has some limitations. It consists of a linear inversion of travel times and it needs a priori information about the medium. This issue can be overcome with Eikonal tomography. However, both methods require the first arrivals picking. Travel time measurements can be quite challenging when dealing with complex waveforms. It is often the case in exploration geophysics.

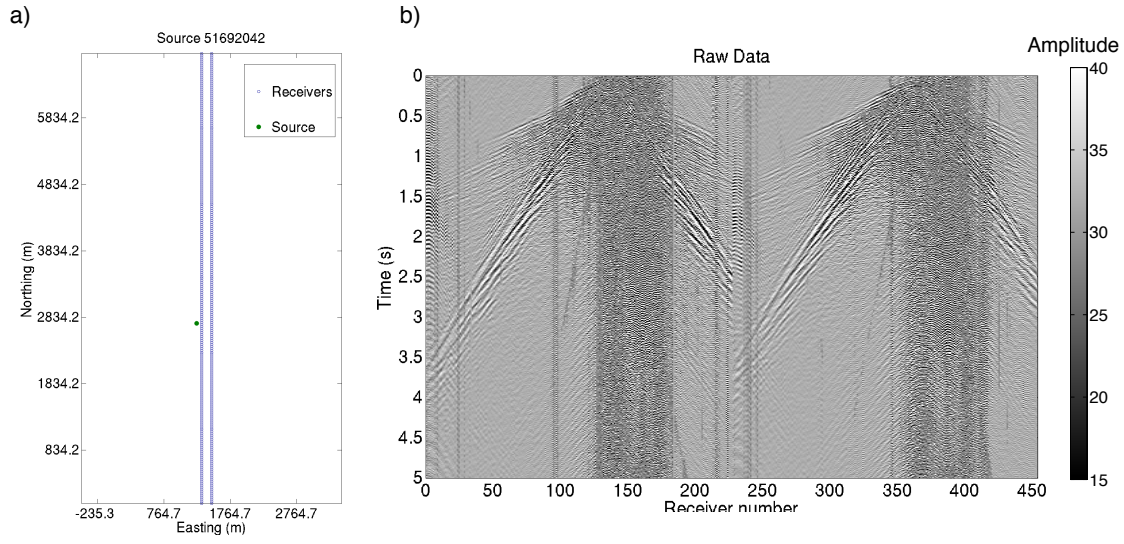

Figure 3.3: Raw data for two lines of receivers and a source. a) Position of the source and 2 lines of receivers; coordinates are relative to the position of the first source; b) data recorded on the receivers for the source. Note the surface waves that are more energetic then the body waves.

In a classical seismic acquisition on the Earth's surface, surface waves are often more ener-

getic than the reflection data (Figure 3.3b). They are created while the sweep is sent into the Earth. They can be present up to 30 Hz (which is the case here) or even in higher frequency bands. Also, depending on the offset of receivers they can be aliased that can make it more difficult to remove them or to pick the travel times. Many algorithms and acquisition strategies have been developed in order to extract the surface waves or use them more efficiently. Naturally, the optimal algorithms are the ones that provide high quality results in an automatic way.

3.2 Green's function retrieval: Virtual receivers and virtual sources.

3.2.1 Green's function retrieval

Green's function is a displacement field generated by an unidirectional unit impulse, which has a precise location in both space and time (Aki and Richards (1980)). In the case of an equipartitioned wavefield, the cross-correlation of two recordings between two points converge towards the complete Green's function between these two points, including all the propagation modes, reflections and diffractions (Weaver (2005)). Many studies have investigated the emergence of Green's function from ambient noise cross-correlations. The Green's function retrieval was demonstrated in: acoustics and elastic plates (Lobkis and Weaver (2001); Weaver and Lobkis (2001); Larose et al. (2004); Sabra et al. (2008)), seismology (Paul and Campillo (2001); Shapiro and Campillo (2004), Shapiro et al. (2005)); oceanography (Roux and Kuperman (2004)) and seismic exploration (Draganov et al. (2007)).

Mathematically speaking, the derivate of cross-correlations is equal to the difference between causal and anticausal part of Green's function (Roux et al. (2005), Gouédard et al. (2008a)):

$$\frac{d}{dt}\sum_{s} c^{s}_{AB}(t) \propto G_{BA}(t) - G_{AB}(-t) \tag{3.1}$$

where c-is the correlation function in time between points A,B summed over sources s and G is the Green's function.

Seismic interferometry (Schuster et al. (2008)) can be based on correlation and performed with direct waves. It can be used with active sources and passive sources. Bakulin and Calvert (2004) showed possible application of interferometry using active sources in exploration geophysics context. In noise interferometry, long averaging times are often needed in order to converge towards Green's functions. In the case of an active seismic experiment, the recording time is not continuous. Data is recorded separately for each shot and the length of one recording is of a few seconds (often 5 s). However, the equipartition criterion is fulfilled due to the regular distribution of sources and receivers. What is more, the location of sources is known and their density is important. Therefore, seismic acquisition with active, controlled sources gives more possibilities when it comes to interferometry. The use of controlled sources makes it possible to recover the surface wave Green's functions between two points using either correlation or convolution.

In the following, we focus on surface waves. As we saw in the section 3.1.1, surface waves are the dominant direct arrivals on the recorded data. Also, surface waves are most easily extracted, because they dominate the Green function between receivers located at the surface (Shapiro et al. (2005)) and also because they are excited by surface sources.

3.2.2 Source-Receiver Reciprocity

The principle of reciprocity states that traveltime along a given ray is the same disregarding the direction of travel (Sheriff and Geldart (1995)). It means that any source and any receiver might (under some conditions) be interchanged and the same waveform will be observed. This principle can be used to simplify the data collection. There are some cases where this source-receiver reciprocity breaks down, for example in moving fluids (Wapenaar (2006)). One of the aspects of the Green's function retrieval from the cross-correlation functions is built on the reciprocity principle (Wapenaar (2004)). The reciprocity can be defined as:

$$G_{AB}(x_R, t; x_S, 0) = G_{BA}(x_S, t; x_R, 0) \tag{3.2}$$

where G_{AB}, G_{BA} are the Green's functions. Indices for their spatial components and the source and receiver positions have been switched; and x_R symbolizes the position of a receiver and x_S symbolizes the position of a source (e.g., Aki and Richards (1980), Nowack and Chen (1999)).

Figure 3.4 shows the reciprocity principle in practice. We may represent the active seismic data in two collections: source gather (Figure 3.4a, b) and receiver gather (Figure 3.4c, d). Source gather presents wavefield generated by a point source and recorded on receivers. Receiver gather presents wavefields generated by sources and recorded on a receiver. In this example, we represent only the wavefields within the radius of 2000 m for both gathers (source gather: 2516 receivers and receiver gather: 12383 sources). This example shows that the recorded wavefield is reciprocal. We also observe the coherency of two spectrums (Figure 3.5).

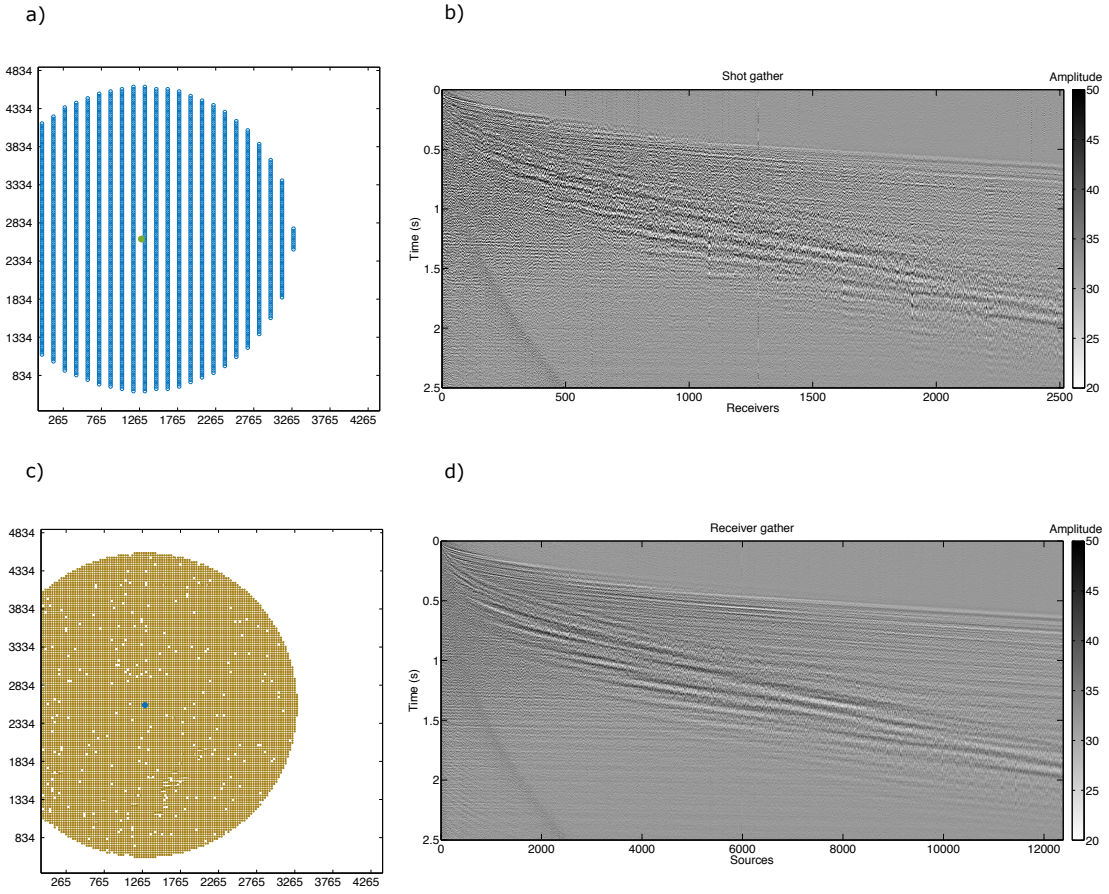

Figure 3.4: Source-receiver reciprocity. a) Map representing the source gather data collection: the source position is marked as a blue dot. b) Source gather collection. This seismic section presents a raw signal recorded on the receivers within the radius of 2000 m from the source. Presented data is arranged by an increasing offset receiver-source. Color scale represents the signals amplitude scaled with a gain: -84 dB. c) Reciprocal geometry for b): Map representing a receiver gather data collection: the receiver position is marked as a blue dot. d) Receiver gather collection. This seismic section presents a raw signal recorded on the receiver for all the sources within the rayon of 2000 m. Presented data is arranged by an increasing offset receiver-source. Color scale represents the signals amplitude scaled with a gain: -201 dB.

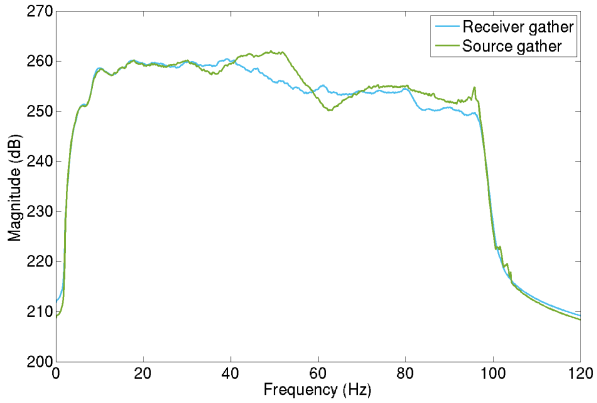

Figure 3.5: A mean spectrum of amplitude for the presented receiver gathers and shot gathers.

3.2.3 Virtual receivers and virtual sources

Seismic interferometry allows to construct an unmeasured wavefield between two points by applying cross-correlation, deconvolution, or convolution to seismic data recordings (Duguid et al. (2011)). Curtis et al. (2009) have demonstrated the possibility of converting earthquakes into "virtual seismometers" by using the correlations. In practice, it means that with inter-receiver interferometry, a virtual source can be constructed at the location of a real receiver with energy from surrounding sources. Reciprocally, a virtual receiver can be constructed at the location of a real source with energy recorded at surrounding receivers with inter-source interferometry.

The following methodology is used to create virtual gathers. In particular, we consider a methodology for a virtual receiver gather, but we follow the same steps to create a virtual source gather.

1. Choose two sources in A and B.

2. Filter and whiten data in a specified frequency band.

3. Cross-correlate two wavefields s_{SA} and s_{SB} recorded at a receiver R_i that were generated by the two sources. We are using a normalized version of the cross-correlation.

$$c_{AB}^{R_i}(t) = \frac{s_{R_iA} \star s_{R_iB}}{\sqrt{E_{R_iA} E_{R_iB}}} \tag{3.3}$$

where: E_{R_iA}, E_{R_iB} are the traces energies.

Normalized cross-correlations are equalled to the coherence function (Jones (2000)). Note that after the spectral whitening, the energy of the trace is the same for all the traces and consists of a constant. For a single frequency the energy of a trace after spectral whitening equals to 1.

4. Sum the cross-correlations for all the R receivers: Virtual receiver: $V_R = \sum_{R_i=1}^{R} c_{AB}^{R_i}(t)$.

Figure 3.4 presents a comparison of a receiver gather a) with a virtual receiver gather collection b) and c). In both cases, data was whitened in the frequency band (2-30) Hz. Note the higher signal to noise ratio of surface waves arrivals for the virtual gather. Also, note the change in the polarity for the negative and positive lag (in agreement with the equation 3.1).

In a classical seismic acquisition on the Earth's surface, surface waves generated by the vibrator truck are often more energetic than the reflection and refraction events (see: Figure 3.3 and Figure 3.4). This is the reason why surface waves are most easily extracted with interferometry, because they dominate the Green's function between receivers located at the surface (Shapiro et al. (2005)).

Virtual receiver gather was obtained summing all the cross-correlations. Each slice represents wavefield recreated at the position of the source. Time slices are taken at 0.5 s, 1 s, 1.5 s, 2 s and 2.5 s. Note, that the virtual gather collection can be created for each source position (51 808 virtual gathers) while receiver gather can be recreated at each receiver position (10 710 real gathers).

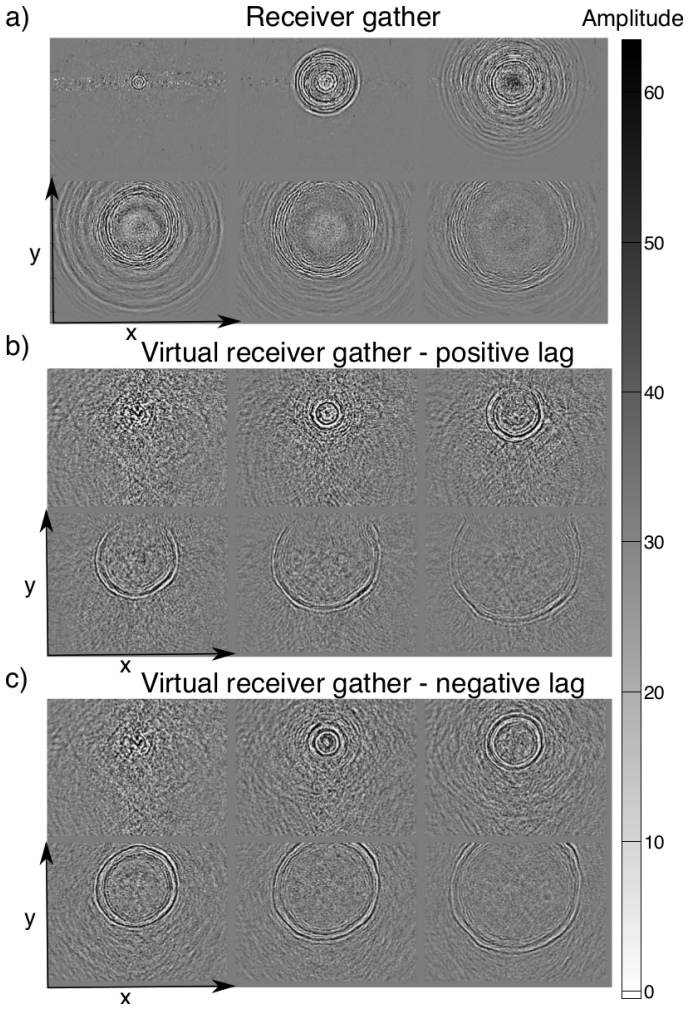

Figure 3.6: Time slices taken at 0.5 s, 1 s, 1.5 s, 2 s and 2.5 s in the frequency band: (2-30) Hz. a) Receiver gather collection. Each slice presents the wavefield excited by all the sources and recorded at the receiver. Color scale represents signals amplitude scaled with a gain -188 dB. b) Virtual receiver gather collection (positive lag). Color scale represents signals amplitude scaled with a gain 57 dB. c) Virtual receiver gather collection (negative lag).

3.3 Stationary phase approximation

The convergence of the noise correlation function towards the Green's function can also be interpreted through the stationary phase theorem (Snieder (2004); Roux et al. (2005), Roux and Kuperman (2004)). Snieder (2004) explained the construction of impulse response with cross-correlations. Observable arrivals are present under the condition of the stationary phase. It means that the main contribution to interferometrically reconstructed inter-receivers Green's function comes from the sources in stationary phase zone (two cones around extensions of the line that connects the two receivers). Therefore, the energy emanated by the sources in other locations

should cancel out.

The stationary phase approximation can be also interpreted as the end-fires lobes (EFL). The EFLs are the areas in which the phase of the correlation function of direct waves is stationary with respect to the azimuth (Roux and Kuperman (2004), Gouédard et al. (2008b)). Even if the sources are not aligned with the two receivers, the main contribution to the average correlation function comes from the sources inside the end-fire beams. Also, we can call the stationary zone the Fresnel zone, as it is the area where the correlated wavefields interfere in a constructive way.

There are different approaches to define the aperture of the stationary phase cones or the EFLs. In the following, we are presenting the methods of: angle approximation, hyperbolic selection, directivity pattern and phase oscillations, which are used to define the stationary phase zone for the direct wave interferometry.

3.3.1 Azimuth selection

The first presented method consists in selecting the stationary phase zone by azimuth (Wapenaar et al. (2010)). Consider the 2D geometry for the inter-sources interferometry shown in Figure 3.7. S1 and S2 are two sources separated by a distance of 1030 m. These sources are surrounded with receivers distributed over a ring (the distance of the receiver to the center of the ring is between 1000 m and 2000 m). The wavefields from the two sources are cross-correlated for each receiver and whiten in the frequency band of (2-7) Hz. The cross-correlation functions obtained from each receiver are stacked by a beam of 1° and plotted as a function of azimuth in Figure 3.7b. Note that these cross-correlation functions strongly depend on the receiver azimuth (sinusoidal dependence).

Next, we sum the cross-correlation functions. It results in the time-symmetric response in Figure 3.7c, with two events at -0.92 s and 0.92 s. This is the response of a source at S1 observed at S2 and its time-reversed version (as shown in 3.1 and in the Appendix A). The stationary points of the cross-correlation function are located within the stationary phase zone. In this example, they are located within the cone of an aperture of 22° (Figure 3.7a, marked in red). Also, we can conduct this analysis a bit further and derive a mean phase velocity of surface waves by fitting a sinus to the correlations gather. The fit with the least squares gave a mean phase velocity of 1174 m/s (Figure 3.8).

In this example the stationary phase angle is derived in an empirical way. Normally, the aperture of the stationary phase zone should be calculated according to the wavelength, which will be shown in the following examples.

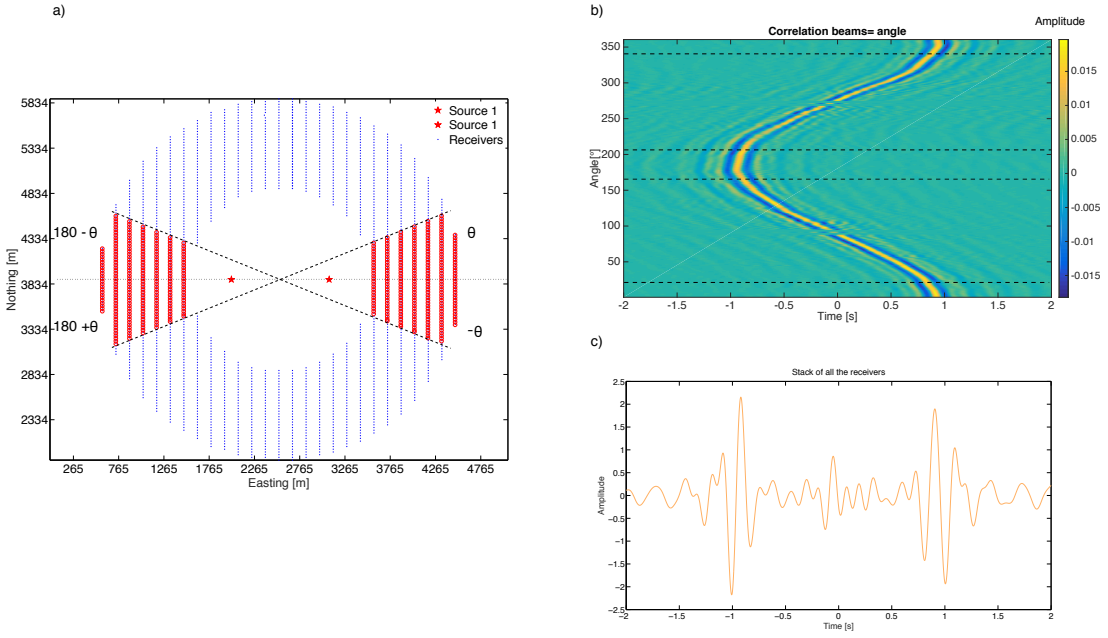

Figure 3.7: a) 2D geometry for the inter-sources interferometry. Distance between the two sources is 1030 m, the ring of receivers: R1 = 1000 m, R2 = 2000 m (counting from the center point). Stationary phase zone is marked for angle theta 22°. b) Cross-correlation function. Cross-correlations were filtered in the frequency band (2-7) Hz and they are arranged by their angle and stacked by the interval of 1°. c) Virtual receiver: stack of all the cross-correlation functions.

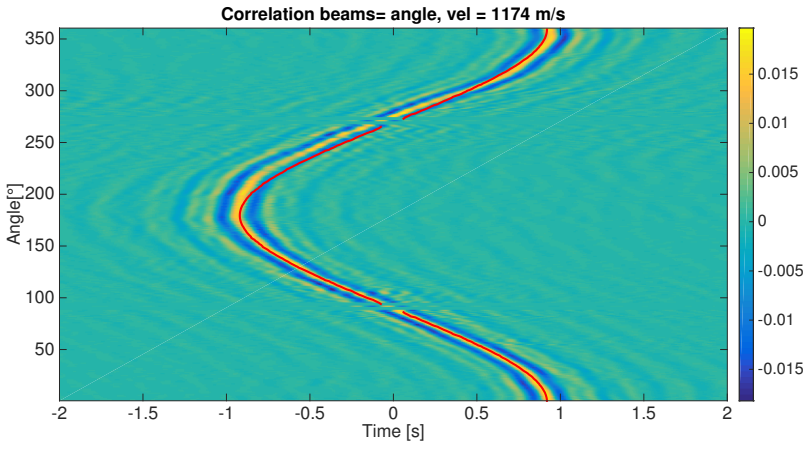

Figure 3.8: Cross-correlation function with a sinus fitted with a mean phase velocity of v = 1174 m/s.

3.3.2 Hyperbolic selection – End Fire Lobes

Another way to calculate the end fire beam is a hyperbolic equation. Roux et al. (2005) have shown that by introducing a geometrical argument, an analytical solution can be obtained for a noise correlation function spatially integrated over source positions. For a 2D geometry, sources (x,y) have to be placed on a hyperbole defined by the equation:

$$y^2 - x^2(\frac{4a^2}{c^2t^2} - 1) = a^2(1 - \frac{c^2t^2}{4a^2}) \tag{3.4}$$

if $ct \neq 0$ and $x = 0$ if $ct = 0$. We calculate y from the equation 3.4 as:

$$y = \sqrt{x^2(\frac{4a^2}{c^2t^2} - 1) + a^2(1 - \frac{c^2t^2}{4a^2})} \tag{3.5}$$

where: a is the mid-distance between two receivers in A (a,0) and B (-a,0) (Figure 3.9) and for a time t satisfying a condition -2a < = ct <= 2a.

The hyperboles in Figure 3.9 correspond to the sources in a 2D section that will contribute to the cross-correlation function at a given time t.

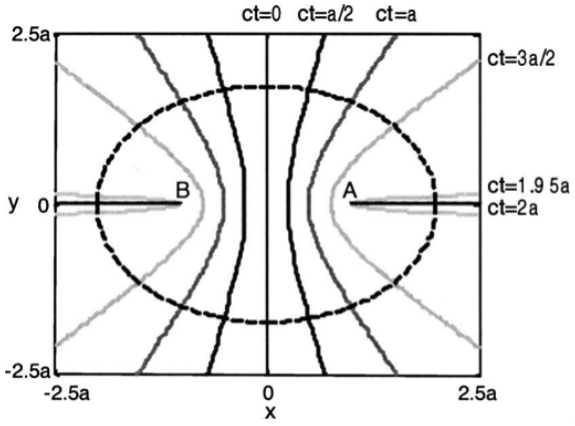

Figure 3.9: Representation in the xy plane of the hyperbola that contributes to a given time t in the noise correlation function. The receivers A and B are at (a,0) and (-a,0) (after Roux et al. (2005)).

In this section, we use the equation 3.5 and the previously presented 2D geometry (3.7), to define the time hyperboles. To calculate the hyperboles, we use a mean phase velocity of 1174 m/s (as derived in the previous section). The distance between the two sources is equal to: 2a = 1030 m. Each hyperbole on the Figure 3.10a contributes to the following times: t= (-1.95, -1.5, -1, -0.5, -0.05, 0.05, 0.5, 1, 1.5, 1.95) a/c, which gives 10 hyperbolas with different aperture. In this example, the stationary phase zone can be determined with an aperture of a hyperbole (for example limited to the time t > 1.95 a/c). The colorscale represents the time of direct arrivals pointed per trace. We see that receivers that contribute the most to the final stack are located within the first hyperbole. The data was filtered in the frequency band of (2-7) Hz. Figure 3.10b

presents the cross-correlation functions stacked by 360 hyperboles and plotted as a function of $c \cdot t$. Note, the linear dependence of $c \cdot t$ on a in the cross-correlation function. The phase velocity can be derived by calculating the slope of the cross-correlation functions, which is equal to $(c \cdot t)/t = a/t$

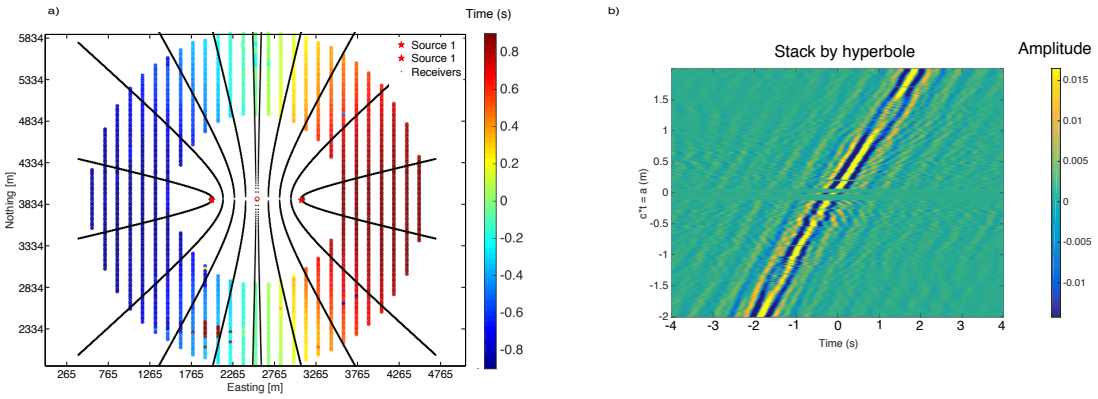

Figure 3.10: Hyperbolic selection of the stationary phase zone. a) Hyperbolas defined with the equation 3.5 with the velocity = 1174 m/s and the times t = (-1.95, -1.5, -1, -0.5, -0.05, 0.05, 0.5,1, 1.5, 1.95) a/c. b) The cross-correlations functions stacked by 360 hyperboles and plotted as a function of $c \cdot t$.

3.3.3 Directivity pattern

Another way of defining the EFL is based on the directivity pattern. The directional dependence of the radiation and reception of seismic sources and receivers can be quantified by their directivity. Different definitions can be found for directivity patterns, but in general they are all frequency dependent functions (Pollow (2015)). Roux et al. (2005) derive the directivity pattern for EFL as:

$$B(\delta\theta) \cong 1 - \frac{\delta\theta^4}{8}\left(\frac{R}{c}\right)^2\left(\omega^2 + \frac{\Delta\omega^2}{12}\right) \tag{3.6}$$

where B is the directivity pattern, $\omega = 2\pi f$ the central angular frequency, and $\Delta\omega$ the frequency bandwidth, $\delta\theta$ the aperture of the EFL, R is the distance between the two sources and c is the mean phase velocity.

The EFL of the pair of sources are the areas located in the axis of the two sources (on each side) with an aperture $\delta\theta$ from the equation 3.7 (Figure 3.11).

$$\delta\theta = 2\sqrt{2\frac{c}{R}}\sqrt[4]{\frac{1-B}{\omega^2 + \frac{\Delta\omega^2}{12}}} \tag{3.7}$$

In other words, the EFLs are areas in which the phase of the correlation function of direct waves is stationary. Figure 3.11 represents the EFL calculated for two sources with the distance R =

3100 m, B = 0.8 (phase shift is up to 1/5th of the period), c = 1174 m/s and ω = 4.5 Hz and $\Delta\omega$ = 5 Hz, which gives the $\delta\theta = 0.3°$. Note that in this example we include the receivers in the closest vicinity of the sources, contrary to the previous examples.

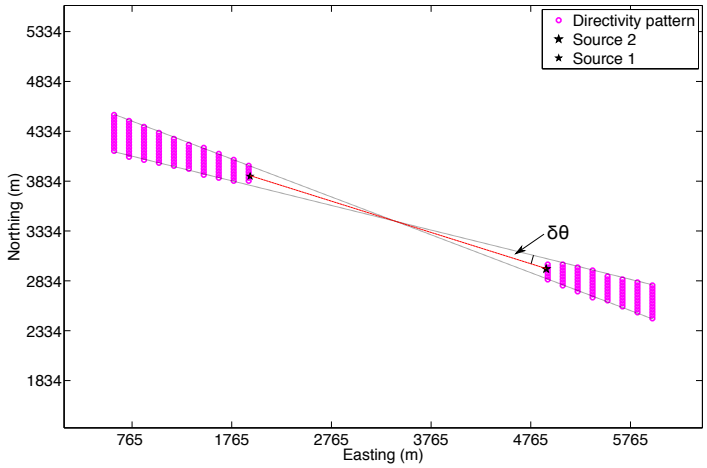

Figure 3.11: EFL calculated using the directivity pattern (in pink) where $\delta\theta = 0.3°$. The distance between the two sources is 3.1 km.

Spectral whitening of the active seismic data

We now consider the construction of a virtual receiver using the presented geometry (Figure 3.11), the positive lag in particular. Figure 3.12a shows the receivers participating in the creation of the positive lag of cross-correlations (8 lines of receivers, the distance between each line is of 150 m). Figure 3.12b represents wavefield generated by s1 and s2 recorded on the receivers. The data is filtered in the frequency band (2-30) Hz, without the spectral whitening.

In the noise cross-correlations, spectral normalization acts to broaden the band of the ambient noise signal, and also to avoid strong dominant spectral peaks in the background noise (Bensen et al. (2008)). However, one may ask: do we really need the spectral whitening in the case of an active seismic data? We now consider the wavefield from source 2 processed without the spectral whitening (Figure 3.12b) and with it (Figure 3.12c). We observe, that the spectral whitening reduces the effects of the near-field on the amplitude. Moreover, it limits the impact of high-frequencies damping in the medium. After the spectral whitening, the amplitudes of cross-correlations of surface waves (observed at 3 s) are strongly equilibrated (Figure 3.12c). Also, note the cross-correlations of surface waves from source 1 with P-waves from source 2 (observed at 1.5 s). However, they do not interfere constructively.

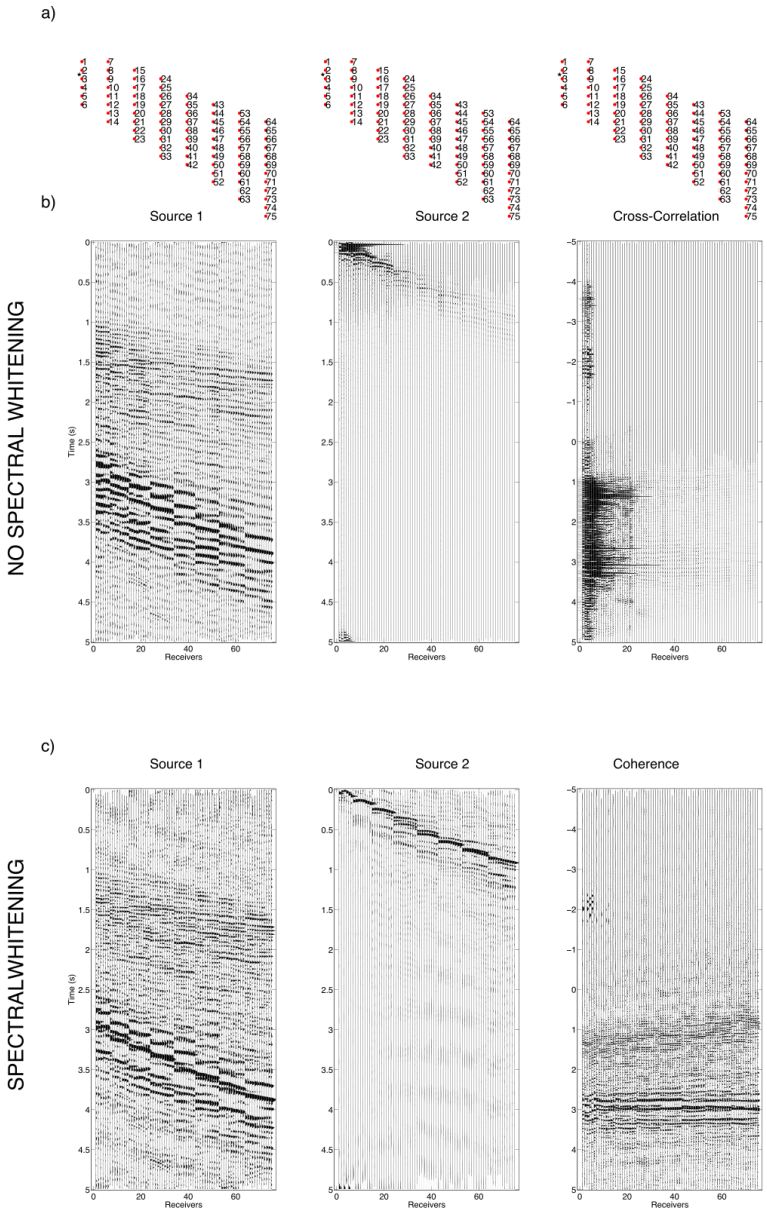

Figure 3.12: Spectral whitening of active seismic data. a) Receivers participating in the construction of the positive lag of cross-correlations. b) Signal recorded at the receivers generated by source 1 and source 2. The signal was filtered in the frequency band (2-30) Hz and correlated. c) Signal recorded at the receivers for source 1 and source 2. The signal was whitened in the frequency band (2-30) Hz, correlated and normalized by the energy of a trace.

3.3.4 Sensitivity Kernels

Each of the previous methods shows a different approach for deriving the stationary phase zone. However, these methods are not directly based on the coherence measurements. For the case of an isotropic wavefield distribution, there is a well-defined connection between the ex-

pected value of the wave coherence over the sensors and the wave propagation (Eckart (1953), Cox (1973)). Walker (2012) explored the influence of ambient field directionality on the relationship between the measured wave coherence and sensor-to-sensor propagation. This behavior is a simple consequence of Huygens–Fresnel principle. Let's consider a following 2D geometry (Figure 3.13), where a source point is in s and two receivers are in r1 and r2:

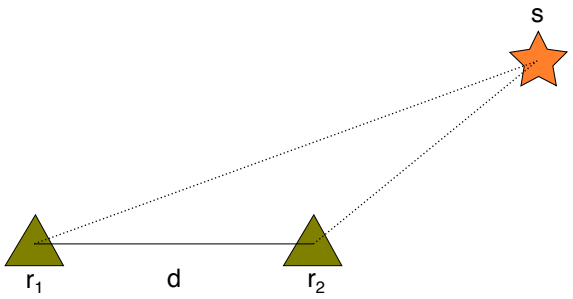

Figure 3.13: Scheme of two sensors in: r1 and r2 that are separated by distance d and source in s.

The aperture size is the sensor separation: d. The criterion of interference for a monochromatic wave depends on the length of the path difference:

$|sr_1| - |sr_2| = \frac{2n+1}{2}\lambda$ - destructive interference

$|sr_1| - |sr_2| = \frac{2n}{2}\lambda$ - constructive interference

where n is a natural number and λ is a wavelength.

In the case where the source is align with the receivers axis: $|sr_1| - |sr_2| = d$. It means that depending on the wavelength we might observe the destructive or constructive interference pattern, even in the direction aligned with the receivers axis. However, two waves can be subject to a constructive interference or a destructive interference and still be coherent (that is to say to have a constant phase difference at the same frequency).

The contrast of interference can be quantified by the interferometric visibility, which is also known as fringe visibility (Born and Wolf (1999)). When two waves interfere and the phase difference between them varies as a function of space, the power of intensity of the arising wave oscillates, which results in an interference pattern. The oscillations of intensity in space are due to interference and are called fringes. The interferometric visibility is related to the measure of coherence between two wavefields. The decrease in coherence will result in decrease of the visibility.

We now consider a frequency dependent Green's function between two points 1 (in $\vec{r}_1$) and 2 (in $\vec{r}_2$) in the case of a homogenous medium without attenuation:

$$G(\vec{r}_2, \vec{r}_1, \omega) = \frac{1}{|\vec{r}_2 - \vec{r}_1|} exp\left(i\omega\left(t - \frac{|\vec{r}_2 - \vec{r}_1|}{c}\right)\right) \tag{3.8}$$

Where: c – wave velocity

We define another function G^0 that is based only on the phase between points: 1 and 2 and a source s (in $\vec{r}_s$), we skip the amplitude factor. In some cases, only the phase of the recorded signal is used. Indeed, the phase is more sensitive than the amplitude in coherent processing (Jensen et al. (2011)).

$$G_1^0(\vec{r}_S, \vec{r}_1, \omega) = \exp\left(i\omega\left(t - \frac{|\vec{r}_S - \vec{r}_1|}{c}\right)\right) = \exp\left(i\omega t_1\right) \tag{3.9}$$

$$G_2^0(\vec{r}_S, \vec{r}_2, \omega) = \exp\left(i\omega\left(t - \frac{|\vec{r}_S - \vec{r}_2|}{c}\right)\right) = \exp\left(i\omega t_2\right) \tag{3.10}$$

where: t_1 - propagation time from the source s to the receiver 1, t_2 - propagation time from the source s to the receiver 2, $\omega = 2\pi f$ the central angular frequency.

Energy of the Green's function (equations 3.9, 3.10) reads:

$$E = |G^0(\omega)^2| = 1 \tag{3.11}$$

Now, the correlation of the two modeled Green's function gives:

$$Corr_{1,2}(\omega) = G_1^0(\vec{r}_S, \vec{r}_1, \omega) G_2^0(\vec{r}_S, \vec{r}_2, \omega)^* = \exp\left(i\omega\left(t_1 - t_2\right)\right) \tag{3.12}$$

where the asterisk denotes complex conjugation.

To quantify the contribution to the spatial coherence between field locations r1 and r2 arising from the source location s and the scale of the phase oscillations, we are going to use the aperture diffraction kernel (Walker (2012)). This kernel is based on the correlation function:

$$K(\omega) = \exp\left(i\omega\left(\frac{d}{c} - (t_1 - t_2)\right)\right) \tag{3.13}$$

We call the function $K(\omega)$ a phase sensitivity kernel function. We develop this idea in the next section. Equation 3.13 gives the expression of the aperture diffraction kernel for a single frequency, which results in strong phase oscillations (Figure 3.14a). We can smooth the oscillations by integrating the function K over a given frequency band: (ω_1, ω_2).

$$\int_{\omega_1}^{\omega_2} \exp\left(i\omega\left(\frac{d}{c} - (t_2 - t_1)\right)\right) = \Delta\omega \exp\left(i\omega_0\left(\frac{d}{c} - (t_2 - t_1)\right)\right) \mathrm{sinc}\left(\frac{\Delta\omega}{2}\left(\frac{d}{c} - (t_2 - t_1)\right)\right) \tag{3.14}$$

where: $\omega_1 = \omega_0 - \frac{\Delta\omega}{2}$ and $\omega_2 = \omega_0 + \frac{\Delta\omega}{2}$.

Energy of the Green's function (equation 3.9) integrated over the same frequency band yields:

$$E = |\int_{\omega_1}^{\omega_2} G^0(\omega)| = \Delta\omega \tag{3.15}$$

We define another function H that is normalized by the energy of the Green's function:

$$H(\omega) = \exp\left(i\omega_0\left(\frac{d}{c} - (t_2 - t_1\right)\right) \mathrm{sinc}\left(\frac{\Delta\omega}{2}\left(\frac{d}{c} - (t_2 - t_1)\right)\right) \tag{3.16}$$

In the following, only the real part of the kernel functions is represented: $\Re(K(\omega))$ and $\Re(H(\omega))$.

The spatial representation of aperture diffraction kernel for d = 1020 m, c = 1100 m/s is presented on the Figure 3.14 (Figure 3.14a: function $K(\omega)$ at the frequency 7Hz, and Figure 3.14b function $H(\omega)$ for the frequency band (4-10) Hz). Note, that the presented configuration consists of source-source interferometry. Kernel functions are presented only for the receivers located outside the two sources.

Note the decrease in the fringe visibility for the kernel in the frequency band (4-10) Hz (Figure 3.14). Moreover, we observe the inversion of the contrast in the fringes. These phenomenon are due to the interefence of different wave-lengths in the broadband processing.

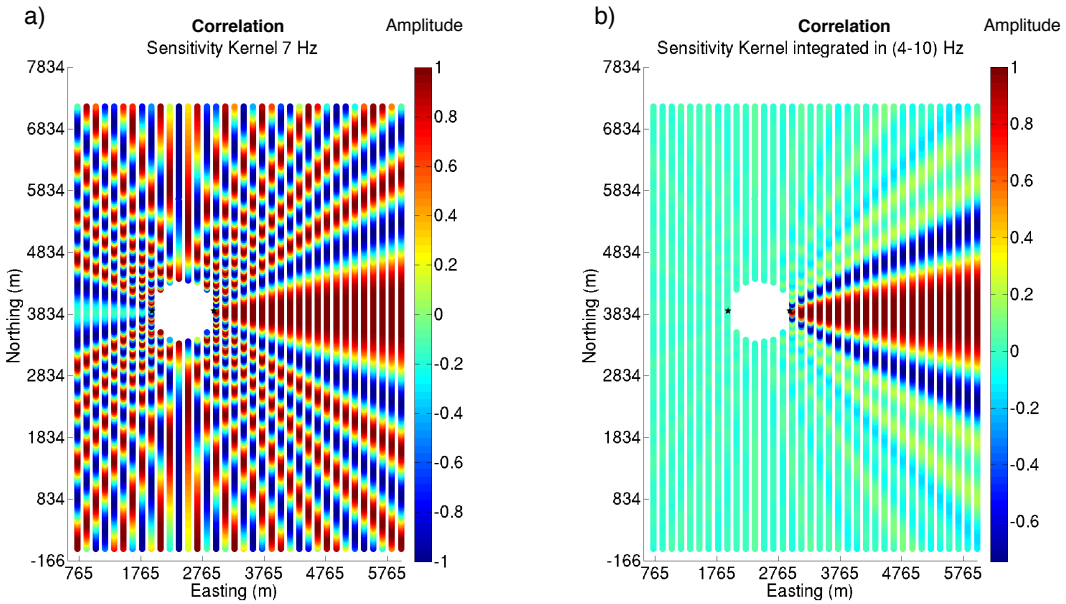

Figure 3.14: Theoretical phase sensitivity Kernels for two sources 1020 m apart, calculated using a velocity 1100 m/s: a) for a single frequency of 7 Hz, b) integrated in the frequency band (4-10) Hz. Sources positions are presented as black stars.

Virtual trace: stack improvements

The zone over which surface waves are coherent in phase is defined as the first Fresnel zone (the first phase oscillation aligned with sources axis). All the receivers located within the first phase oscillation, where the amplitude of the kernel is higher or equal to 0, belong to the stationary phase zone. An example of the first Fresnel zone is presented on the Figure 3.15a. Note, that it is the same configuration as in the section 3.3.3 (the distance between the two sources is 3100 m). This theoretical kernel was calculated for the frequency band (1-4) Hz. We now use the amplitude of the kernel to define a taper. This taper will smooth sharp edges effects of the stationary phase

selection, which should improve the quality of the virtual trace. The weights w_i of the taper correspond to the amplitude of the kernel function at the receiver R_i. This taper can be applied before summing the cross-correlation functions in order to improve the quality of the stack:

$$V_R = \frac{1}{\sum w_i} \sum_{i=1}^{N} w_i c_{R_i} \tag{3.17}$$

where $w_i = H(r_i, \omega)$ and c_{R_i}-correlation at the receiver R_i.

Another possible application of the taper consists in stacking the cross-correlation functions per line of receivers (L line of receivers with n_l receivers within each line):

$$V_R = \frac{1}{L} \sum_{l=1}^{L} \frac{1}{n_l} \sum_{i=1}^{n_l} w_i c_{R_i} \tag{3.18}$$

where L – is the number of receivers lines.

Figure 3.15 compares different methods of stacking the cross-correlation functions. The best result is obtained with the taper and the sum per line of receivers with a near field correction (exclusion of the receivers within the distance of $\lambda/2$) increased the maximum of the stack of the virtual traces (from 0.49 to 0.55). However, it is a second order improvement; the value of the maximum is increased by 10%.

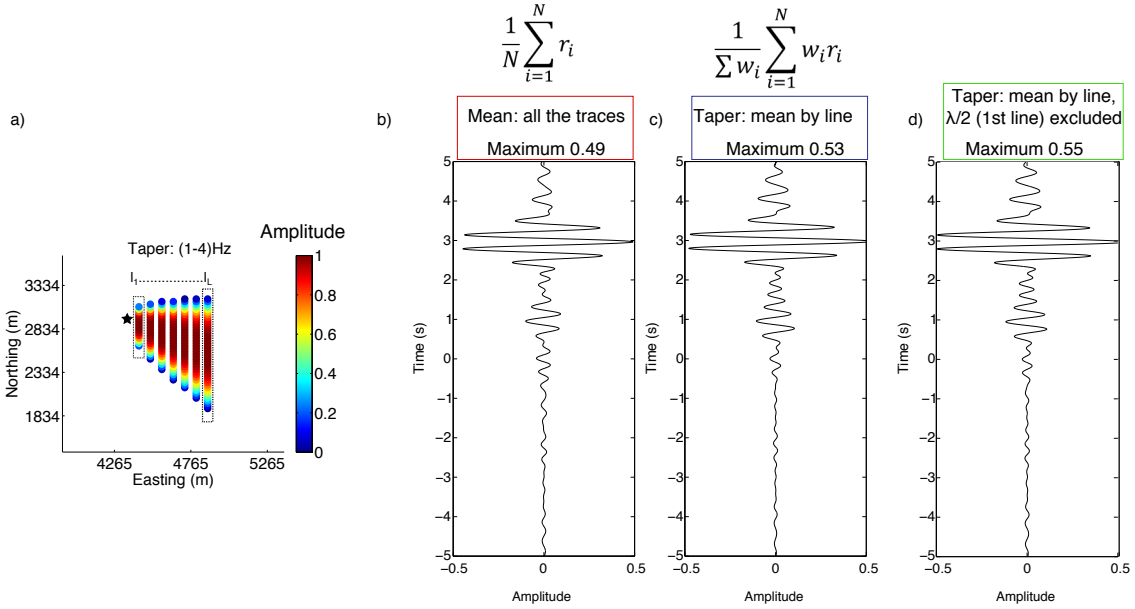

Figure 3.15: a) Taper defined with sensitivity Kernels for the acquisition geometry presented in Figure 3.11 with a velocity 1100 m/s and the frequency band (1-4) Hz. b) Stack of all the cross-correlations; b) All the cross-correlations are weighted with the taper amplitude; stacked per lines; c) All the cross-correlations are weighted and stacked as in b) but the correction of the near field is added.

Virtual receiver gather: FK

The selection of the Fresnel zone with the Kernel function and the previously presented weighted stack is considered as an optimal processing for a creation of virtual-traces. Now, we create a complete virtual gather using this method. We use a 2D geometry (Figure 3.16a.): a line of 131 sources with spacing 30 m surrounded with receivers. For each point source we apply the previously presented methodology. The virtual receivers gather is created in the frequency band (1-20) Hz (Figure 3.16b). The negative time lag is represented as a negative offset. Next, a two-dimensional Fourier transform (frequency-wavelength) is calculated (Figure 3.16c). Note the discontinuity of the F-K transform at around 8 Hz. It might correspond to a superior mode of surface waves that is set off at this frequency.The separation of modes becomes visible as the offset increases (from $\sim$ 1000 m, Figure 3.16b). The apparent mean velocities are of: 1180 m/s (2-8 Hz) and 1340 m/s (8-20) Hz.

To further investigate this discontinuity we recreated the virtual receiver gather in a narrow frequency band, centered at 8 Hz: (6-10) Hz (Figure 3.17). Figure 3.17a shows a periodic increase and decrease in wave amplitude (a beating pattern), especially for the positive offsets. It is caused by the interference of two waves in this frequency band: a fundamental mode with a superior mode of surface waves. The F-K diagram shows a secondary maximum that can be interpreted as a higher mode of surface waves.

We discuss the higher modes of surfaces waves and possible techniques of their separation in the following chapters.

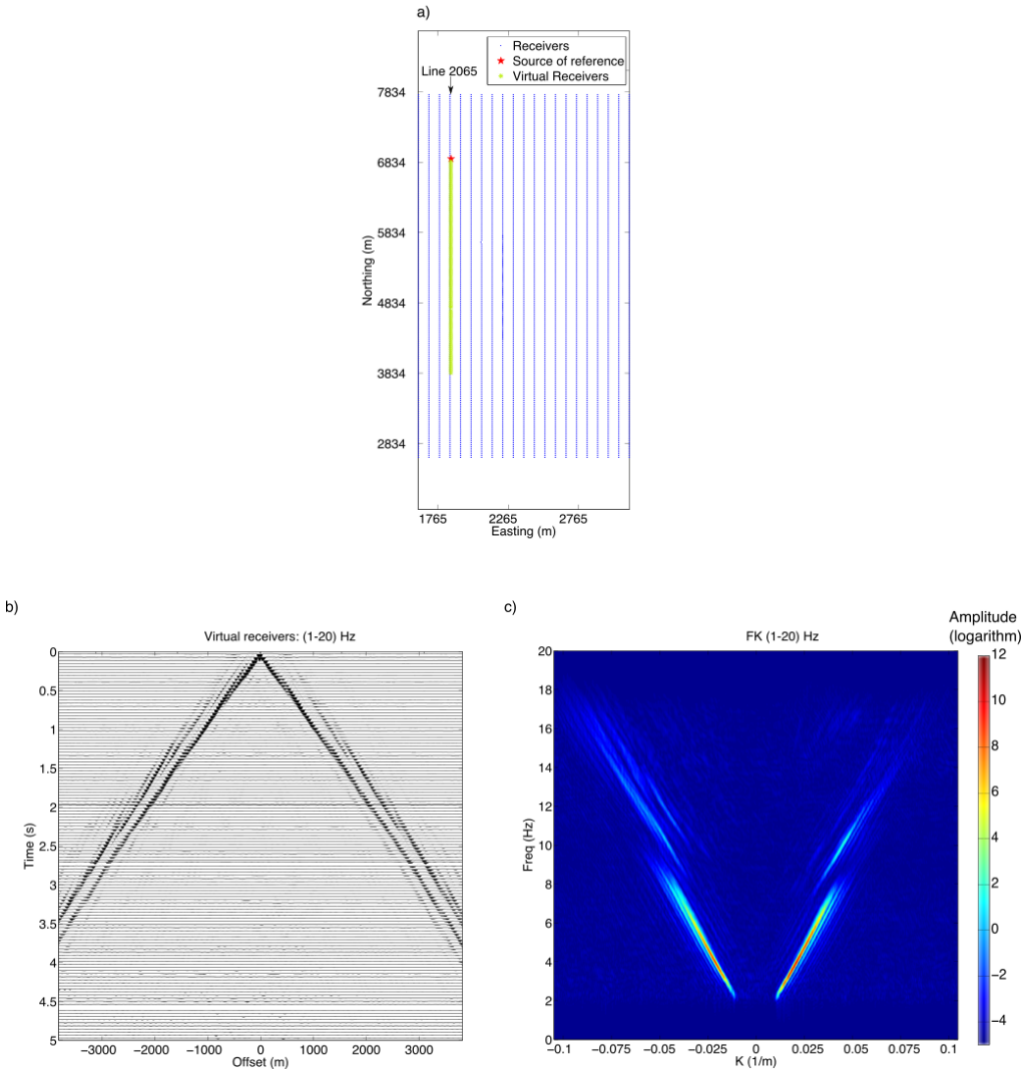

Figure 3.16: a) 2D geometry for the virtual receivers construction. Blue dots represent the position of receivers, the red star show the position of the source (virtual receiver) of reference and green dots show the position of the line of sources (virtual receivers). b) The line of virtual receivers for the frequency band of (1-20) Hz. Note, that the negative time lag was represented as a negative offset. c) F-K transform of the previous figure. Note the appearance of the second mode of surface wave from the frequency 8 Hz.

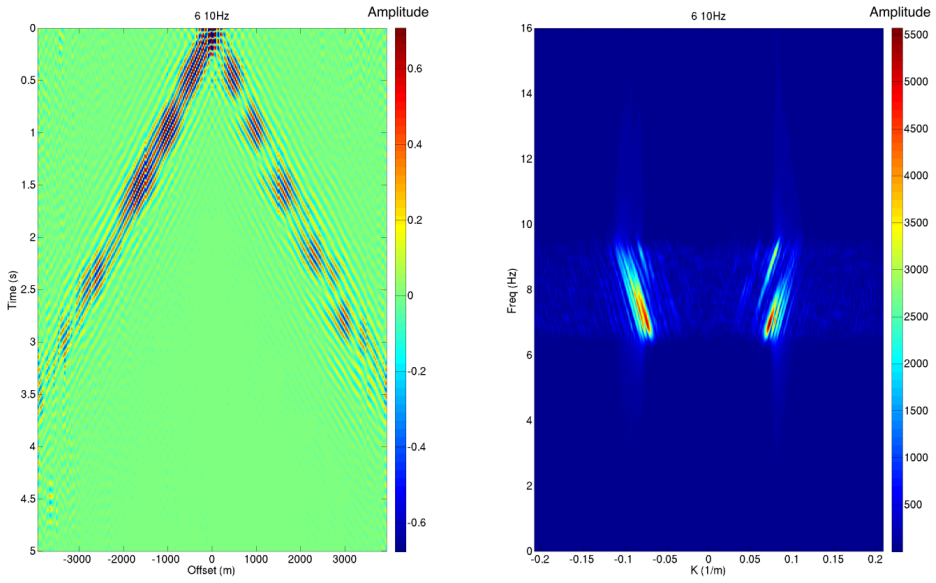

Figure 3.17: a) The line of virtual receivers created in the frequency band of (6-10) Hz. The negative time lag was represented as a negative offset. Note the beating pattern in the waveform, especially for the positive offsets. b) F-K transform.

3.4 Data based sensitivity kernels

In general, sensitivity kernels show how specific measurements react to perturbations of elastic properties anywhere in the medium (de Vos et al. (2013)). The sensitivity kernels can be used for surface wave tomography. They can replace ray theory that interprets local relative phase shifts along great circle propagation. Ray theory is valid in the infinite frequency approach, when the scale of heterogeneous structure is larger than the wavelength. However, if the scale of heterogeneities is about the wavelength or smaller, we should consider the finite-frequency effects. In 2004, Zhou et al. determined 3D sensitivity kernels for surface waves based on the single-scattering (Born) approximation on the Earth surface. In 2006, Yang and Forsyth derive 2D sensitivity (phase and amplitude) kernels for fundamental-mode Rayleigh waves also based on the single-scattering approximation. These are examples of sensitivity kernels calculated for source-receiver geometries, based on phase difference.

However, sensitivity kernels for Rayleigh waves based on a noise cross-correlation function with station-station geometry were also studied (Tromp et al. (2010), Nishida (2011)). In particular, Tromp et al. (2010) measured a misfit between observed and simulated noise cross-correlation functions to determine corresponding sensitivity kernels. Such kernels involve interactions between ‘forward’ and ‘adjoint’ wavefields (Tarantola (1988); Tromp et al. (2005); Fichtner et al.

(2006); Liu and Tromp (2006)). The principal application of adjoint models is sensitivity analysis. Sensitvity gives information about how a selected measure will react to perturbations to a certain property in the medium. If we need to quantify the sensitvity a mathematical model is required. An adjoint model gives a first-order approximation to sensitivity in a nonlinear model Errico (1997). The adjoint wavefield is excited by an adjoint source and travels backward in time from the receiver to the source (de Vos et al. (2013)). Adjoint calculations can be quite complicated.

We propose an alternative approach to derive the sensitivity kernels. The Fresnel zones at a given frequency provide the propagation path for surface waves (Yoshizawa and Kennett (2002)). We benefit from the homogenous source distribution to calculate phase sensitivity kernels. We showed in the previous section that a cross-correlation function between a pair of stations provides the wave propagation between them (the Green's function). Similarly to Eikonal tomography (Lin et al. (2009)), we are assuming that a cross-correlation function has sensitivity along the ray path between a pair of stations. In this section we derive the 2D sensitivity kernels for Rayleigh waves based on correlations and convolutions. These sensitivity kernels will be subsequently used to produce phase-velocity dispersion relations between two points and to separate the higher mode from the fundamental mode for surface waves. Potential application to surface wave cancellation is also envisaged.

Following Zhou et al. (2004), we deal with phase perturbations between receivers in 1 and 2 and we define the 2D data-based sensitivity kernel as:

$$\partial\varphi_{Corr_{1,2}} = \int_{\vec{r}_s} d\vec{r}_s K^s_{Corr_{1,2}}(\omega, \vec{r}_s)\frac{\partial c}{c} \tag{3.19}$$

$$\partial\varphi_{Conv_{1,2}} = \int_{\vec{r}_s} d\vec{r}_s K^s_{Conv_{1,2}}(\omega, \vec{r}_s)\frac{\partial c}{c} \tag{3.20}$$

where $\partial\ \varphi$ is the phase delay associated to the spatial integration over the position of all of the sources and the kernel expresses the sensitivity to local phase velocity perturbations. We now use the interference pattern between two wavefields (calculated with correlation or convolution) to retrieve data-based sensitivity kernels. The kernels are directly extracted from the product of the empirical Green's functions.

In the following, we limit our study of the sensitivity kernels to phase variations between physical receivers in 1 and 2 associated to each physical source in s. Playing with phase only is a way to cancel issues associated to mechanical coupling of geophones and active sources to the ground. It emphasizes the role played by local velocity variations on travel times which is the main goal in tomography inversion. On the other hand, it prevents investigation on local attenuation or damping which we may consider as a second order effect at low frequencies (below 10 Hz). In consequence, we apply spectral whitening on the received data which is equivalent to say that the time-domain correlation and convolution functions for a source in s are normalized

by the energy of the received signals in 1 and 2. Normalized cross-correlations are equal to the coherence function (Jones (2000)).

Acoustic or elastic wave interferometry provides a measure of the wavefield between two receivers by applying cross-correlation, deconvolution (e.g, Wapenaar et al. (2008)), or even convolution (e.g, Roux and Fink (2003); Slob et al. (2007)) to wavefield recordings at these two points (Duguid et al. (2011)). When applied to seismic recordings, surface wave interferometry takes advantage of the correlation process to recover travel time information from uncorrelated noise sources (Sabra et al. (2005); Campillo and Roux (2014)). Indeed, because of phase cancelation in the correlation process, the origin time of the noise sources is not required and seismic noise can be used for surface wave tomography. On the contrary, surface wave interferometry based on convolution demands synchronized, controlled sources with an accurate absolute time.

If we work with active, synchronized sources, we can also consider convolution as the principal operation to derive the sensitivity Kernel. The question is: when should we use cross-correlations and when should we use convolutions? Roux and Fink (2003) showed that the Green's function between two receivers could be retrieved with convolution as the sum over a set of points sources between the receivers: the Green's function between the first point and the sources convolved with the Green's function between the sources and the second point.

It means that for the receivers located on the outside of the two sources we should use the cross-correlations (the difference of two phases) and for the receivers located between the two points we should use the convolutions (the sum of two phases). Figure 3.18 presents a selection of receivers for which we can use the cross-correlations (in green) and for which we can use the convolutions (in orange) to retrieve the Green's function between two sources (red stars).

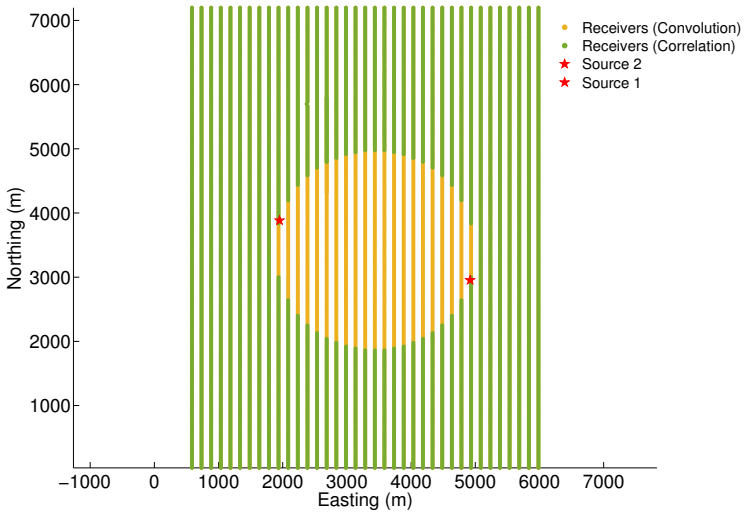

Figure 3.18: Geometry acquisition for data based sensitivity kernels for two sources (distance = 3100 m) calculated with correlation (receivers in green) and convolution (receivers in orange).

3.4.1 Convolution: a mathematical approach

In this project, we benefit from a large set of active sources and receivers to explore both the convolution and the correlation approaches in surface wave interferometry. We now remind the theoretical approach that leads to the Green's function retrieval from controlled sources with both convolution and correlation schemes. In both cases, we follow a similar reasoning as in Roux et al. (2005) for cross-correlations. For sake of simplicity, we limit the theoretical developments (shown in the Appendix) to the 3D acoustic case for which the analytic expression of the Green's function is well known. The generalization to surface waves in a 2D space is straightforward.

Let's consider a free space with attenuation. Volume attenuation is added in the medium by including an imaginary component to the wave speed $c = c_0 + ic_i$, with $c_i << c_0$. We now consider a geometry with two receivers 1 (in $\vec{r_1}$) and 2 (in $\vec{r_2}$) and a source s in $\vec{s}$ (Figure 3.19a).

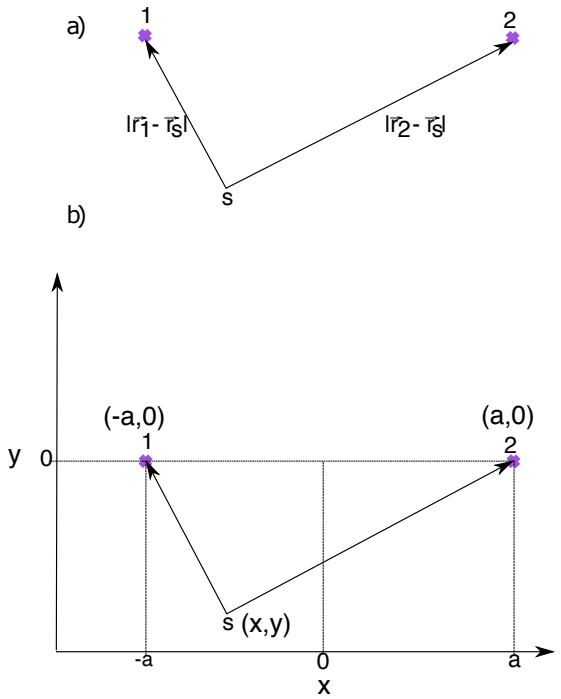

Figure 3.19: a) Two receivers 1 and 2 and a source s. b) Representation in the xy plane of the receivers 1 and 2 that are at (a,0) and (-a,0) and the source s in (x,y).

The Green's functions in a 3D homogenous medium with attenuation between the source s (in $\vec{r_s}$) and the points: 1 (in $\vec{r_1}$) and 2 (in $\vec{r_2}$) are defined in the following way:

$$G_{s,1}(\omega) = \frac{1}{4\pi}\frac{1}{|\vec{r_s} - \vec{r_1}|}\exp\left(\frac{i\omega}{c_0}|\vec{r_s} - \vec{r_1}|\right)\exp\left(\frac{-\omega c_i}{c_0^2}|\vec{r_s} - \vec{r_1}|\right) \tag{3.21}$$

$$G_{s,2}(\omega) = \frac{1}{4\pi}\frac{1}{|\vec{r_s} - \vec{r_2}|}\exp\left(\frac{i\omega}{c_0}|\vec{r_s} - \vec{r_2}|\right)\exp\left(\frac{-\omega c_i}{c_0^2}|\vec{r_s} - \vec{r_2}|\right) \tag{3.22}$$

The Green's function in a 3D homogenous medium with attenuation between point 1 (in r1) and 2 (in r2) is defined in the following way:

$$G_{1,2}(\omega) = \frac{1}{4\pi}\frac{1}{|\vec{r_1} - \vec{r_2}|}\exp\left(\frac{i\omega}{c_0}|\vec{r_1} - \vec{r_2}|\right)\exp\left(\frac{-\omega c_i}{c_0^2}|\vec{r_1} - \vec{r_2}|\right) \tag{3.23}$$

In the time domain the Green's function between the point 1 and 2 is:

$$G_{1,2}(t) = \frac{1}{2\pi}\int_{-\infty}^{\infty} G_{1,2}(\omega)\exp(i\omega t)d\omega \tag{3.24}$$

Which can be written as:

$$G_{1,2}(t) = \frac{1}{8\pi}\int_{-\infty}^{\infty} d\omega\frac{1}{|\vec{r_1} - \vec{r_2}|}\exp\left(i\omega\left(t + \frac{|\vec{r_1} - \vec{r_2}|}{c_0}\right)\right)\exp\left(\frac{-\omega c_i}{c_0^2}|\vec{r_1} - \vec{r_2}|\right) \tag{3.25}$$

We now define a Cartesian coordinate system (the same as presented on the figure 3.9) for the 3D space in which receiver 1 is in (a,0,0), receiver 2 is in (-a,0,0), and the source s is in (x,y,z) (Figure 3.19b). Now, the Green's function between the point 1 and the point 2 yields:

$$G_{1,2}(t) = \frac{1}{8\pi}\int_{-\infty}^{\infty} d\omega\frac{1}{2a}\exp\left(i\omega\left(t + \frac{2a}{c_0}\right)\right)\exp\left(\frac{-\omega c_i}{c_0^2}2a\right) \tag{3.26}$$

We now consider correlation and convolution of two signals recorded at 1 and 2 from a single source s.

Table 3.1: Correlation and Convolution

Correlation	Convolution
$Corr_{1,2}(\omega) = G_{s,1}(\omega)G^*_{s,2}(\omega)$ (3.27)	$Conv_{1,2}(\omega) = G_{s,1}(\omega)G_{s,2}(\omega)$ (3.28)

A mathematical development for both: correlation and convolution of the Green's functions is presented in Appendix A. We present here only the final results of the development:

Table 3.2: Converge towards the Green's function from correlation and convolution

Correlation	Convolution
$\frac{d}{dt}\langle Corr_{1,2}(t)\rangle \approx \frac{c_0^3}{4\pi c_i}\frac{1}{\omega}\left(G_{1,2}(t) - G_{2,1}(t)\right)$ (3.29)	$\frac{d}{dt}\langle Conv_{1,2}(t)\rangle \approx -\frac{c_0^2}{2\pi(c_0 + ic_i)}2aG_{1,2}(t)$ (3.30)

The time derivate of the correlation function converges towards a causal and anticausal (time-reversed) estimate of the Green's function between the two points, as shown in Roux et al. (2005).

The time derivate of the convolutions function directly converges towards a causal estimate of the Green's functon between the two points. However, the attenuation in the medium will influence the estimate of the Green's function from correlations and convolutions. The complex coefficient $\frac{c_0^2}{2\pi(c_0+ic_i)}$ introduces a phase shift in the retrieved Green's function with convolutions if the attenuation is present in the medium. This might cause a phase shift of causal estimate of the Green's functions obtained from convolutions. Also, it might open a possibility of an alternative attenuation measurements based on correlations and convolutions.

In our processing, we use a normalized convolution. The normalized convolution $Conv_{1,2}(t)$ between two traces $r_{s,1}$ and $r_{s,2}$ recorded for the same source s at two receivers 1 and 2 is divided by the square root of the traces energies $E_{s,1}$ and $E_{s,2}$. The convolution of two signals in 1 and 2 reads:

$$Conv_{1,2}(t) = \frac{r_{s,1} * r_{s,2}}{\sqrt{E_{s,1}E_{s,2}}} \tag{3.31}$$

Figure 3.20 shows the casual correlation functions in a) and the convolution functions in b) with their stacks in the frequency band (2-8) Hz for the geometry presented on the Figure 3.18. Note, that only the cross-correlation functions of the receivers located within the Fresnel zone are presented. For the convolution functions, all the receivers located between two receivers are presented.

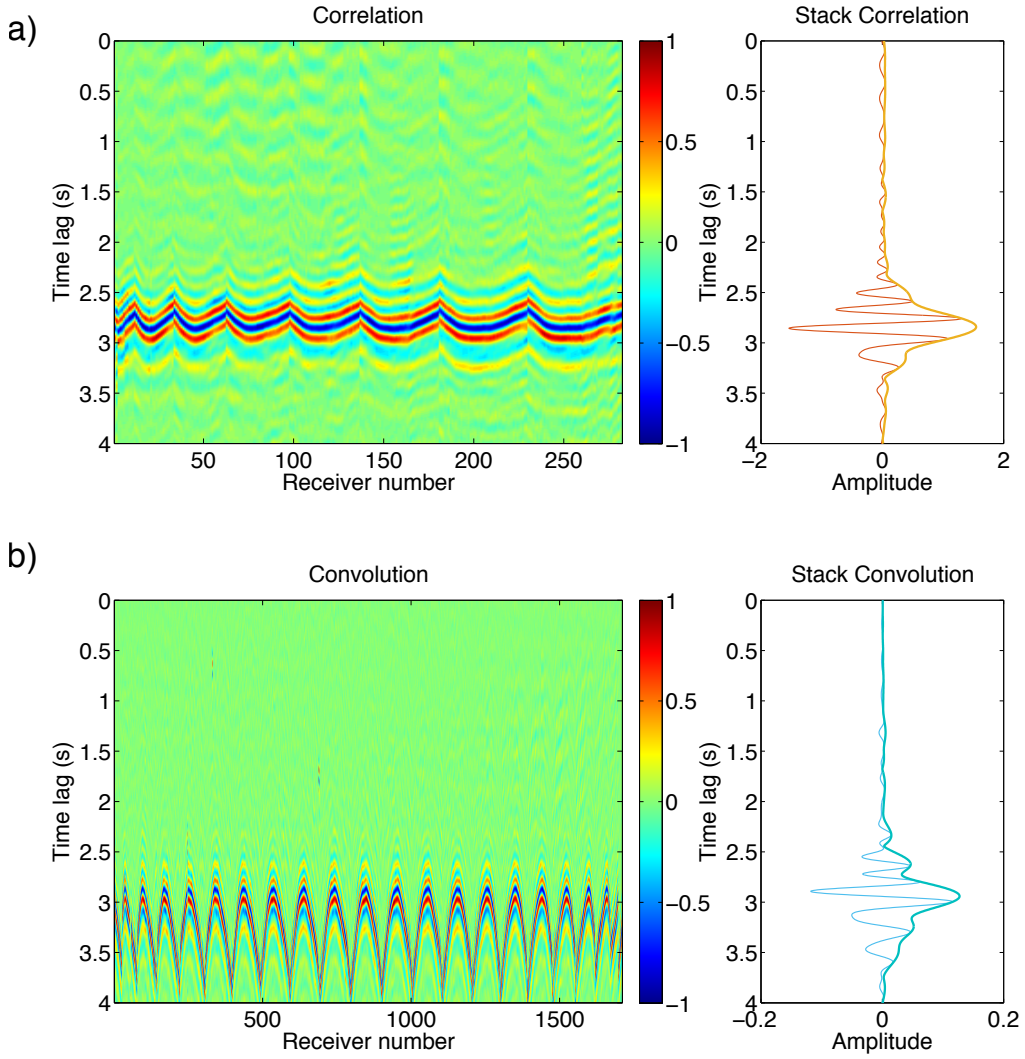

Figure 3.20: Correlation and Convolution function. a) Left: Normalized correlation (coherence) calculated for receivers within the stationary phase zone defined with the sensitivity kernels for correlations; Right: Stack of all the correlations. b) Left: Normalized convolution (coherence) calculated for all the receivers within the circle presented n the Figure 3.18); Right: Stack of all the convolutions.

3.4.2 Empirical kernels in the time domain

Now, we look into the construction of the empirically determined phase traveltime sensitivity kernels for surface waves. As stated before, sensitivity kernels often require a significant amount of calculations. However, some empirical constructions of 2D surface wave phase sensitivity kernels were demonstrated. Lin and Ritzwoller (2010) follow a basic idea of the adjoint method to construct the sensitivity kernels. In particular, they mimic the adjoint calculations to retrieve information about wave propagation due to an impulsive force at one station location by using the

virtual source property.

Here, we proposed another approach to derive empirical kernels. Thanks to the carpet shooting we can calculate sensitivity kernels for surface waves at any two points in the acquisition, in particular the inner kernels (extracted with convolutions) and the outer kernels (extracted with correlations). We define the phase data based sensitivity kernels as a spatial representation of a coherence at time t_i prior to the spatial averaging performed on the set of sources s.

$$K^s_{Conv_{1,2}}(t_i, \vec{r_s}) = Conv^s_{1,2}(t_i, \vec{r_s}) \tag{3.32}$$

$$K^s_{Corr_{1,2}}(t_i, \vec{r_s}) = Corr^s_{1,2}(t_i, \vec{r_s}) \tag{3.33}$$

On Figure 3.21 and Figure 3.22 we see data-based: inner sensitivity kernels extracted from convolutions and outer sensitivity kernels extracted from positive lag of cross-correlations for two source points in the frequency band (2-8) Hz.

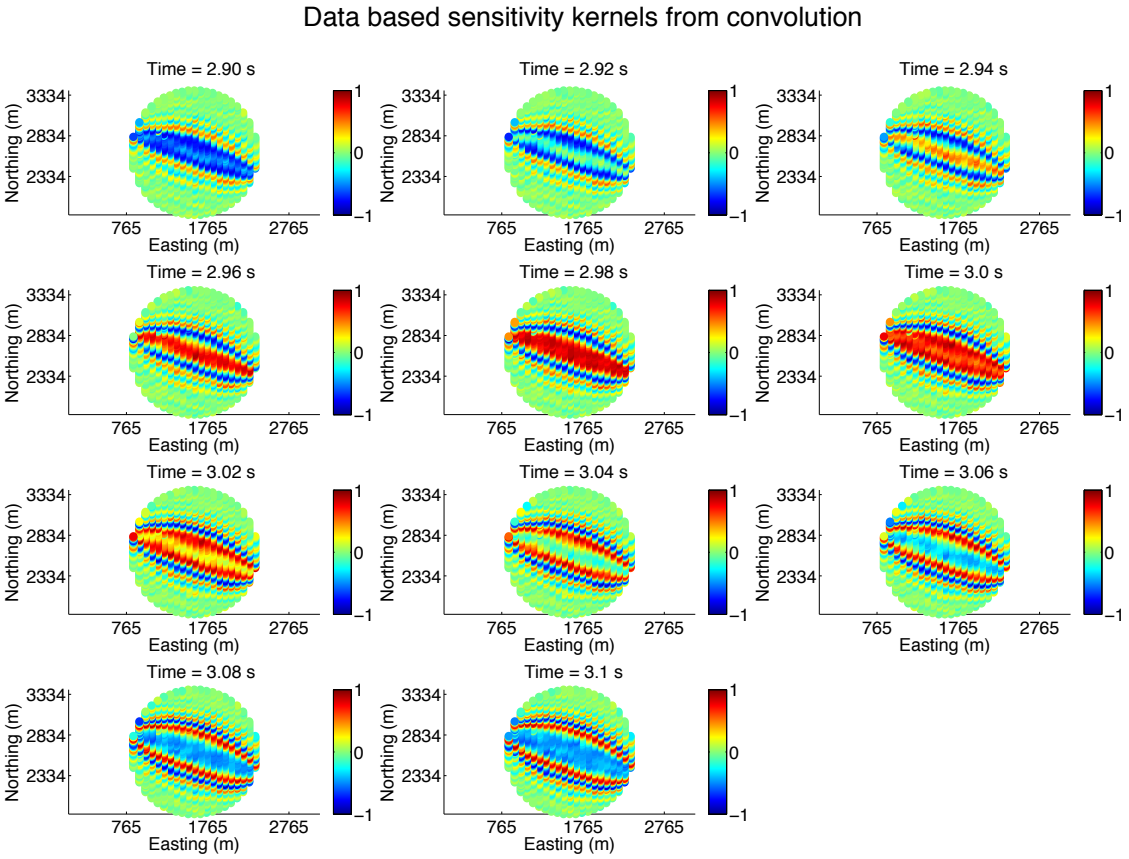

Figure 3.21: Data-based inner sensitivity kernels extracted from convolutions at different times t_i for the frequency band (2-8) Hz.

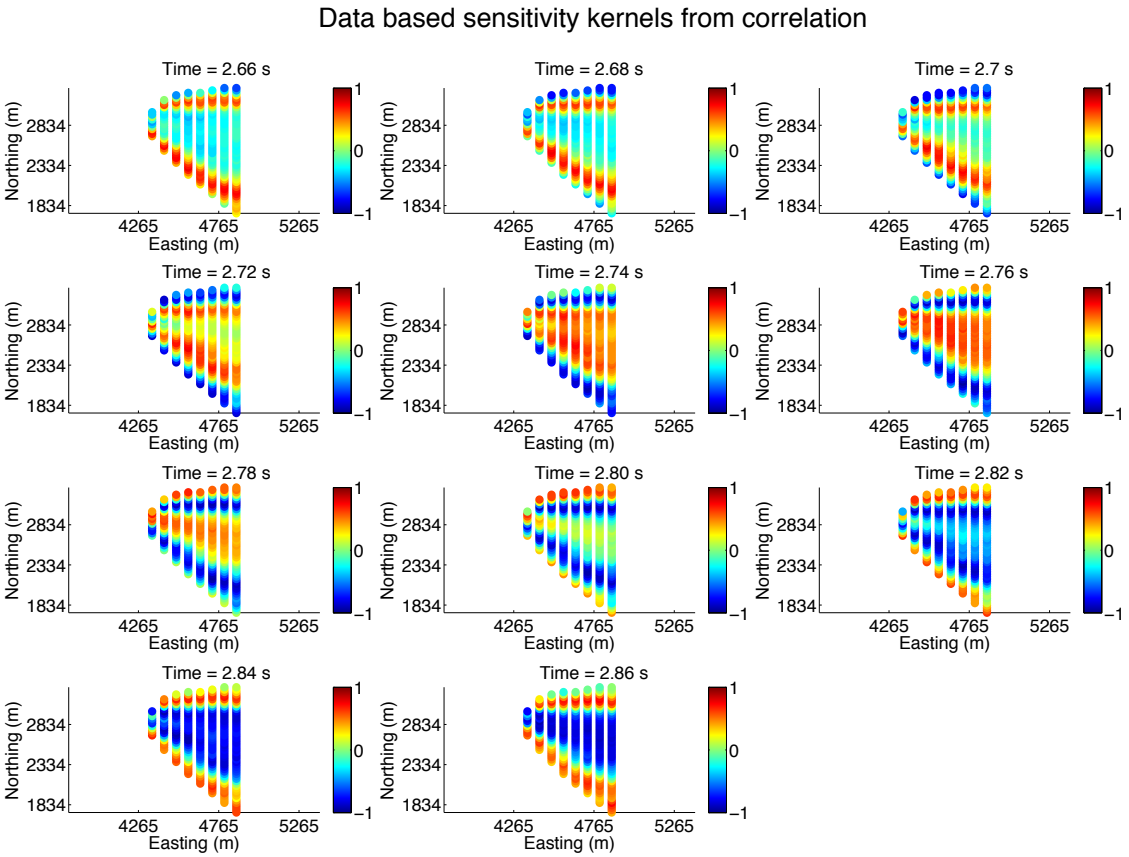

Figure 3.22: Data-based outer sensitivity kernels extracted from correlations at different times t_i for the frequency band (2-8) Hz.

Analogically to cross-correlations (equation 3.13), we can define a theoretical sensitivity Kernel calculated with convolutions. The convolution of the two modeled Green's functions (as defined in equations 3.9, 3.10) gives:

$$Conv_{1,2}(\omega) = G_1^0(\vec{r}_S, \vec{r}_1, \omega) G_2^0(\vec{r}_S, \vec{r}_1, \omega) = \exp\left(i\omega\left(t_1 + t_2\right)\right) \tag{3.34}$$

We define a kernel function that is based on the convolution:

$$K_{Conv_{12}}(\omega) = \exp\left(i\omega\left(\frac{d}{c} - (t_1 + t_2)\right)\right) \tag{3.35}$$

where c – is a mean phase velocity of Rayleigh waves, t_1 propagation time from source s to receiver 1, t_2 propagation time from source s to receiver 2, d - distance between the two point sources, and $\omega = 2\pi f$ the central angular frequency.

After an integration over a frequency band:

$$H_{Conv_{1,2}}(\omega) = \int_{\omega_1}^{\omega_2} K_{Conv_{12}}(\omega) = \exp\left(i\omega_0\left(\frac{d}{c} - (t_2 + t_1\right)\right) \operatorname{sinc}\left(\frac{\Delta\omega}{2}\left(\frac{d}{c} - (t_2 + t_1)\right)\right) \tag{3.36}$$

We now represent the outer and inner sensitivity Kernels together. The source density is 5 times bigger than the receiver density, so we decided to work in virtual sources domain – it means that we represent kernels calculated for the carpet of sources. We can benefit from this dense acquisition to track more precisely the phase traveltime. On Figure 3.23 we compare the real part of theoretical sensitivity kernels (calculated in the frequency domain: equations: 3.13 and 3.35) to the empirical sensitivity kernels (calculated in the time domain). The theoretical kernels were calculated with a mean phase velocity of 1100 m/s, for the frequency (2-4) Hz a) and (4-6) Hz. Data-based kernels are retrieved at the maximum time of a stack which is: 2.71 s (correlation) and 2.71 s (convolution) for (2-4) Hz and at the time 2.47 s (correlation) and 2.49 s (convolution) for (4-6) Hz. Note the change in the aperture for Kernels with frequency (the higher the frequency the smaller the aperture).

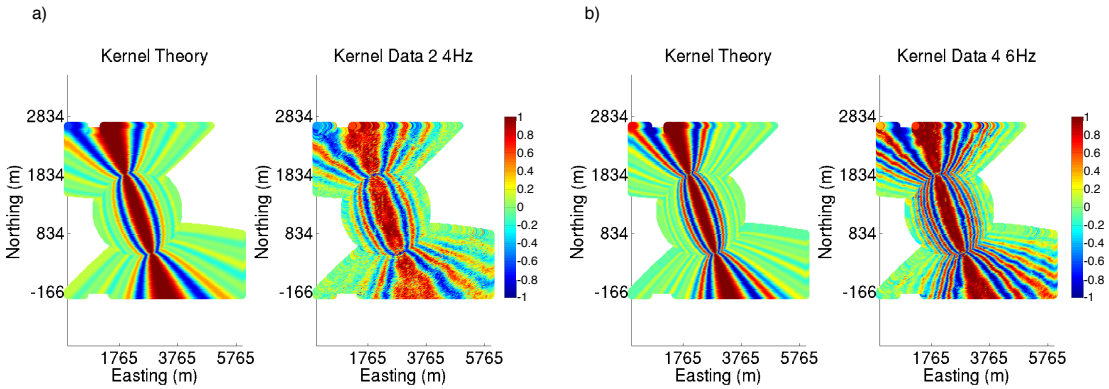

Figure 3.23: Data-based sensitivity kernels from correlations and convolutions for two receivers (distance 2900 m) a) left: Theoretical kernel for the frequency (2-4) Hz obtained with the velocity 1100 m/s; right: data-based sensitivity kernel from correlation and convolutions obtained for the time 2.71 s (correlation) and 2.71 s (convolution). b) left: Theoretical kernel for the frequency (4-6) Hz obtained with the velocity 1100 m/s; right: data-based sensitivity kernel from correlation and convolutions obtained for the time 2.47 s (correlation) and 2.49 s (convolution).

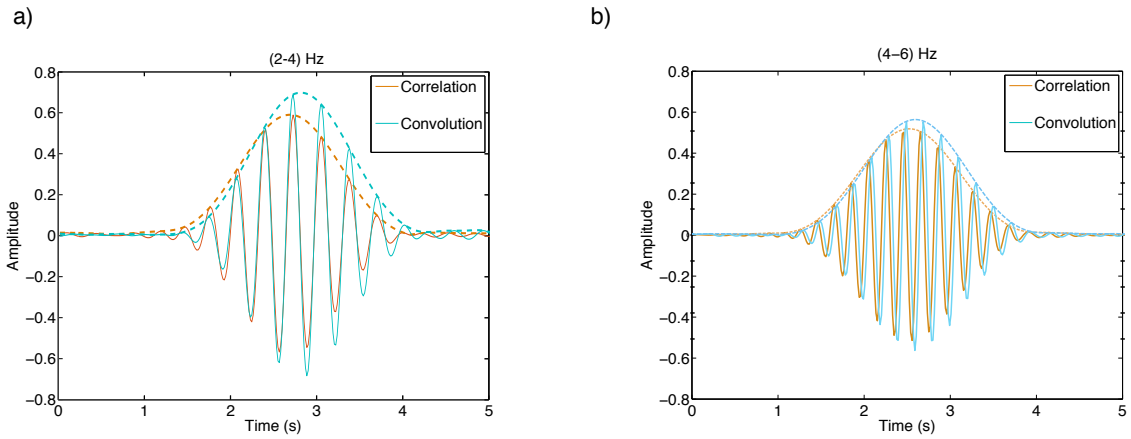

Figure 3.24: Comparison between stacks of the correlation and convolution functions within the stationary phase zone (first phase oscillation for frequency: a) (2-4) Hz and b) (4-6) Hz.

In Figure 3.24 we show a virtual trace obtained with correlations (positive lag) and convolutions. All the cross-correlation functions and convolution functions within the stationary phase zone (the first Fresnel zone) were stacked. We observe that these virtual traces for the two receivers are not exactly the same. This difference can be caused by a few reasons. First, there might be a phase shift of convolutions that depends on the attenuation in the medium (Table 3.2). This phase shift can be used to estimate the attenuation in the medium. Also, we use different spatial information to retrieve the Green's function with correlations and convolutions. Moreover, correlations consist in a subtraction of phases, while convolution consists in a summation. It means that information extracted from correlations should be more independent on the statics corrections.

3.4.3 Single frequency empirical kernels

In the previous section, we considered theoretical kernels in the frequency domain and the empirical kernels in the time domain. However, the data-based kernel functions can be retrieved in the frequency domain. The kernels are directly extracted from the product of the empirical Green's functions. They correspond to a spatial representation of the correlation and convolution process described above prior to the spatial averaging performed on the set of sources s. In the frequency domain (for a single frequency f), they are defined as:

$$K^s_{Conv_{1,2}}(t_i, \vec{r_s}) = G_{s,1}(\omega) \cdot G_{s,2}(\omega) \tag{3.37}$$

$$K^s_{Corr_{1,2}}(t_i, \vec{r_s}) = G_{s,1}(\omega) \cdot G^*_{s,2}(\omega) \tag{3.38}$$

These Kernels consist of correlations/convolutions of two wavefields multiplied by a constant $\exp\left(i\omega\frac{d}{c}\right)$. As in the literature, the sensitivity kernels between points in 1 and 2 are phase delayed

by the travel time $t_{1,2}$ between the two points. The travel-time $t_{1,2}$is derived in an empirical way and corresponds to the maximum of the stacked convolution or correlation functions

We represent kernels that are extracted from correlations and convolutions for single frequencies (only the real part of the kernel functions is represented). On Figure 3.25 and Figure 3.26 we represent inner kernels and outer (positive lag) kernels for two receivers within distance of 930 m. Note that we observe significantly more phase oscillations for the inner kernel than for the outer kernel. For the simplicity of display, we represent only the first five phase oscillations of the inner sensitivity kernel.

As the frequency increases, the wavelength of surface waves decreases. It means that surface wave kernels become more sensitive to spatial heterogeneities, what we observe on Figure 3.25d,and Figure 3.26c, and Figure 3.26d. Also, for higher frequencies we observe the beating phenomena. The higher surface waves mode interferes with the fundamental mode, which appears as: a circular disorder for outer kernels (Figure 3.26c and Figure 3.26d) and a deformation of an elliptical shape for inner kernels (Figure 3.25d). Note, that the outer kernels provide spatially coherent information for higher frequencies than the inner kernels. It is due to the phase subtraction in correlations that is a more robust and stable operation then the phase summation in convolutions.

These sensitivity kernels will be subsequently used to produce phase-velocity dispersion curves between two points and to separate the higher mode from the fundamental mode for surface waves (Chapter 4). Potential application to surface wave tomography and surface wave cancellation can be also envisaged.

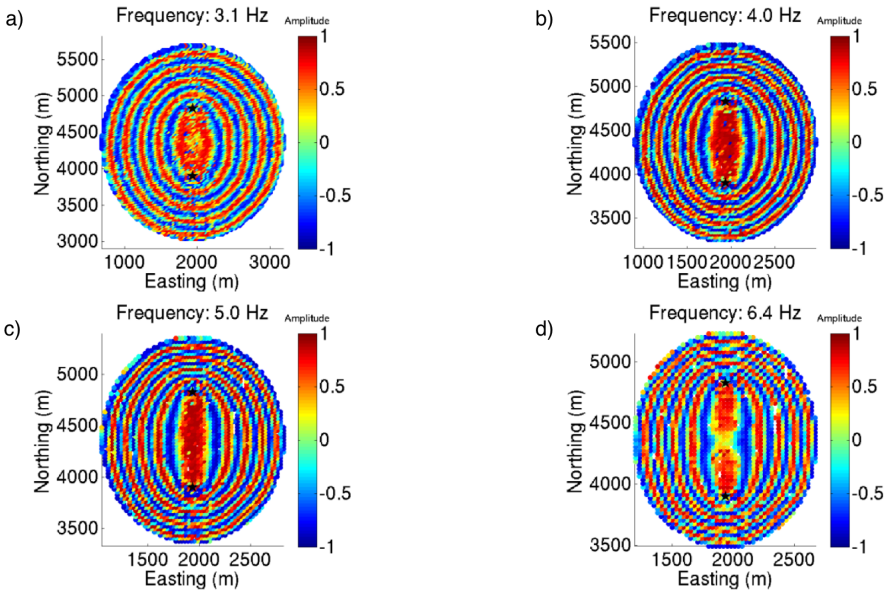

Figure 3.25: Data-based inner sensitivity kernels obtained from convolution for frequency a) 3.1 Hz: b) 4 Hz; c) 5 Hz; d) 6.4 Hz. The distance between two receivers is 930 m. Note, that for the simplicity of display, we represent only the first five phase oscillations of the sensitivity kernel.

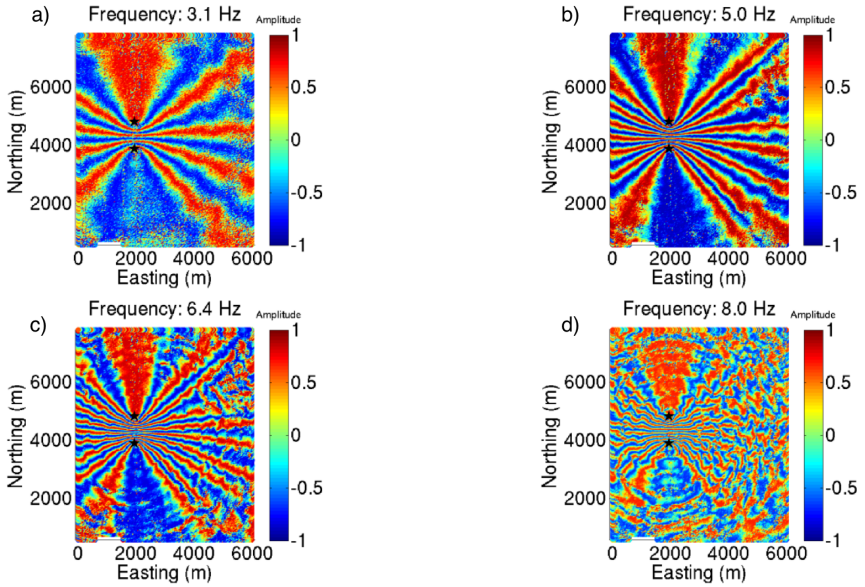

Figure 3.26: Data-based outer sensitivity kernels obtained from correlation for frequency a) 3.1 Hz: b) 5 Hz; c) 6.4 Hz; d) 8 Hz. The distance between two receivers is 930 m.

3.5 Conclusions

Seismic configuration with active, controlled sources gives more possibilities when it comes to interferometry. The use of controlled sources makes it possible to recover the surface wave Green's function between two points using either correlation or convolution. We investigated the convolutional and correlational approaches using land active-seismic data from exploration geophysics. Invoking spatial reciprocity between sources and receivers, correlation and convolution functions can thus be constructed between either pairs of receivers or pairs of sources. Different approaches for stationary phase approximation were presented. From angle, hyperbole approximations through the directivity pattern calculations, we ended up by defining sensitivity kernels for surface waves. These kernels can be calculated with correlations or convolutions. This criterion seems to be the optimal one; it is based on the phase oscillations. Moreover, it requires only one a priori, which is a mean phase velocity.

Benefiting from the dense acquisition, we extracted phase data based sensitivity kernels from correlation and convolution measurements of the seismic data. In the next chapter, we present one of the possible applications of the kernels. They can be used to produce phase-velocity dispersion relations between two points and to separate the higher mode from the fundamental mode for surface waves.

Chapter 4

Dispersion analysis with Hyperbolic and Ellipsoid transforms

In this chapter we present applications of phase sensitivity kernels from correlations and convolutions. First, we use them to produce phase-velocity dispersion relations between two points. Then, we invert them to obtain S-wave and P-wave velocity profiles. In addition, we use the dispersion curves to separate higher modes of Rayleigh waves.

Dispersion of surface waves is mostly due to a vertically stratified medium. If the medium is homogenous, Rayleigh wave velocities are non-dispersive. In a layered space we may observe dispersion and higher modes of surface waves. If the velocity of the upper layer is low enough to cause a complete reflection of both P- and SV-waves then we observe higher branches of Rayleigh waves (Heaton (2005)). These overtones can provide important information on shallow structure and on uniqueness of inverted models (van Heijst and Woodhouse (1997)). Still, it might be difficult to use the higher modes due to their interference, their simultaneous arrivals, and their overlap in the frequency domain.

Different wavelengths sample different layers of the subsurface, which means that the shape of dispersion curves is related to geologic profiles (Pei (2007)). Surface waves dispersion curves can be inverted to obtain S- wave velocity model of the near surface and in some cases (e.g., in the presence of surface-wave overtones) P-wave velocity model. It can improve P-wave tomography and determination of P-wave statics (Duret et al. (2016)).

4.1 Hyperbolic and ellipsoid transforms: Projection

We now use the data-based sensitivity kernels in an inversion of medium properties to produce phase-velocity dispersion relations between two measurement points. We may project phase sensitivity kernels into the frequency-phase-velocity space. In order to do so, we define a projection that is applied to the phase sensitivity kernels. It will allow finding an approximate linear relationship between kernels and phase velocity values. For each frequency we define the define

the relation between the sensitivity kernel and a dispersion relation as:

$$\vec{K}(\vec{r}_s) = \bar{\bar{A}}(\vec{r}_s; c)\vec{D}(c) \tag{4.1}$$

where: $\bar{\bar{A}}$-transformation matrix, $\vec{K}(\vec{r_s})$-is the vector containing kernel values for a given frequency (observed data), $\vec{D}(c)$- dispersion relation (modeled data).

We seek the dispersion relation $\vec{D}$:

$$\bar{\bar{A}}^T\vec{K} = \bar{\bar{A}}^T\bar{\bar{A}}\vec{D} \tag{4.2}$$

If we assume that the transformation matrix is orthogonal,

$$\bar{\bar{A}}^T\bar{\bar{A}} = I \tag{4.3}$$

where I is the identity matrix, then the equation 4.2 yields:

$$\bar{\bar{A}}^T\vec{K} = \vec{D} \tag{4.4}$$

The matrix is a transformation matrix, that allows to connect the spatial domain with the phase velocity domain (c). We introduce two transformation matrices for correlation (hyperbolic transformation) and convolution (ellipsoid transformation).

4.1.1 Hyperbolic transform

First, we consider the sensitivity kernels from correlations: $\vec{K}_{Corr}$ extracted between two points in $\vec{r_1}$, $\vec{r_2}$. Kernel functions depend on an angular frequency ω and the position of source s $\vec{r_s}$. Hyperbolic transformation is based on the difference of phases:

$$\bar{\bar{A}}(c, \vec{r}; \omega) = \exp\left(\frac{i\omega}{c}\left(|\vec{r}_1 - \vec{r}_s| - |\vec{r}_2 - \vec{r}_s|\right)\right) \tag{4.5}$$

We calculate the dispersion relation using the projection:

$$D^{1,2}_{Corr}(\omega, c) = \sum_s \left(\exp\left(\frac{i\omega}{c_0}(|\vec{r}_1 - \vec{r}_s| - |\vec{r}_2 - \vec{r}_s|)\right) K^{1,2}_{Corr}(\vec{r}_s; \omega)\right) \tag{4.6}$$

Note that we directly use information from correlation (and convolution), there is no multiplication by coefficient $\exp(i\omega\frac{d}{c_0})$. This transform projects the sensitivity kernels into frequency-phase velocity domain. Note that in equation 4.6 we calculate the transform using scalar representation and summing over all the source position. We might write the same equation using matrix representation as presented in the equation 4.4.

Figure 4.1 shows a dispersion relation calculated for two sources within a distance of 930 m (the same configuration as presented in Chapter 3, Figure 3.25, 3.26). We can also apply another transform to obtain a frequency-wavenumber (FK) diagram between the two points:

$$D^{1,2}_{Corr}(\omega, k) = \sum_s \left(\exp\left(ik(|\vec{r}_1 - \vec{r}_s| - |\vec{r}_2 - \vec{r}_s|)\right) K^{1,2}_{Corr}(\vec{r}_s; \omega)\right) \tag{4.7}$$

In order to improve the quality of results and to minimize the effects of the secondary maximums, we may integrate the equation 4.7 over a small wavenumber band Δk (0.004 1/m).

$$D^{1,2}_{Corr}(\omega,k) = \frac{\Delta k}{2}\sum_{s}(\exp\left(ik(|\vec{r}_1-\vec{r}_s|-|\vec{r}_2-\vec{r}_s|)\right) \\ \operatorname{sinc}\left(ik(|\vec{r}_1-\vec{r}_s|-|\vec{r}_2-\vec{r}_s|)\right) K^{1,2}_{Corr}(\vec{r}_s;\omega)) \tag{4.8}$$

where: $k_1 = k_0 - \frac{\Delta k}{2}$, $k_2 = k_0 + \frac{\Delta k}{2}$.

We normalize the hyperbolic transform in equation 4.8 by $\frac{\Delta k}{2}$. We can smooth the secondary maxima even more, by integrating the function $CCorr^{1,2}(\omega,k)$ over a small frequency band: $\Delta\omega$ centered at ω_0 (here: $\Delta\omega$ = 0.27 Hz).

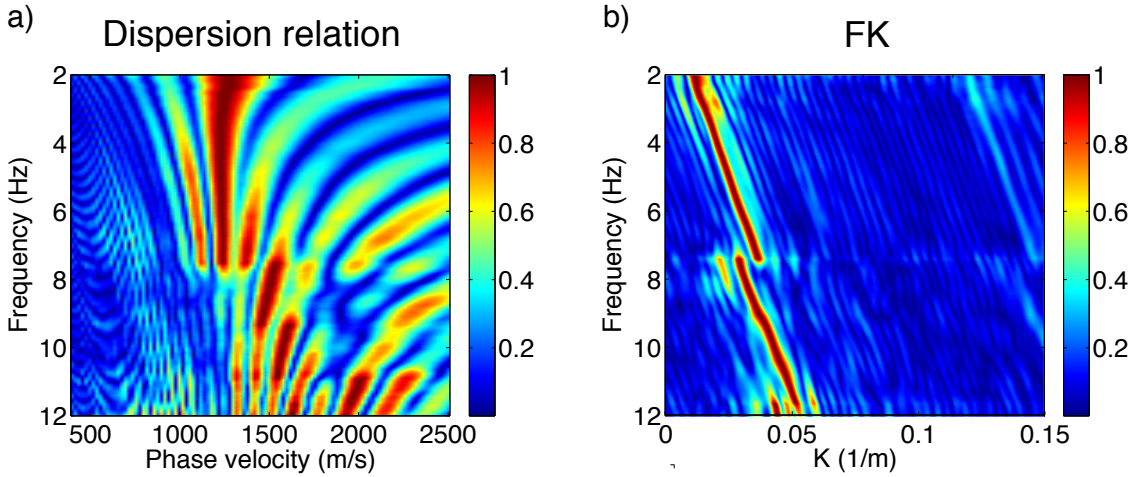

Figure 4.1: Projection of the sensitivity kernel from correlations into dispersion relations using the hyperbolic transform. a) Dispersion relation obtained with the projection. b) Dispersion relation (FK) obtained with the projection and integration over $\Delta\omega$ and Δk.

The integration over $\Delta\omega$ and Δk minimizes the oscillations observed on the Figure 4.1a. The amplitudes of dispersion relations are normalized by their maximums for each frequency. We use the same normalization for all dispersion relations in this chapter. Note the discontinuity at 8 Hz that we spotted in Chapter 3. It corresponds to a superior mode of surface waves that sets off at this frequency. The integration over $\Delta\omega$ and Δk improves the results, we observe less secondary oscillations, in comparison to Figure 4.1a. However, it decreases the resolution of the FK plot. This plot (Figure 4.1b) is of a much higher quality that the FK plot obtained with a traditional method (Chapter 3, Figure 3.16, 3.17). These figures represent an average phase velocity between the two points. We observe an aliasing for higher wave-numbers, although it does not directly affect the dispersion relation. Note, that we are able to obtain these dispersion relations between any two points benefitting from the dense acquisition. We might calculate them

for each pair of receivers or sources. Now, we can use the same transform to relocate the sources in the spatial domain:

$$D^{1,2}_{Corr}(\omega; r_{ij}, r_{kl}) = \sum_s \left(\exp\left(\frac{i\omega}{c_0} (|\vec{r}_{ij} - \vec{r}_s| - |\vec{r}_{kl} - \vec{r}_s|) \right) K_{Corr}(\vec{r}_s; \omega) \right) \tag{4.9}$$

We calculate the spatial transform $D^{1,2}_{Corr}(\omega; r_{ij}, r_{kl})$ for each two points in $\vec{r}_{ij}$ and in $\vec{r}_{kl}$. To calculate D_{Corr} we fix an average phase velocity c for a given frequency. Normally, the argument of maximum of $CCor$ should correspond to the theoretical position of the first source and the second source:

$$\text{Indmax}\left(D^{ijkl}_{Corr}(\omega, r_{ij}, r_{kl}) \right) \Rightarrow r_{1max}, r_{2max} \tag{4.10}$$

Re-localization of source 1 using the hyperbolic transform is presented on the Figure 4.2a. We use a regular grid with a step of 10 m to calculate D^{ijkl}_{Corr}. The position of the source 1 found with this method is shifted by 10 m comparing to the theoretical position (in black star). The position of the source 2 is shifted by 28 m comparing to the theoretical position (we do not represent it here). However, we see that the theoretical position of the source is located within the maximum of the output map. The resolution of the maximum spot is limited by the wavelength due to diffraction laws. We can apply this method to higher frequencies to improve the resolution of the output, but the processing will become more sensitive to the spatial heterogeneities. The shift between the theoretical position and the found position might be due to the use of a homogenous velocity model.

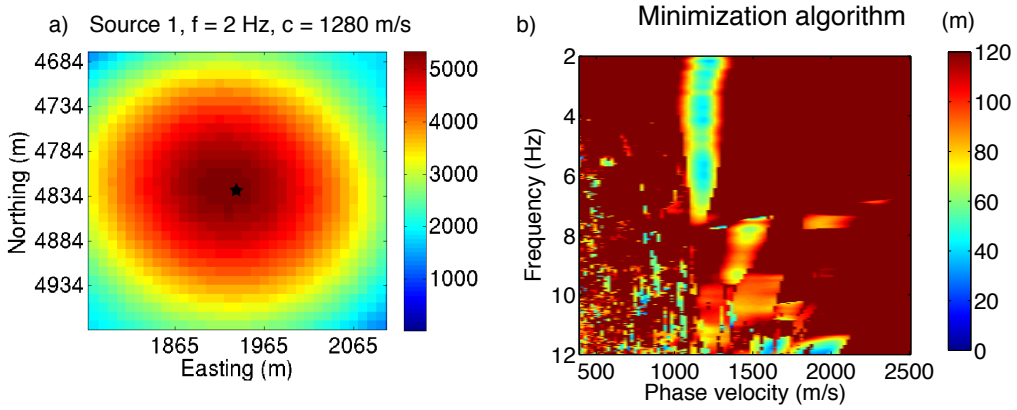

Figure 4.2: a) Re-localization of a receiver using the hyperbolic transform, b)Dispersion relation obtained with the minimization algorithm.

We can use the misfit of re-location to calculate a dispersion relation (Figure 4.2b). In order to do so, we introduce a minimization algorithm (as described in 2.3.3). This function looks for positions that minimize the value of $-CCorr^{ijkl}$. It uses the simplex search method of Lagarias et al (1998) to find the minimum. This minimization algorithm is more efficient than the function based on the grid search. It means, that we might add one more dimension (a mean phase velocity)

to obtain a dispersion relation. This time, we represent a spatial misfit between the theoretical positions of the sources and the positions derived from the minimization algorithm (Figure 4.2b). We see that this dispersion relation has less secondary maximums then the dispersion relation in Figure 4.1a. We conclude that by adding more variables to the transformation and by using the minimization algorithm, we constrain better the dispersion relation.

4.1.2 Ellipsoid transform

We follow the same path of calculations for convolutions, although this time we define an ellipsoid transform:

$$D^{1,2}_{Conv}(\omega, c_0) = \sum_s \left(\exp\left(\frac{i\omega}{c_0} (|\vec{r}_1 - \vec{r}_s| + |\vec{r}_2 - \vec{r}_s|) \right) K_{Conv}(\vec{r}_s; \omega) \right) \tag{4.11}$$

Dispersion relation obtained with inner sensitivity kernels and the ellipsoid transform is shown at Figure 4.3a. We observe less oscillation and a higher resolution then the dispersion relation from correlations. However, this dispersion relation becomes more ambiguous in higher frequencies. We also calculate a dispersion relation in the frequency-wavenumber (FK) domain:

$$D^{1,2}_{Conv}(\omega, k) = \sum_s \left(\exp\left(ik(|\vec{r}_1 - \vec{r}_s| + |\vec{r}_2 - \vec{r}_s|) \right) K_{Conv}(\vec{r}_s; \omega) \right) \tag{4.12}$$

Analogically to correlations we can integrate the previous equation over a wave-number band Δk (0.0004 1/m) and $\Delta\omega$ (0.031 Hz) to smooth the dispersion relations (Figure 4.3b).

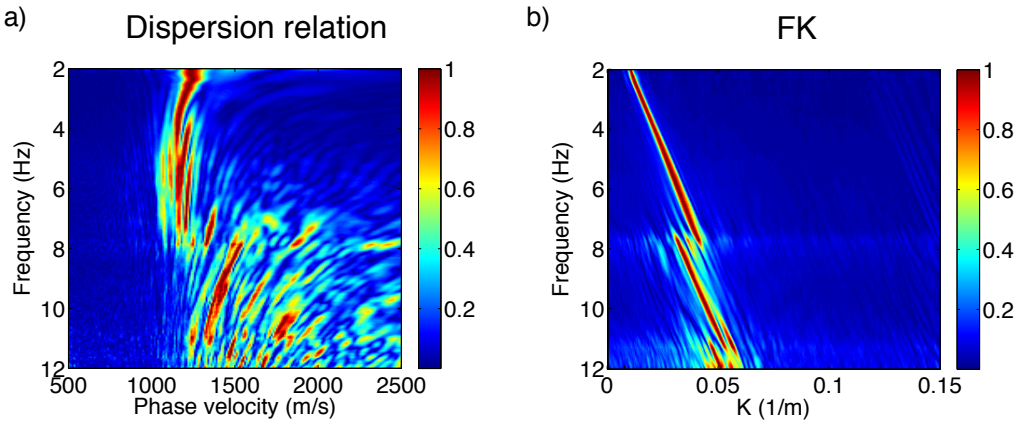

Figure 4.3: Projection of the sensitivity kernel from convolutions into dispersion relations using the ellipsoid transform. a) Dispersion relation obtained with the projection, b) Dispersion relation (FK) obtained with the projection and integration over $\Delta\omega$ and Δk.

We observe much more phase oscillations for sensitivity kernels from convolutions than from correlations (see: Chapter 3). Moreover, Fresnel zones from convolutions become more deformed with offset. Using the first few oscillations of the inner kernels might improve dispersion relations.

We empirically determined that by selecting the first 8 oscillations of the inner sensitivity kernels (Figure 4.4a), we improve the results of projection (Figure 4.4b). Introducing a selective criterion in space lowers the resolution of the dispersion relation, but it reduces its ambiguity.

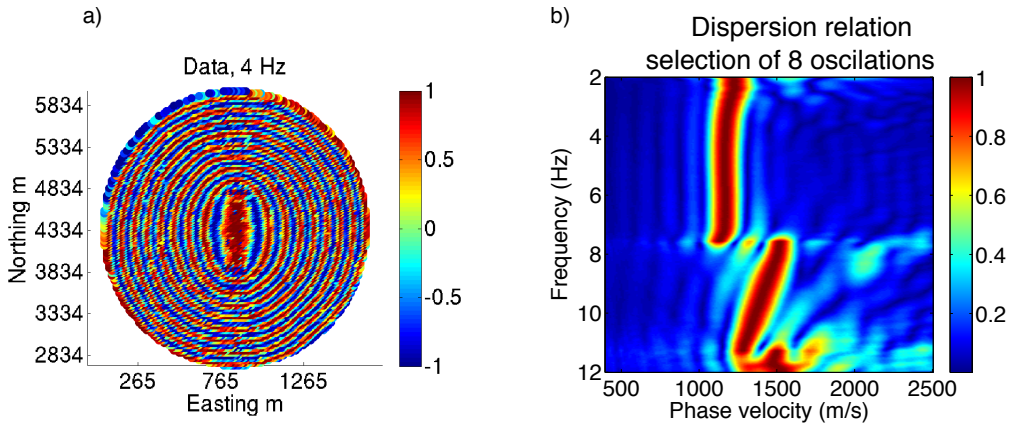

Figure 4.4: a) Selection of sources located within the first 8 phase oscillations. b) Dispersion relation obtained from convolutions using the selection of sources.

Analogically to hyperbolic transform, we tested the relocalization algorithm using the ellipsoid transform. It appeared that shift of the source positions found with convolution was more important than for the correlations and dispersion relation was not clear. These results are not presented here. Also, we tested a spatially selective criterion for correlations, but it did not improve the results. It confirms that correlation and convolution have different properties and they bring complementary information about a mean phase velocity between two points.

4.2 Least squares

4.2.1 Theory

We now go back to the equation:

$$\bar{\bar{A}}^T \vec{K} = \bar{\bar{A}}^T \bar{\bar{A}} \vec{D} \tag{4.13}$$

This time, we do not assume the orthogonality of the matrix A. In order to find the vector $\vec{x}$ we follow the development:

$$(\bar{\bar{A}}^T \bar{\bar{A}})^{-1} \bar{\bar{A}}^T \vec{K} = \vec{D} \tag{4.14}$$

We now introduce the Least Squares estimate that is also called a residual sum of squared errors (Hastie et al. (2001)):

$$RSS = ||(\bar{\bar{A}}^T \bar{\bar{A}})^{-1} \bar{\bar{A}}^T \vec{K} - \vec{D}||_2^2 \tag{4.15}$$

This estimate is defined as a minimum of this equation. It means that by using the least squares approach we find the vector $\vec{x}$ (a dispersion relation) that minimizes the misfit between the model

and the data. It should give more accurate results than the previously used projection. However, the square matrix $\bar{\bar{A}}^T\bar{\bar{A}}$ may be singular. We need to ensure a full rank matrix $\bar{\bar{A}}^T\bar{\bar{A}}$ in order to inverse it. Considering that, we apply a regularization by adding a small positive constant to the diagonals of A^TA:

$$(\bar{\bar{A}}^T\bar{\bar{A}})_\epsilon = (\bar{\bar{A}}^T\bar{\bar{A}}) + \epsilon I \tag{4.16}$$

where ϵ is a constant and I is the identity matrix.

One of the possible solutions is to define ϵ as the norm L2 of the matrix (A^TA) divided by 100: $\frac{||\bar{\bar{A}}^T\bar{\bar{A}}||_2^2}{100}$. Then the minimization problem reduces to the following expression:

$$RSS = ||(\bar{\bar{A}}^T\bar{\bar{A}})^{-1}\bar{\bar{A}}^T\vec{y} - \vec{x}||_2^2 + \lambda||\vec{K}||_2^2 \tag{4.17}$$

where: $\lambda = \frac{1}{100}$.

L2-norm regularization provides a numerical stability, although it does not encourage sparsity of the found model $\vec{x}$ (Schmidt (2005)). A sparse model is a model in which most of the elements are zero. There has been a recent trend to represent a seismic data as a sparse volume in a given domain (e.g.: Guillouet et al. (2016)). Sparse model can be obtained with a L1-norm regularization. Using the L1-norm in equation 20 yields:

$$LASSO = ||(\bar{\bar{A}}^T\bar{\bar{A}})^{-1}\bar{\bar{A}}^T\vec{y} - \vec{x}||_2^2 + \lambda||\vec{K}||_1 \tag{4.18}$$

Regularization with norm L1 cannot be solved algebraically. This led to the introduction of different techniques to determine the optimal parameters (Schmidt (2005)). Estimating Least Squares parameter with the norm L-1 was popularized under the names Least Absolute Selection and Shrinkage Operator (LASSO: Tibshirani (1994)) and Basis Pursuit Denoising (Chen et al. (1999)). Here, we are going to use the Shooting method for the LASSO minimization problem. We are not explaining the mathematical details of the method, they can be found in Schmidt (2005). This method was chosen as the optimal one in an empirical way. Also, the constant λ is chosen in an empirical way for the regularization with the norm L-1.

We can also add some a priori information to better constrain the least squares solution. In particular, we can equalize the data and the transformation matrix. The equalization is introduced with weighted least squares:

$$\vec{K}' = \bar{\bar{A}}'\vec{D} \tag{4.19}$$

where: $\vec{K}' = \bar{\bar{W}}\vec{K}$ and $\bar{\bar{A}}' = \bar{\bar{W}}\bar{\bar{A}}$; $\bar{\bar{W}}$ - a diagonal matrix with weights.

Note that equation 4.19 is a generalized expression and can be also applied to projections. In addition, we can calculate misfit functions to quantify the residues between the least square solution and the data. We introduce two residues:

- $res_1(\omega)$-frequential misfit function for each frequency
- $r\vec{e}s_2(x, y; \omega)$-spatial misfit function for a given frequency.

These are defined in the following way:

$$res_1 = \frac{||\vec{D} - \bar{\bar{A}}\vec{K}||_2^2}{||D||_2^2} \tag{4.20}$$

$$r\vec{e}s_2 = \vec{K} - \bar{\bar{A}}\vec{D} \tag{4.21}$$

4.2.2 Least Squares with L-2 norm and L-1 normalization: Correlations

We now apply the least squares approach with sensitivity kernels to obtain phase velocity dispersion relations. We use weighted least squares. We define elements of a diagonal weight matrix W as a product of two weights:

$$\bar{\bar{W}} = \Big(w_{ij}\Big) \tag{4.22}$$

where $w_{ij} = 0$ if $i \neq j$ and $w_{ij} = w_1 w_2$ if $i = j$

$$\begin{aligned} w_1 &= \min(\frac{1}{|d_1 - d_2|}, \frac{1}{400}) \\ w_2 &= \frac{1}{d_1}\frac{1}{d_2} \end{aligned} \tag{4.23}$$

where $d_1 = |\vec{r}_1 - \vec{r}_s|$ if $||\vec{r}_1 - \vec{r}_s| \geq d$ or $d_1 = d$ if $|\vec{r}_1 - \vec{r}_s| < d$
$d_2 = |\vec{r}_2 - \vec{r}_s|$ if $||\vec{r}_2 - \vec{r}_s| \geq d$ or $d_2 = d$ if $|\vec{r}_2 - \vec{r}_s| < d$

The weight $\bar{\bar{W}}$ is a combination of two geometrical coefficients. The first one w_1 equalizes the distribution of distances for correlations. We add a lower limit ($\frac{1}{400}$ to avoid values tending to infinity for very small distances). The second coefficient w_2 equalizes the decay of amplitudes of surfaces waves. We now present the dispersion relations calculated with least squares squares using regularization with the norm L-2 (Figure 4.5) and the norm L-1 (Figure 4.5):

We also represent: functions $res_1(\omega)$ (Figure 5c, 6c) and $r\vec{e}s_2$, together with a sensitivity kernel at 4 Hz (Figure 5a,b; Figure 6a,b).

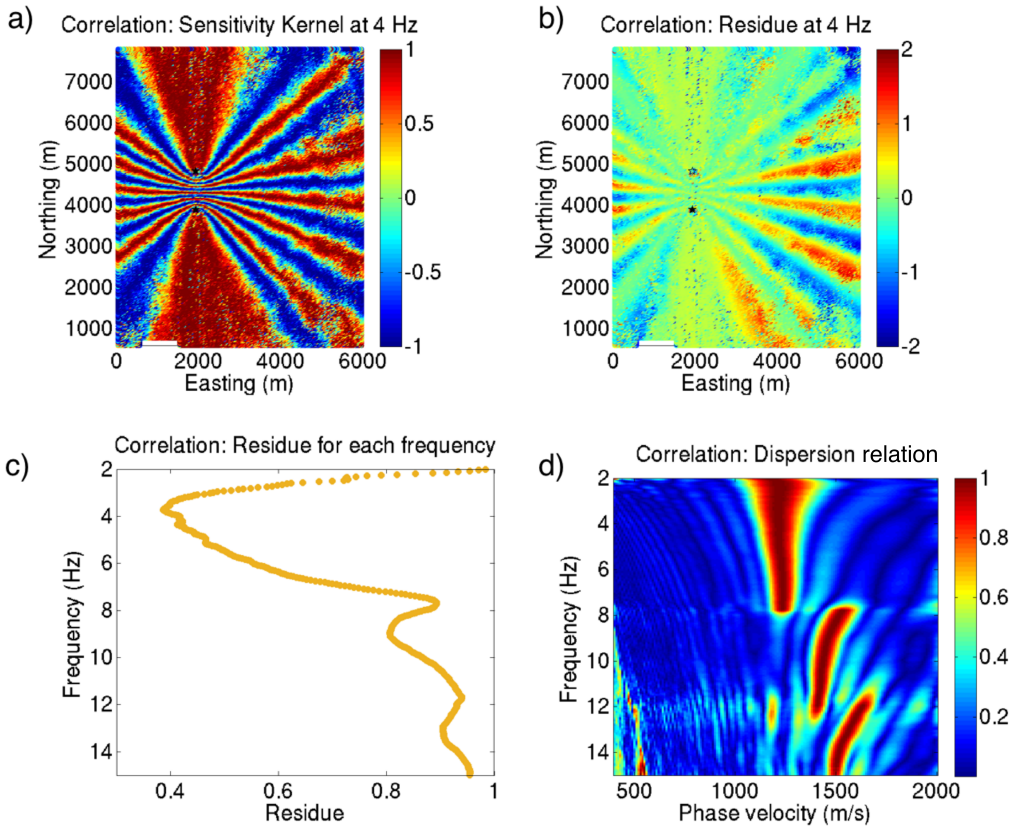

Figure 4.5: Weighted least squares with the L2-norm regularization for the sensitivity kernels from correlations. a) Phase sensitivity kernel at 4 Hz. b) Spatial misfit function $\vec{res}_2$ at 4 Hz. c) Frequential misfit function $res_1(\omega)$. d) Dispersion relation obtained with the weighted least squares.

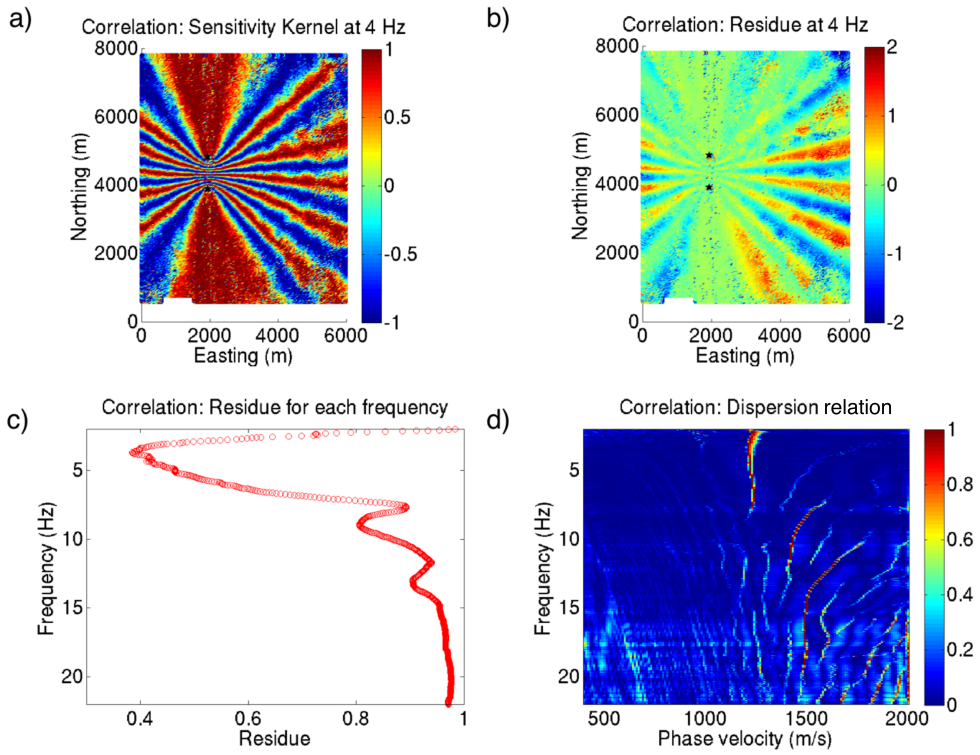

Figure 4.6: Weighted least squares with the L1-norm regularization for the sensitivity kernels from correlations. a) Phase sensitivity kernel at 4 Hz. b) Spatial misfit function $r\vec{e}s_2$ at 4 Hz. c) Frequential misfit function $res_1(\omega)$. d) Dispersion relation obtained with the weighted least squares.

We observe a fundamental mode of surface waves together with two higher modes (Figure 4.5d, 4.6d). We see that the sparse model (regularization with the L-1 norm) explains the data equally well as the "traditional" least squares. The value res_1 and the $r\vec{e}s_2$ at 4 Hz are the same. The found model explains well the stationary phase zone and close offsets, which might be due to the weighting (Figure 4.5b, 4.6b). The value of res_1 increases at set-off frequencies of superior modes (8 Hz, 12 Hz). The quality of the dispersion relation is strongly enhanced in comparison to the projection method. The sparse solution provides a super-resolution. Note that we extract dispersion relations up to 20 Hz using LASSO minimization. This result was obtained only with a suitable pre-conditioning of least squares (weights). We did not use here any integration. We can obtain this kind of dispersion relation for any two points of acquisition.

4.2.3 Least Squares with L-2 norm and L-1 normalization: Convolutions

We now present results of the weighted least squares approach with sensitivity kernels extracted from convolutions. Similarly to the previous section, we define elements for a diagonal weight matrix W as a product of two weights:

$$\bar{\bar{W}} = \Big(w_{ij}\Big) \tag{4.24}$$

Where: $w_{ij} = 0$ if $i \neq j$ and $w_{ij} = w_1 w_2$

$$\begin{aligned} w_1 &= \frac{1}{|d_1 + d_2|} \\ w_2 &= \frac{1}{d_1}\frac{1}{d_2} \end{aligned} \tag{4.25}$$

The weight $\bar{\bar{W}}$ is a combination of two geometrical coefficients. The first one w_1 equalizes the distribution of distances for convolutions. The second coefficient w_2 equalizes the decay of amplitudes of surfaces waves. We now present the dispersion relations calculated with least squares using regularization with the norm L-2 (Figure 4.7).

We also represent: functions $res_1(\omega)$ (Figure 4.7c) and $\vec{res}_2$, together with a sensitivity kernel at 4 Hz (Figure 4.7a, b). The dispersion relation obtained with least squares using L2-norm regularization is less ambiguous than the one obtained with the projection. The maximums corresponding to the fundamental mode and the superior modes of surface waves are clearer. Note that for lower frequencies this dispersion relation has a better resolution that the dispersion relation based on correlations. However, function $res_1(\omega)$ has stronger values for higher frequencies than for correlations. At 4 Hz first few Fresnel zones are better explained by the model than the rest of the sensitivity kernel (Figure 4.7b).

We do not present here results from the least squares with L1-norm. The solution with L2-norm regularization is ambiguous (we observe discontinuities in the dispersion relation) and the L1-norm regularization provides a solution that is more noisy (we verified it in an empirical way).

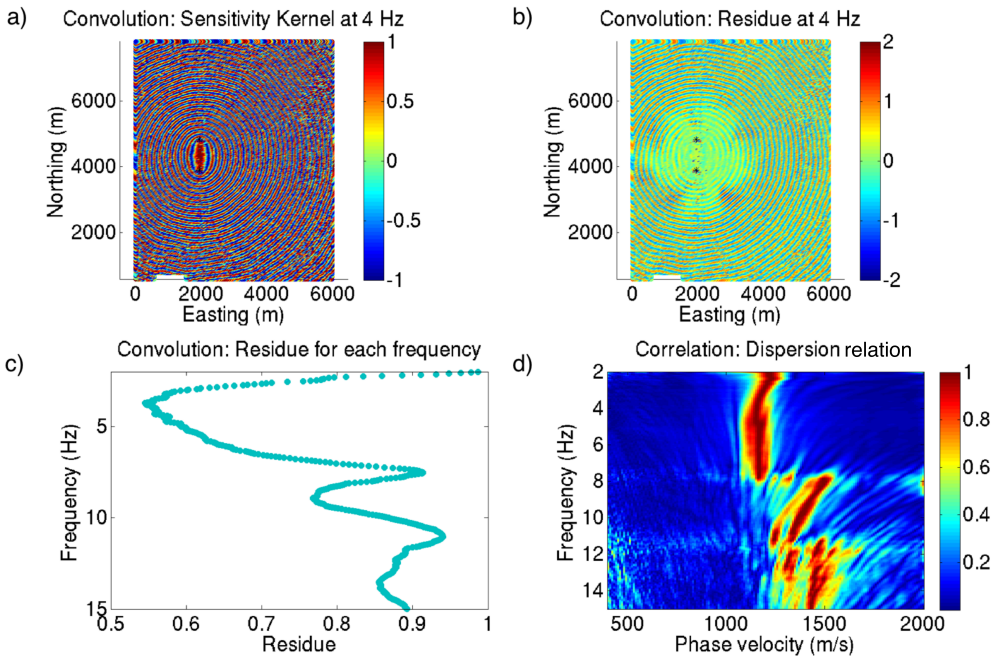

Figure 4.7: Weighted least squares with the L1-norm regularization for the sensitivity kernels from convolutions. a) Phase sensitivity kernel at 4 Hz. b) Spatial misfit function $\vec{res}_2$ at 4 Hz. c) Frequential misfit function $res_1(\omega)$. d) Dispersion relation obtained with the weighted least squares.

4.2.4 Least Squares with L-2 norm and L-1 normalization: Correlations and Convolutions

We observe some discrepancies between dispersion relations from inner and outer kernels. It is due to the difference between mathematical operations in correlation and convolution. In correlations, we subtract the phase of the signals. It is a more robust and stable method than convolution. Due to the sum of phases, convolution provides a higher resolution, but its uncertainty increases fast with the frequency.

We now combine information from both sensitivity Kernels: the ones extracted from correlations and from convolutions. Sensitivity kernels extracted from convolutions provide a better resolution for lower frequencies. However, sensitivity kernels extracted from correlations provide a clearer result for higher frequencies. In order to use both inner and outer sensitivity kernels together, we introduce some weighting in the frequency domain. We put more weight on the convolution (a ratio of 0.7) for the frequencies up to 7.3 Hz and more weight on the correlation (a ratio of 0.95) for higher frequencies. The transition between the weights is smoothed with functions: $\sin^2(x)$ and $\cos^2(x)$ in order to minimize discontinuities.

Results of weighted least squares with combined sensitivity kernels from convolutions and correlations are presented on Figure 4.8. The sparse solution (Figure 4.8d) is more sensitive to the interference between higher modes. We observe some artefacts caused by differences between dispersion relations obtained from inner and outer sensitivity kernels. However, we see that the dispersion relation with the norm L2 (Figure 4.8b) has a better resolution for lower frequencies than the dispersion relation from correlations. Function $res_1(\omega)$ (Figure 4.8a,c) shows the same values for both solutions.

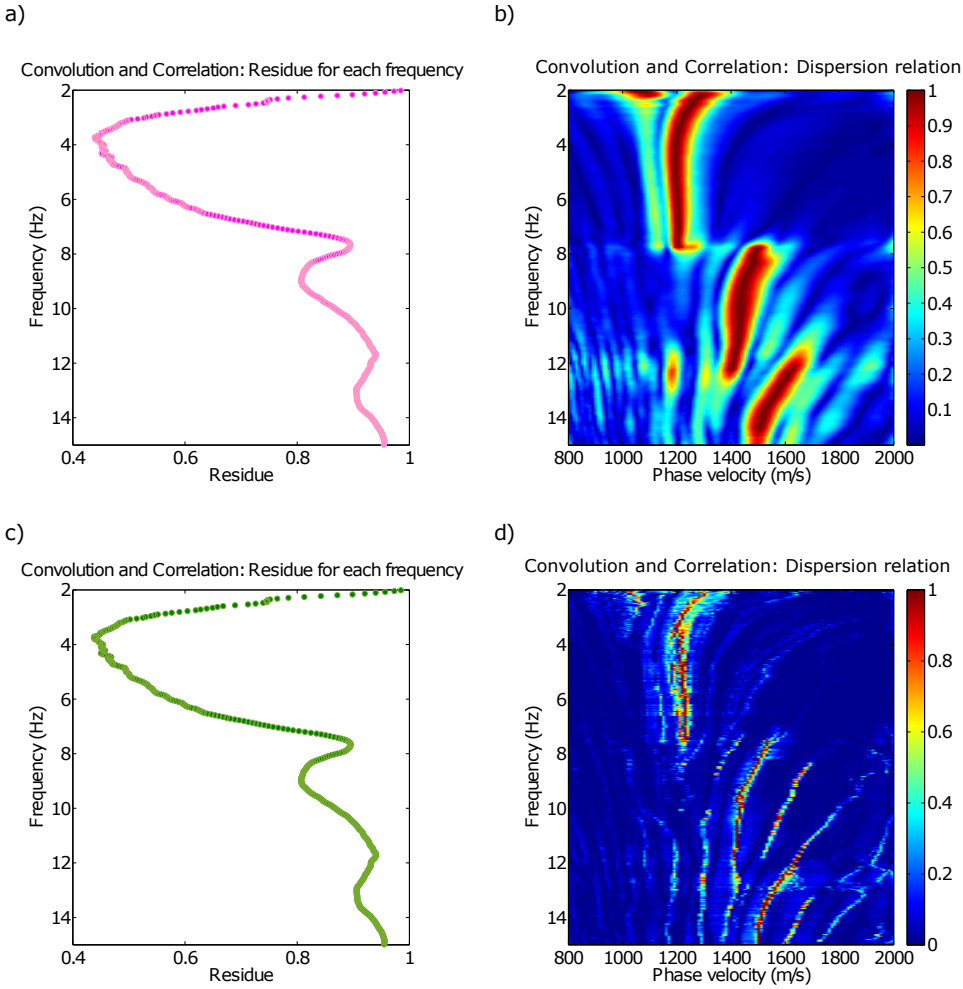

Figure 4.8: Joint dispersion relation analysis. Weighted least squares with the sensitivity kernel from correlations and convolutions used conjointly. a) Function $res_1(\omega)$ for weighted least squares with the norm L2; b) dispersion relation for weighted least squares with the norm L2; c) function $res_1(\omega)$ for weighted least squares with the norm L1; d) dispersion relation for weighted least squares with the norm L1.

We now apply a joint inversion of sensitivity kernels to another position in space. We keep

the same parameters for the weighting in the frequency domain. The distance between the two receivers is of 1000 m. Figure 4.9 presents the outer sensitivity kernel (Figure 4.9a) and the inner sensitivity kernels (Figure 4.9b) for the frequency 3.6 Hz. Misfit function $res_1(\omega)$ shows higher values than in the previous configuration. However, the dispersion relation obtained with the L2-norm regularization is clear (Figure 4.9c). In this configuration we observe only one superior mode of surface waves (Figure 4.9d). However, the set off frequency (8 Hz) for the first higher mode is the same as in the first configuration.

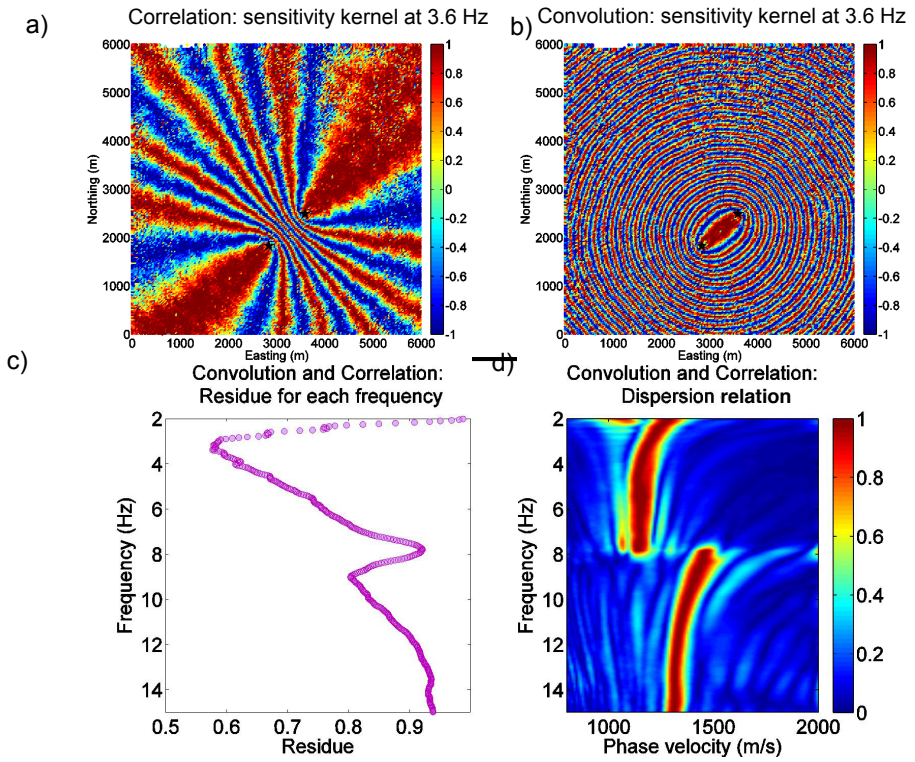

Figure 4.9: Sensitivity Kernels from correlations and convolutions are used conjointly with weighted least squares algorithm. a) Sensitivity Kernel from correlation at 3.6 Hz; b) Sensitivity Kernel from convolution at 3.6 Hz; c) residue for weighted least squares with norm L2; d) dispersion relation for weighted least squares with norm L2.

4.2.5 Inversion of phase velocity dispersion curve

Weighted least squares provide high quality dispersion relations. It allows to easily pick the maximum of the dispersion relations in both configurations to obtain the actual dispersion curves. We use software Geopsy (Wathelet et al. (2004)) to invert surface waves in order to obtain P- and S- wave velocity profiles.

This software performs surface waves inversion and calculates phase velocity dispersion curves (Figure 4.10, 4.11). Misfit is represented with the color scale. Superior modes of Rayleigh

waves constrain information about S-wave profiles and allow extracting P-wave profiles (with a higher uncertainty). The third dispersion curve in Figure 4.10b can be perturbed by another, higher mode of surface waves (so called ”mode-kissing”). The surface waves modes overlap in the frequency domain. We pick only the maximums of the dispersion relation without overlapping frequency bands. However, Geopsy calculates dispersion curves for broader frequency bands (Figure 4.10b, Figure 4.11b), separately for each mode.

Note, that this inversion can be performed for any two points in the medium. It gives valuable information about the near-surface that can be used to improve existing models of the medium and for static corrections.

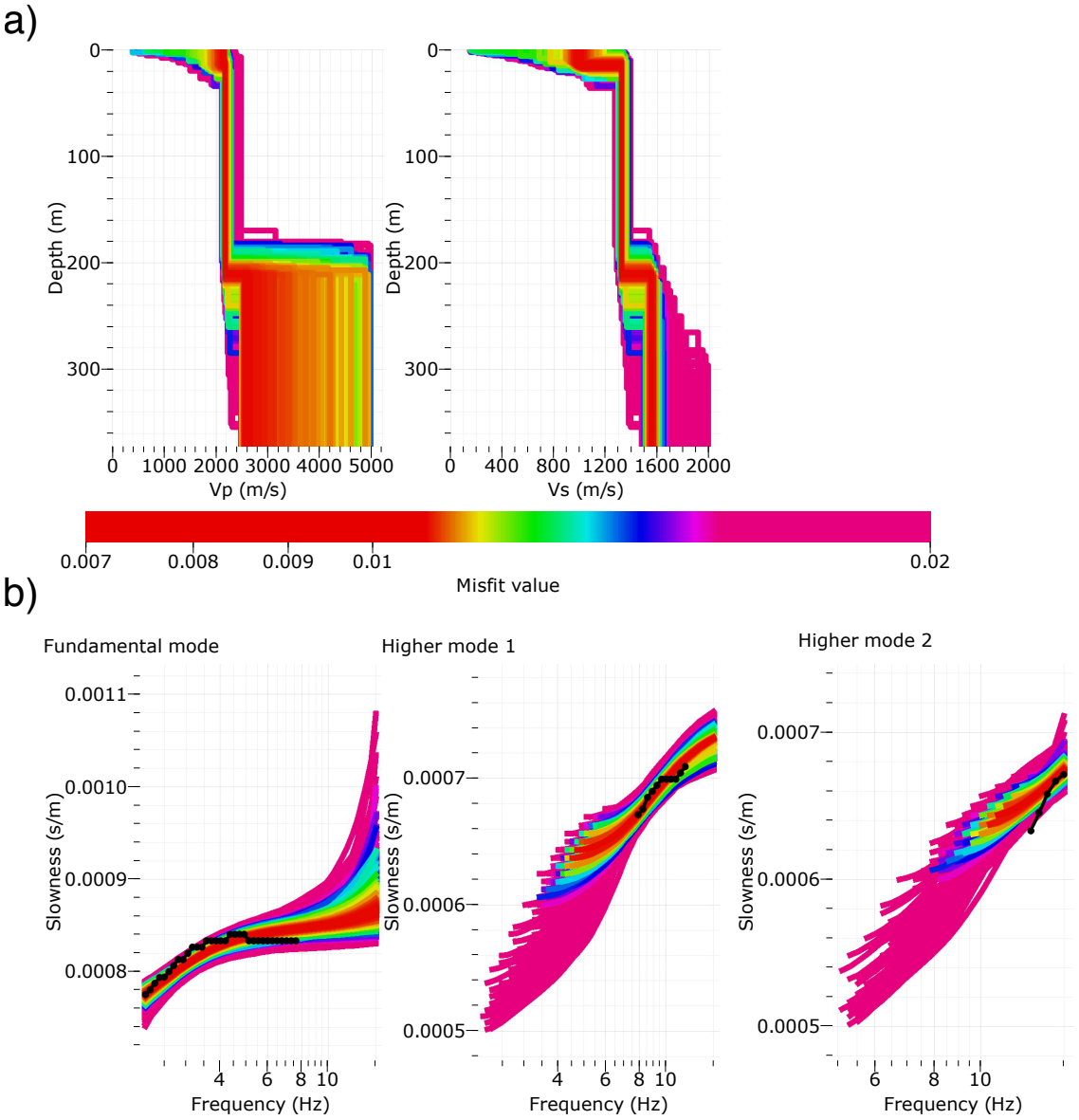

Figure 4.10: Inversion of surface waves in configuration 1. a) Left: P-wave velocity profile; Right: S-wave velocity profile, b) Dispersion curves for the fundamental mode and two higher modes (courtesy: M. Wathelet).

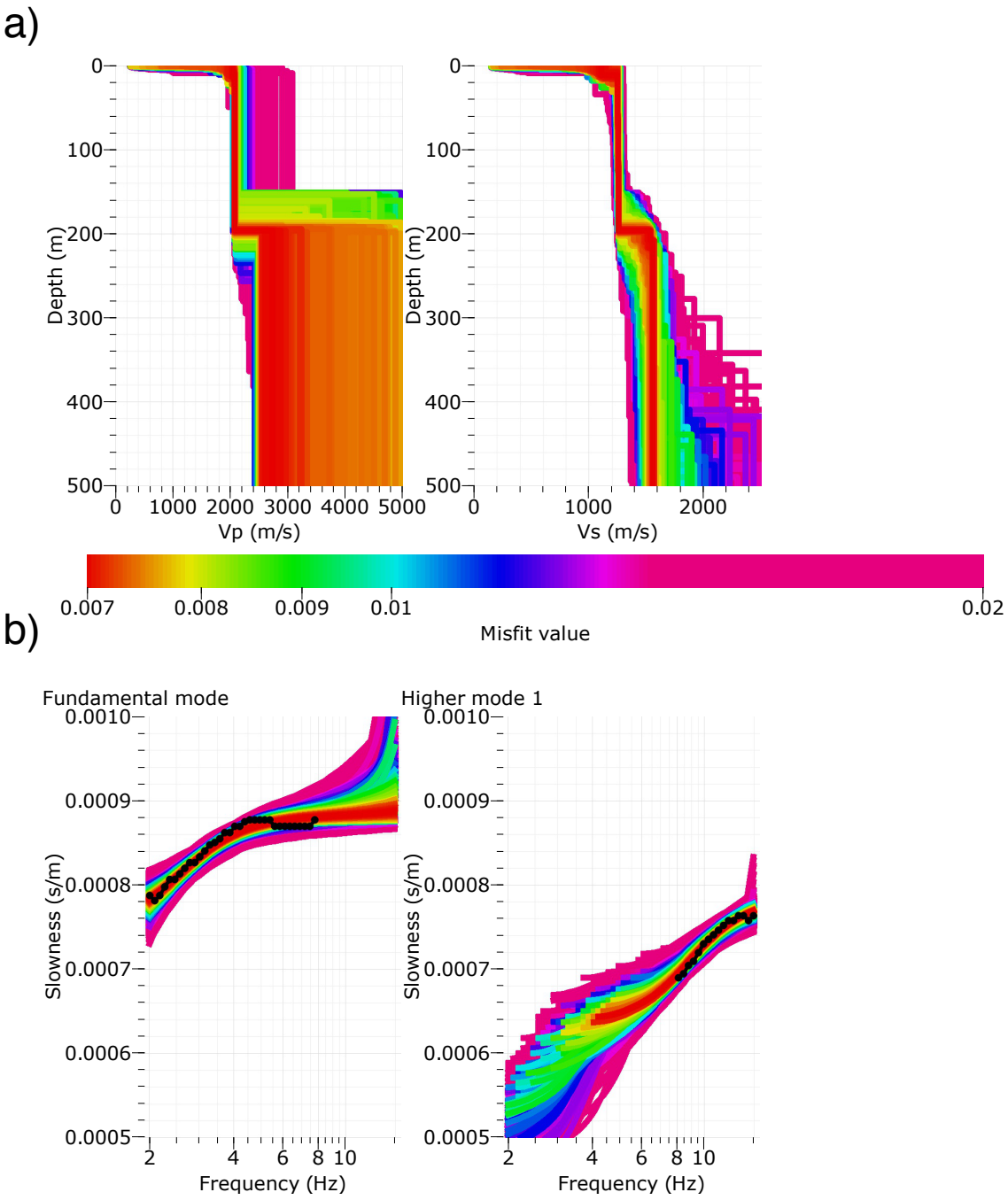

Figure 4.11: Inversion of surface waves in configuration 2. a) Left: P-wave velocity profile; Right: S-wave velocity profile, b) Dispersion curves for the fundamental mode and two higher modes (courtesy: M. Wathelet).

4.3 Higher modes of Rayleigh waves: Modes separation

Separation of higher modes of Rayleigh waves can be complicated due to their overlap in the frequency domain and simultaneous arrivals. However, high quality dispersion relations obtained between two points can ease this issue. We now use the dispersion relations to separate the modes. In particular, we focus on the first configuration, where three overtones are present. We use the dispersion relation from correlations. First, we perform an improved picking of the modes in order to extract them in overlapping frequencies bands: (2-9.49) Hz, (7-11.96) Hz, and (9.7-15) Hz. Next, we apply masks to the dispersion relations. For each mode we apply a Gaussian mask to preserve only the dispersion relation for a specific mode. Then, we calculate the inverse hyperbolic transform in order to return into the (x,y) space:

$$K^{Inv}_{Corr}(x,y;\omega) = \sum_{c_0} \left(\exp\left(-\frac{i\omega}{c_0}(|\vec{r}_1 - \vec{r}_{xy}|) - |\vec{r}_2 - \vec{r}_{xy}| \right) CCorr^{1,2}(\omega, c_0) \right) \tag{4.26}$$

Now, we sum $K^{Inv}_{Corr}(x,y;\omega)$ for all the sources and we return into the time domain with the inversed Fourier transform (we create a virtual trace). Figure 4.12a shows a virtual trace in the frequency band (2-15) Hz. Figure 4.12b, c, d presents the separated modes in the previously specified frequency bands together with envelopes of the traces. The fundamental mode seems less dispersive than the two others. We also observe a trend of increasing group velocities. These conclusions agree with the observed dispersion relations for those modes.

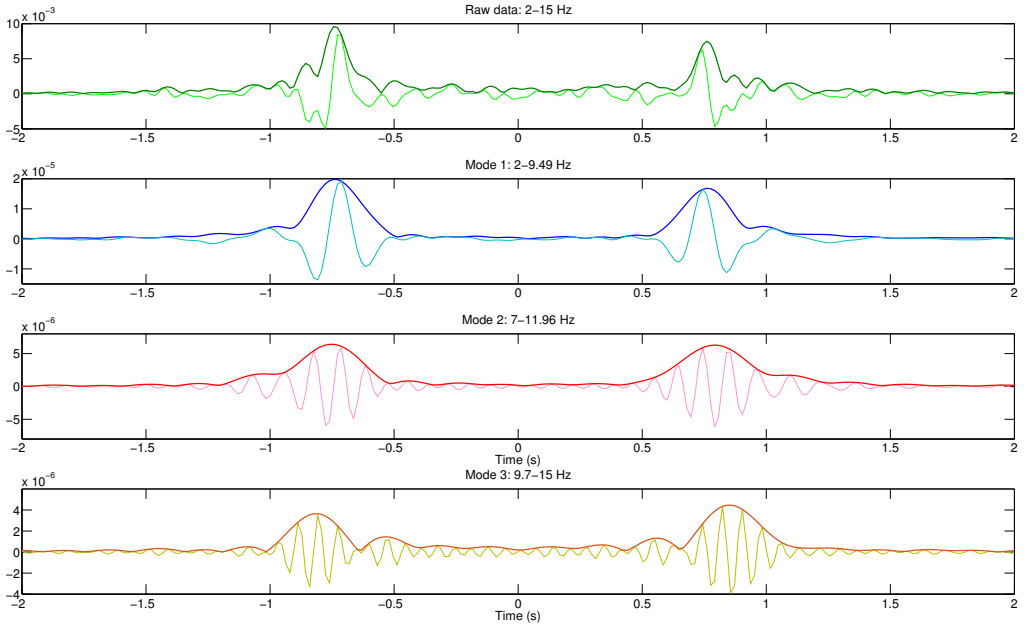

Figure 4.12: Modes separation for Rayleigh waves. a) Virtual trace in the frequency band (2-15) Hz, b) Fundamental model in the frequency band (2-9.49) Hz, c) Second mode in the frequency band (7-11.96) Hz, d) Third mode in the frequency band (9.7-15) Hz.

4.4 Conclusions

In this chapter, we presented possible applications of phase sensitivity kernels extracted from correlation and convolution. We might use the kernels to retrieve high quality phase velocity dispersion relations for any two points in the medium, up to 20 Hz. Dispersion relations from convolutions have a better resolution in lower frequencies (due to the sum of phases in convolution); while dispersion relation from correlation show more stability in higher frequencies (due to the difference of phases in correlation). This is the reason why we decided to combine both dispersion relations with an adequate weighting in the frequency domain. These joint dispersion relations are consequently inverted to find S-wave and P-wave velocity profiles. This method can add valuable information about the near-surface. We might obtain these velocity profiles for every two points in the medium to map the near surface properties. We can also use the dispersion relations to separate different modes of Rayleigh waves. Here, we present an example using sensitivity kernels from correlations, but we can apply the same methodology with convolutions. High quality of the dispersion relations allows us to apply a simple solution to a complex problem, which is modes separation. These are examples of the potential use of the phase sensitivity kernels. Other applications can be envisaged as well, such as: group- and phase- velocity tomography, mapping the near surface structures and retrieving the static corrections.

Conclusions and Perspective

High trace density opens new possibilities in geophysical processing in both passive and active surveys. Depending on the aim of the processing, we explore various approaches in different frequency bands: passive sources: at the surface (from 2 Hz to 10 Hz) and at depth (from 10 Hz to 60 Hz) with correlations-based methods; and active sources with: convolutions (from 2 Hz to 6 Hz) and correlations (from 6 Hz to 20 Hz) (Figure 1).

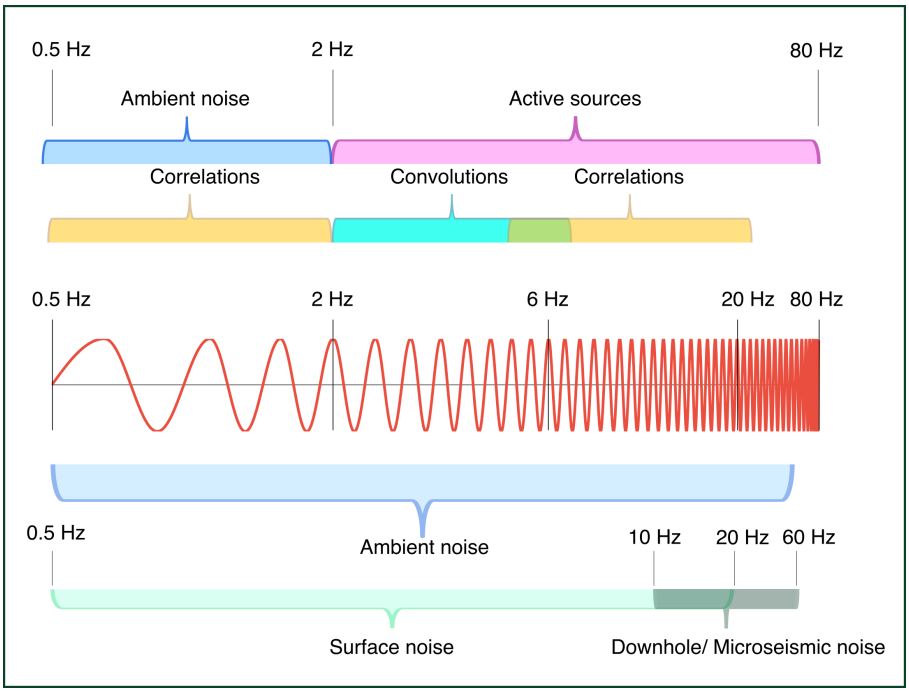

Figure 1: Geophysical processing with passive and active sources as a function of the frequency band of interest.

1 Conclusions

In the first part we have investigated the possibilities of combining a patch array acquisition with array processing methods. The main ingredient is the use of Matched Field Processing to explore noise sources within the network. The patch-array design at the surface gives a possi-

bility to use alternative approaches by taking advantage of ambient noise correlations. MFP is successfully applied to determine noise sources at the surface and at depth.

At the surface, localized, punctual noise sources provide significant physical importance and, what is more, they accelerate the convergence towards the noise-correlation function. Contrary to low-frequency ambient-noise tomography that classically requires long averaging periods (i.e., several hours to days), a duration of 15-min was sufficient to produce the phase velocity maps and 150-min to produce the group velocity maps in this study. The use of directional sources seems to be more adapted in land exploration geophysics due to limited time of recording and the presence of strong human-related noise sources. The human-related sources such as pumps, wells and drilling platforms generate noise, which propagates as surface waves. These sources of opportunity are often situated within the network area. Thanks to the acquisition with patches we can explore the noise sources within the network, not only on the outside. These sources can occur in the frequencies from at least 2 Hz to 20 Hz or even higher. We explore them in the frequency band (2-10) Hz.

At depth, detected and localized downhole noise sources provide information about the distribution of heterogeneities in the reservoir, in the well vicinity. The proposed location method is efficient and allows real-time processing. The only a priori needed is a homogenous velocity model, adapted to data. This approach cannot replace existing, more elaborated and precise techniques: like a relative method or methods that use the inversion of a source mechanism. However, it might provide the first insight into the reservoir. We propose a simple method, easy to implement in an automatic way that directly yields information about the sub-surface, separating noise sources on the surface and at depth. The downhole noise sources are explored in the frequency band of (10-60) Hz.

We might process patches coherently in a joint manner or work patch per patch. The surface noise sources can be attenuated with the use of MRABF algorithm. If we focus on the processing of surface waves (e.g. to detect and locate surface sources or to suppress surface waves) we should privilege working per patch. Surface noise is highly coherent within a patch. However, the joint use of patches strongly decreases the coherence of surface noise, while preserving the coherence of downhole signals. In consequence, we observe significantly more detections if patches are used in a joint manner.

In the second part, we present a new approach in processing surface waves from active seismic data. Seismic surveys with active, controlled sources gives more possibilities when it comes to interferometry. The use of controlled sources enables the recovery of the surface wave Green's function between two points using either correlation or convolution. We investigate the convolutional and correlational approaches using land active-seismic data from exploration geophysics. Invoking spatial reciprocity between sources and receivers, correlation and convolution functions can thus be constructed between either pairs of receivers or pairs of sources. High density of sources and the application of the reciprocity principle allow us to retrieve phase oscillations ker-

nels of surface waves between two points in the medium. These kernels can be calculated with correlations or convolutions.

Next, the phase oscillations kernels are used to retrieve high quality dispersion relations. The inner sensitivity kernels obtained with convolutions provide high resolution in lower frequencies: $\sim$(2-6) Hz due to the phase summation. In higher frequencies (from 6 Hz up to 20 Hz) outer sensitivity kernels obtained with correlations appear more stable due to the phase difference. We might combine both inner and outer phase sensitivity kernels to obtain phase velocity dispersion curves for any two points in the medium, up to 20 Hz. These joint dispersion relations are consequently inverted to find S-wave and P-wave velocity profiles. This method can add valuable information about the near-surface. We might obtain the velocity profiles for every two points in the medium to map the near surface properties. We can also use the dispersion curves to separate different modes of Rayleigh waves. We present an example using sensitivity kernels from correlations, but we can apply the same methodology with convolutions. High quality of the dispersion relations allows us to apply a simple solution to a complex problem, which is modes separation.

This work succesfully bridges industrial challenges (such as surface noise, source localization, imaging of the near surface) with academical methods (such as noise-correlations, beamforming, data-based sensitivity kernels calculated with correlation and convolution). The methodologies presented above benefit from spatially dense networks. The dense arrays give new possibilities in geophysical processing.

2 Perspectives

Presented works give numerous perspectives in active and passive seismic configurations. We now present possible paths for the future studies.

The multi-scale approach paves the way to substantially more accurate inversion of surface waves and production of wide and accurate maps of static corrections due to strong constraints coming from both local phase velocities and group velocity maps. We are able to extract information about the subsurface using only the ambient noise recorded during acquisition and the present methodology; no extra costs are needed. The spatial coherence associated with this local incoherent source will build rapidly over time, and can be used as a coherent source by the patch-array design. The methodology we describe here opens the route to environmental monitoring of the subsurface from the repetitive inversion of phase and group velocity maps with ambient-noise surface sources.

Matched Field Processing methods allowed detecting and locating noise sources in the reservoir, in the well proximity. No information a priori is needed, only a homogenous velocity that is adapted to the medium. The results of our processing might help to better understand the origin of the downhole noise and to distinguish between possible noise sources (e.g., downhole noise, microseismic activity or long-period, long duration seismic events). This method is easy to ap-

ply and opens a route to continuous, easily implemented, purely automatic reservoir monitoring. Possible applications can be envisaged in monitoring of volcanic, geyser or other natural seismic activity. For example, this method could be applied with a spatially dense array that was deployed at the damage zone of the Clark branch of the San Jacinto Fault Zone south of Anza, California (Figure 2: Roux et al. (2016)).

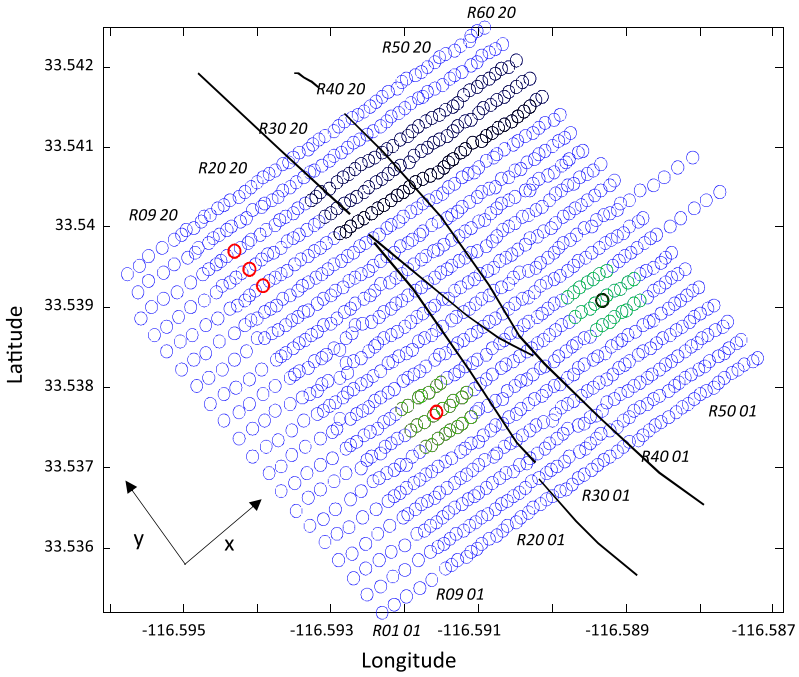

Figure 2: "Map of the 1108 geophones installed in a 650 x 700 m2 configuration above the Clark branch (black lines) of the San Jacinto Fault (Southern California). Each row along the x-direction is composed of 55 sensors with an interdistance of 10 m, and the nominal separation between the rows in the y-direction is 30 m. Seismic ambient noise was recorded over more than one month, in May-June 2014" (after Roux et al. (2016)).

Of course, if more a priori information is available (e.g., a located perforation shot) we might use a relative processing that would increase the sensibility of the method. Also, working in frequency domain allows to specified frequency bands of interest. Here, we used a broad frequency band (10-60) Hz to locate downhole sources of noise. However, narrow frequencies bands (such as: (10-20) Hz, (20-30) Hz etc) can be used to determine the distribution of different size depth sources (bigger fractures in lower frequencies and smaller fractures in higher frequencies). For the patch acquisition, it would be profitable to deploy 3-components patches to record also the S-waves. It would allow optimizing the velocity model and localize more precisely seismic events with a lower vertical uncertainty.

Yet, the best would be to merge the passive and the active techniques. To retrieve high quality phase velocity and group velocity maps, we might multiply the number of "controlled" and

localized sources. Noise can for example be generated by a truck that continuously and locally circles in one position in the field for a few minutes. After a few minutes of continuous seismic ambient noise generated locally by the truck (i.e., typically 5 or 10 min), this one could then move to another position with the same strategy.

Passive and active sources give complementary information in different frequency bands. Ambient noise sources can provide information below 2 Hz, where active sources cannot be used. The typical range of frequencies is between 10 Hz and 80 Hz in active surface seismic. Very low frequencies are hard to obtain in active experiments: the use of active sources in low frequency regime might be too destructive. However, low frequency improves the vertical resolution and facilitates the exploration of deep targets (Draganov et al. (2009): Figure 2). The best solution is to combine information from passive and active seismic. Of course, an ideal case would consist of a spatially dense array that continuously (e.g. during a few days) records: ambient noise and additional experiments with active sources.

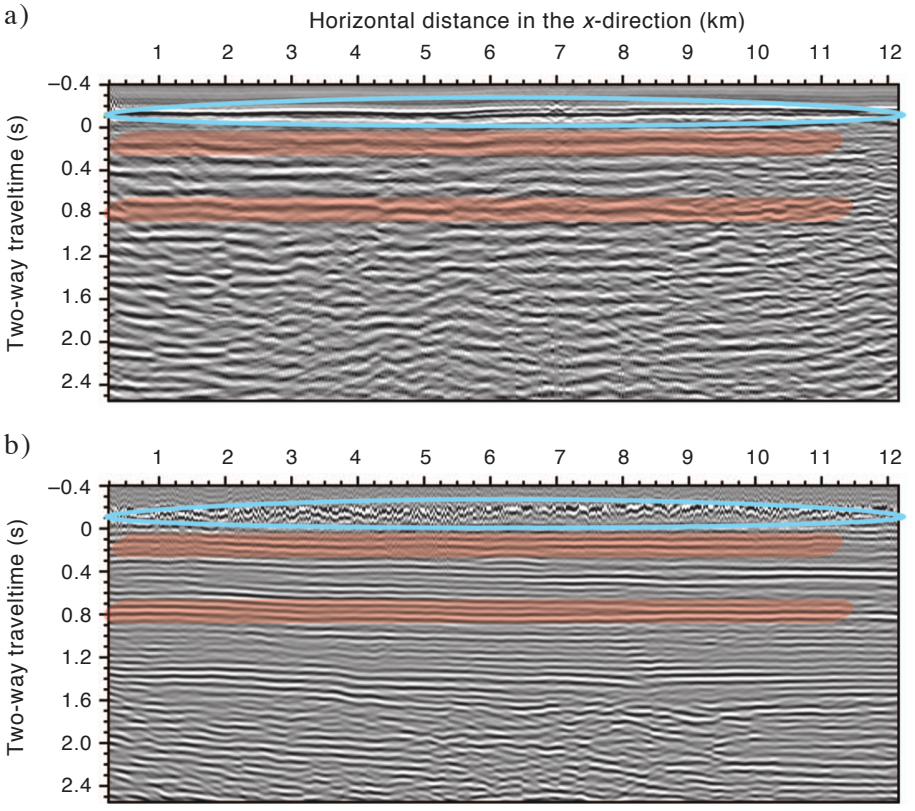

Figure 3: "Poststack time-migrated sections a) the interferometric shot gathers and b) the active data. Coinciding imaged reflectors are highlighted in transparent red. The blue ellipses indicate the earth's surface. Zero time refers to mean sea level"' (after Draganov et al. (2009)).

Another possibility is to extract sensitivity kernels with correlations and convolutions, but for P-waves. First, by using double beamforming or wave-separation algorithms (e.g. Singular

Value Decomposition) we could retrieve body waves from the data (Figure 4). Then, we could retrieve the sensitivity kernels for P- waves with convolutions and correlations. Due to the use of controlled sources, we could focus on exploring different waves: refracted and reflected body waves, back-scatter noise. These are examples of the potential use of the phase sensitivity kernels. Other applications can be envisaged as well, such as: group- and phase- velocity tomography, mapping the near surface structures and retrieving the static corrections.

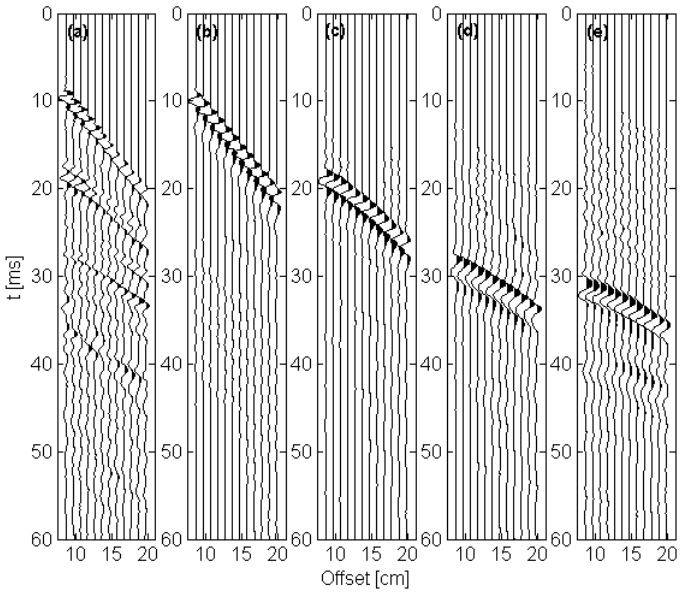

Figure 4: Waves extracted after Double beamforming processing: a) Raw data; b) Direct surface wave; c) Reflected surface wave; d), e) Reflected body waves (after de Cacqueray et al. (2011)).

Spatially dense arrays allow to develop new approaches in exploration geophysics: they enable alternative, innovative applications in geophysical processing to aim the industrial challenges.

Appendix A

Presented within is a theoretical approach to derive the Green's function between two points and controlled sources with convolutions and correlations. We will follow a similar path of reasoning as was presented by Roux et al. (2005) for cross-correlations. Let's consider a free space with attenuation. Volume attenuation is added in the medium by including an imaginary component to the wave speed $c = c_0 + ic_i$, with $c_i << c_0$. We now consider a geometry with two receivers 1 (in $\vec{r_1}$) and 2 (in $\vec{r_2}$) and a source s in $\vec{s}$ (Figure 1a).

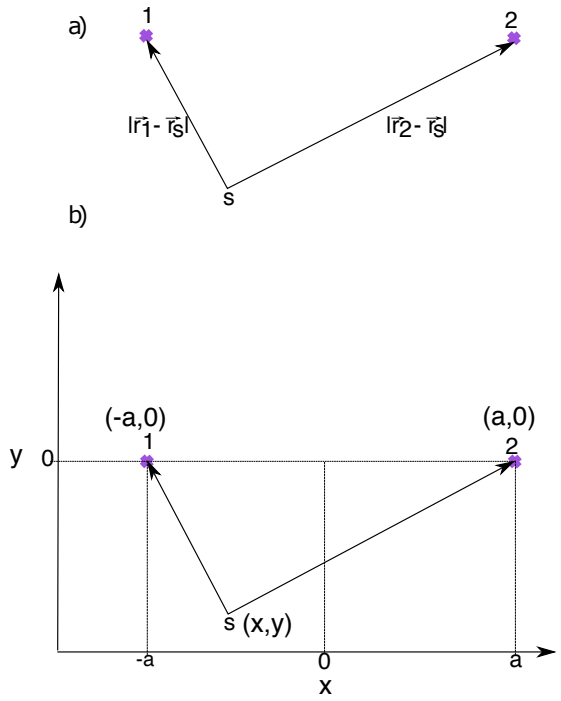

Figure 1: a) Two receivers 1 and 2 and a source s. b) Representation in the xy plane of the receivers 1 and 2 that are at (a,0) and (-a,0) and the source s in (x,y).

The Green's functions in a 3D homogenous medium with attenuation between the source s (in $\vec{r_s}$) and the points: 1 (in $\vec{r_1}$) and 2 (in $\vec{r_2}$) are defined in the following way:

$$G_{s,1}(\omega) = \frac{1}{4\pi}\frac{1}{|\vec{r_s} - \vec{r_1}|}\exp\left(\frac{i\omega}{c_0}|\vec{r_s} - \vec{r_1}|\right)\exp\left(\frac{-\omega c_i}{c_0^2}|\vec{r_s} - \vec{r_1}|\right) \quad (1)$$

$$G_{s,2}(\omega) = \frac{1}{4\pi}\frac{1}{|\vec{r_s} - \vec{r_2}|}\exp\left(\frac{i\omega}{c_0}|\vec{r_s} - \vec{r_2}|\right)\exp\left(\frac{-\omega c_i}{c_0^2}|\vec{r_s} - \vec{r_2}|\right) \tag{2}$$

The Green's function in a 3D homogenous medium with attenuation between point 1 (in r1) and 2 (in r2) is defined in the following way:

$$G_{1,2}(\omega) = \frac{1}{4\pi}\frac{1}{|\vec{r_1} - \vec{r_2}|}\exp\left(\frac{i\omega}{c_0}|\vec{r_1} - \vec{r_2}|\right)\exp\left(\frac{-\omega c_i}{c_0^2}|\vec{r_1} - \vec{r_2}|\right) \tag{3}$$

In the time domain the Green's function between the point 1 and 2 is:

$$G_{1,2}(t) = \frac{1}{2\pi}\int_{-\infty}^{\infty} G_{1,2}(\omega)\exp(i\omega t)d\omega \tag{4}$$

Which can be written as:

$$G_{1,2}(t) = \frac{1}{8\pi}\int_{-\infty}^{\infty} d\omega\frac{1}{|\vec{r_1} - \vec{r_2}|}\exp\left(i\omega\left(t + \frac{|\vec{r_1} - \vec{r_2}|}{c_0}\right)\right)\exp\left(\frac{-\omega c_i}{c_0^2}|\vec{r_1} - \vec{r_2}|\right) \tag{5}$$

We now define a Cartesian coordinate system (the same as presented on the figure 3.9) for the 3D space in which receiver 1 is in (a,0,0), receiver 2 is in (-a,0,0), and the source s is in (x,y,z) (Figure 1b). Now, the Green's function between the point 1 and the point 2 yields:

$$G_{1,2}(t) = \frac{1}{8\pi}\int_{-\infty}^{\infty} d\omega\frac{1}{2a}\exp\left(i\omega\left(t + \frac{2a}{c_0}\right)\right)\exp\left(\frac{-\omega c_i}{c_0^2}2a\right) \tag{6}$$

We now consider correlation and convolution of two signals recorded at 1 and 2 from a single source s.

Correlation

1. The correlation of two signals recorded at A and B is defined as:

$$Corr_{1,2}^{s}(\omega) = G_{s,1}(\omega)G_{s,2}^{*}(\omega) \tag{7}$$

2. If we use the Green's functions defined in equations 1 and 2 the correlations become:

$$Corr_{1,2}^{s}(\omega) = \frac{1}{(4\pi)^2}\frac{1}{|\vec{r_s} - \vec{r_1}|}\frac{1}{|\vec{r_s} - \vec{r_2}|}\exp\left(\frac{i\omega}{c_0}(|\vec{r_s} - \vec{r_1}| - |\vec{r_s} - \vec{r_2}|)\right)$$
$$\exp\left(\frac{-\omega c_i}{c_0^2}(|\vec{r_s} - \vec{r_1}| + |\vec{r_s} - \vec{r_2}|)\right) \tag{8}$$

3. Function $Corr_{1,2}(\omega)$ corresponds to one realization of the correlation function. However, we want to evaluate the average correlation function over an ensemble of realization. We introduce a sum for different sources. These sources can be incoherent, e.g. decorrelated noise sources.

$$\langle Corr_{1,2}(\omega, \vec{r_s})\rangle = \int_{\vec{r_s}} d\vec{r}_s\frac{1}{(4\pi)^2}\frac{1}{|\vec{r_s} - \vec{r_1}|}\frac{1}{|\vec{r_s} - \vec{r_2}|}\exp\left(\frac{i\omega}{c_0}(|\vec{r_s} - \vec{r_1}| - |\vec{r_s} - \vec{r_2}|)\right)$$
$$\exp\left(\frac{-\omega c_i}{c_0^2}(|\vec{r_s} - \vec{r_1}| + |\vec{r_s} - \vec{r_2}|)\right) \tag{9}$$

4. We now perform a change of variable from the Cartesian coordinates to the hyperbolic coordinate system in order to solve the spatial integration in equation 8:

$$\begin{cases} x = a\sin(\theta)\cosh(\varphi) \\ y = a\cos(\theta)\sinh(\varphi)\cos(\psi) \\ z = a\sin(\theta)\cosh(\varphi)\sin(\psi) \end{cases} \tag{10}$$

where:

$$\begin{cases} \varphi \in \mathbb{R}^+ \\ \theta \in (-\frac{\pi}{2}, \frac{\pi}{2}) \\ \psi \in (0, 2\pi) \end{cases} \tag{11}$$

The Jacobian of the change of variable is:

$$J(\varphi, \theta, \psi) = a^3\cos(\theta)\sinh(\varphi)\left(\cosh^2(\varphi) - \sin^2(\theta)\right) \tag{12}$$

Then, for any point $\vec{r}_s$ defined by the coordinates (φ, θ, ψ):

$$\begin{aligned} |\vec{r}_s - \vec{r}_1| &= a(\cosh(\varphi) + \sin(\theta)) \\ |\vec{r}_s - \vec{r}_2| &= a(\cosh(\varphi) - \sin(\theta)) \end{aligned} \tag{13}$$

$$\begin{aligned} |\vec{r}_s - \vec{r}_1||\vec{r}_s - \vec{r}_2| &= a^2(\cosh^2(\varphi) - \sin^2(\theta)) \\ |\vec{r}_s - \vec{r}_1| - |\vec{r}_s - \vec{r}_2| &= 2a(\sin(\theta)) \\ |\vec{r}_s - \vec{r}_1| + |\vec{r}_s - \vec{r}_2| &= 2a(\cosh(\varphi)) \end{aligned} \tag{14}$$

5. We now apply the change of variables:

$$\langle Corr_{1,2}(\omega, \varphi, \theta, \psi)\rangle = \frac{1}{(4\pi)^2}\int_0^\infty d\varphi \int_{-\frac{\pi}{2}}^{\frac{\pi}{2}} d\theta \int_0^{2\pi} d\psi \; a\cos(\theta)\sin(\varphi)\exp\left(\frac{i\omega}{c_0}(2a\sin(\theta))\right) \exp\left(-\frac{\omega c_i}{c_0^2}(2a\cosh(\varphi))\right) \tag{15}$$

Now, we consider the integrals separately.

The presence of attenuation in the medium makes the integral over φ converge as:

$$\int_0^\infty d\varphi \sinh(\varphi)\exp\left(-\frac{2a\,\omega c_i}{c_0^2}\cosh(\varphi)\right) = \frac{c_0^2}{2a\,\omega c_i}\exp\left(-\frac{2a\,\omega c_i}{c_0^2}\right) \tag{16}$$

While the integral over θ gives:

$$\int_{-\frac{\pi}{2}}^{\frac{\pi}{2}} d\theta\, a\cos(\theta)\exp\left(\frac{2a\,i\omega}{c_0}\sin(\theta)\right) = \begin{cases} a\sin(\theta) = x \\ a\sin(\theta)d\theta = dx \end{cases} = \int_{-a}^{a} dx \exp\left(\frac{i\omega}{c_0}2x\right) = \frac{c_0}{2\,i\omega}\left(\exp\left(\frac{2a\,i\omega}{c_0}\right) - \exp\left(-\frac{2a\,i\omega}{c_0}\right)\right) \tag{17}$$

And:

$$\int_0^{2\pi} d\psi \; = 2\pi \tag{18}$$

6. Finally, combining equations 16, 17, 18 it follows:

$$\langle Corr_{1,2}(\omega)\rangle = \frac{1}{16\pi}\frac{c_0^3}{2a\,\omega c_i}\frac{1}{i\omega}\left(\exp\left(\frac{2a\,i\omega}{c_0}\right) - \exp\left(-\frac{2a\,i\omega}{c_0}\right)\right)\exp\left(-\frac{2a\,\omega c_i}{c_0^2}\right) \tag{19}$$

7. The averaged correlation function in the time domain yields:

$$\langle Corr_{1,2}(t)\rangle = \frac{1}{16\pi}\frac{c_0^3}{2a\,c_i}\frac{1}{2\pi}\int_{-\infty}^{\infty}\frac{d\omega}{i\omega}\frac{1}{\omega}\exp\left(-\frac{2a\,\omega c_i}{c_0^2}\right)\exp(i\omega t)\left(\exp\left(\frac{2a\,i\omega}{c_0}\right) - \exp\left(-\frac{2a\,i\omega}{c_0}\right)\right) \tag{20}$$

8. The time derivate of the correlation functions reads:

$$\frac{d}{dt}\langle Corr_{1,2}(t)\rangle = \frac{c_0^3}{4\pi c_i}\Big(\int_{-\infty}^{\infty}\frac{d\omega}{\omega}\frac{1}{8\pi}\frac{1}{2a}\left(\exp\left(i\omega(t+\frac{2a}{c_0})\right)\exp\left(-\frac{2a\,\omega c_i}{c_0^2}\right)\right) - \int_{-\infty}^{\infty}\frac{d\omega}{\omega}\frac{1}{8\pi}\frac{1}{2a}\left(\exp\left(i\omega(t-\frac{2a}{c_0})\right)\right)\exp\left(-\frac{2a\,\omega c_i}{c_0^2}\right)\Big) \tag{21}$$

This integral is proportional to the Green's function from 1 to 2 and its time-reversed equivalent from 2 to 1 (equation 5). However, we observe the coefficient depending on the attenuation before the integral. It means that the attenuation in the medium will influence the estimate of the Green's function (Roux et al. (2005)). This mathematical development shows that the derivative of the correlation function gives an estimate of the causal part and the anticausal part of Green's function between the two points at which signal has been recorded:

$$\frac{d}{dt}\langle Corr_{1,2}(t)\rangle = \frac{c_0^3}{4\pi c_i}\frac{1}{\omega}(G_{12}(t) - G_{21}(t)) \tag{22}$$

Convolution

1. The convolution of two signals recorded at A and B is defined as:

$$Conv_{1,2}^s(\omega) = G_{s,1}(\omega)G_{s,2}(\omega) \tag{23}$$

2. If we use the Green's functions defined in equations 1 and 2 the convolution becomes:

$$Conv_{1,2}^s(\omega) = \frac{1}{(4\pi)^2}\frac{1}{|\vec{r_s}-\vec{r_1}|}\frac{1}{|\vec{r_s}-\vec{r_2}|}\exp\left(\frac{i\omega}{c_0}(|\vec{r_s}-\vec{r_1}| + |\vec{r_s}-\vec{r_2}|)\right) \exp\left(\frac{-\omega c_i}{c_0^2}(|\vec{r_s}-\vec{r_1}| + |\vec{r_s}-\vec{r_2}|)\right) \tag{24}$$

3. Function $Conv_{1,2}(\omega)$ corresponds to one realization of the convolution function. However, we want to evaluate the convolution function over an ensemble of sources. We introduce

a sum for different sources. These sources have to have the same t0=0 in order to be used with convolution processsing. We need to work source after source.

$$Conv_{1,2}(\omega, \vec{r_s}) = \int_{\vec{r_s}} d\vec{r}_s \frac{1}{(4\pi)^2} \frac{1}{|\vec{r_s} - \vec{r_1}|} \frac{1}{|\vec{r_s} - \vec{r_2}|} \exp\left(\frac{i\omega}{c_0}(|\vec{r_s} - \vec{r_1}| + |\vec{r_s} - \vec{r_2}|)\right) \exp\left(\frac{-\omega c_i}{c_0^2}(|\vec{r_s} - \vec{r_1}| + |\vec{r_s} - \vec{r_2}|)\right) \tag{25}$$

4. We now perform a change of variable from the Cartesian coordinates to the hyperbolic coordinate system in order to solve the spatial integration in equation 25. The change of variable is exactly the same as for correlation function.

   Before we go further, we analyze a geometrical argument for convolutions. For the defined Cartesian coordinate system in Figure 1a, sources should satisfy: $|r_s - r_1| + |r_s - r_2| = ct$. For time satisfying condition $-2a \leq ct \leq 2a$ the sources have to line on an ellipsoid defined by the equation:

$$\frac{x^2}{(\frac{ct}{2})^2} + \frac{y^2}{\frac{(ct-2a)(ct+2a)}{4}} = 1 \text{ if } ct \neq 0 \tag{26}$$

   and: $x = 0$ if $ct = 0$. The ellipses in Figure 19 correspond to the sources in a 2D space that will contribute to $Conv_{1,2}(t)$ at a given time t.

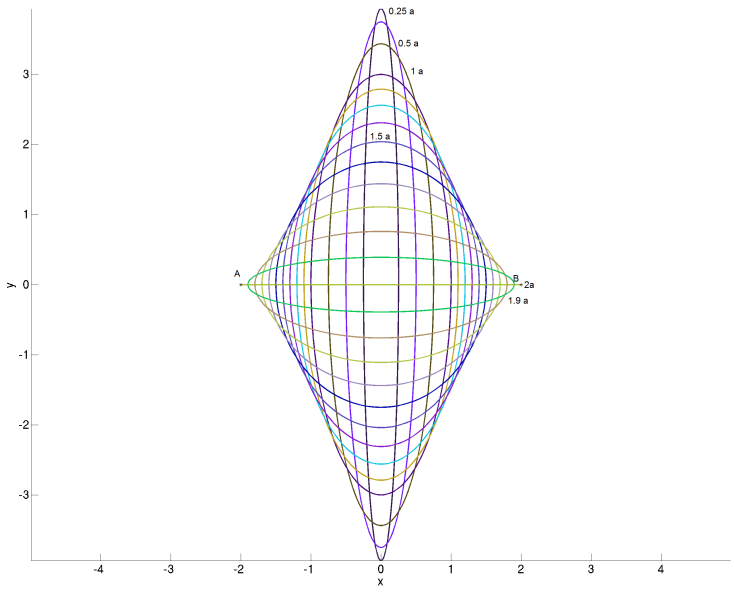

Figure 2: Representation in the xy plane of the ellipses that contribute to a given time t in the noise correlation function. On each ellipsoid, the sources satisfy $|r_s - r_1| + |r_s - r_2| = ct$. The line $y = 0$ corresponds to $ct = 2a$.The receivers 1 and 2 are at (-a,0) and (a,0).

5. We now go back to the equation 25. We perform a change of variable from the Cartesian coordinates to the hyperbolic coordinate system in order to do the spatial integration in equation:

$$Conv_{1,2}(\omega,\varphi,\theta,\psi) = \frac{1}{(4\pi)^2}\int_0^{\infty} d\varphi \int_{-\frac{\pi}{2}}^{\frac{\pi}{2}} d\theta \int_0^{2\pi} d\psi \; a\cos(\theta)\sin(\varphi)\exp\left(\frac{i\omega}{c_0}(2a\cosh(\varphi))\right) \exp\left(-\frac{\omega c_i}{c_0^2}(2a\cosh(\varphi))\right) \tag{27}$$

Now, we consider the integrals separately.

The integral over φ converges as:

$$\int_0^{\infty} d\varphi \sinh(\varphi)\exp\left(\frac{2a\,i\omega}{c_0}\cosh(\varphi)\right)\exp\left(-\frac{2a\,\omega c_i}{c_0^2}\cosh(\varphi)\right) = \left\{\begin{array}{c} x=\cosh(\varphi) \\ dx=\sinh(\varphi)d(\varphi)\end{array}\right\} = a\int_1^{\infty} dx \exp\left((\frac{2a\,i\omega}{c_0}-\frac{2a\,c_i\omega}{c_0^2})\,x\right) \tag{28}$$

Now, this integral converges towards:

$$\int_1^{\infty} dx \exp((ci-d)x) = \frac{\exp(d+ic)}{d-ic} \text{ for } \mathbb{I}(c)+\mathbb{R}(d)>0 \tag{29}$$

where: $c=\frac{2a\,\omega}{c_0}$ $d=\frac{2a\,c_i\omega}{c_0^2}$.

So, the integral 28 gives:

$$\int_0^{\infty} d\varphi \sinh(\varphi)\exp\left(\frac{2a\,i\omega}{c_0}\cosh(\varphi)\right)\exp\left(-\frac{2a\,\omega c_i}{c_0^2}\cosh(\varphi)\right) = \frac{1}{2}\frac{1}{i\omega}\frac{c_0^2}{-(ic_i+c_0)}\exp\left(\frac{2a\,i\omega}{c_0}-\frac{2a\,\omega c_i}{c_0^2}\right) \tag{30}$$

While the integrals over θ and ψ give:

$$\int_{\frac{-\pi}{2}}^{\frac{-\pi}{2}} d\theta\cos(\theta) = 2 \tag{31}$$

$$\int_0^{2\pi} d\psi = 2\pi \tag{32}$$

6. Finally, combining equations 30, 31, 32 it follows:

$$Conv_{1,2}(\omega) = -\frac{1}{(8\pi)}\frac{c_0^2}{c_0+ic_i}\frac{1}{i\omega}\exp\left(\frac{2a\,i\omega}{c_0}\right)\exp\left(-\frac{2a\,\omega c_i}{c_0^2}\right) \tag{33}$$

7. The convolution function in the time domain yields:

$$Conv_{1,2}(t) = -\frac{1}{2\pi}\frac{c_0^2}{c_0+ic_i}\frac{1}{8\pi}\int_{-\infty}^{\infty}\frac{d\omega}{i\omega}\exp\left(i\omega(t+\frac{2a}{c_0})\right)\exp\left(-\frac{2a\,\omega c_i}{c_0^2}\right) \tag{34}$$

8. The time derivate of the convolution functions reads:

$$\frac{d}{dt}Conv_{1,2}(t) = -\frac{1}{2\pi}\frac{c_0^2\ 2a}{c_0 + ic_i}\int_{-\infty}^{\infty} d\omega \frac{1}{8\pi}\frac{1}{2a}\exp\left(i\omega(t + \frac{2a}{c_0})\right)\exp\left(-\frac{2a\,\omega c_i}{c_0^2}\right) \tag{35}$$

This integral is proportional to the Green's function from 1 to 2 (equation 5). However, we observe a phase-shift depending on the attenuation before the integral. It means that the attenuation in the medium will influence the estimate of the Green's function. This mathematical development shows that the derivative of the active source convolution function gives an estimate of the causal Green's function between the two points at which signal has been recorded:

$$\frac{d}{dt}Conv_{1,2}(t) = -\frac{1}{2\pi}\frac{c_0^2\ 2a}{c_0 + ic_i}G_{12}(t) \tag{36}$$

Note, that correlation function does not require synchronized sources, however the convolution function exceeds the same t_0 of the sources. Also, the correlation function provides both causal and anticausal estimates of the Green's functions, while the convolution function provides an estimate of the causal Green's function.

Bibliography

K. Aki and P. G. Richards. *Quantitative Seismology, 2nd Edition*. University Science Books, 1980.

A. Bakulin and R. Calvert. Virtual source: new method for imaging and 4d below complex overburden. *74th Annual International Meeting, Society of Exploration Geophysicists, Expanded Abstracts*, page 2477–2480, 2004.

G. D. Bensen, M. H. Ritzwoller, M. P. Barmin, A. L. Levshin, F. Lin, M. P. Moschetti, N. M. Shapiro, and Y. Yang. Processing seismic ambient noise data to obtain reliable broad-band surface wave dispersion measurements. *Geophysical Journal International*, 169(3):1239–1260, 2008.

M. Born and E. Wolf. *Principles of Optics: Electromagnetic Theory of Propagation, Interference and Diffraction of Light(7th Edition)*. Cambridge University Press, 1999.

F. Brenguier, N. M. Shapiro, M. Campillo, A. Nercessian, and V. Ferrazzini. 3-D surface wave tomography of the Piton de la Fournaise volcano using seismic noise correlation. *Geophysical Research Letters*, 34:L02305, 2007. doi: 10.1029/2006GL028586.

S. Bussat and S. Kugler. Offshore ambient-noise surface-wave tomography above 0.1 hz and its applications. *Leading Edge*, 30(5):514–524, 2011.

M. Campillo and P. Roux. Seismic imaging and monitoring with ambient noise correlations. *Treatise on Geophysics (B. Romanowicz, A. Dziewonski Eds)*, pages 56–271, 2014.

M. Campillo, P. Roux, and N. M. Shapiro. *Using seismic noise to image and to monitor the Solid Earth: in Encyclopedia of Solid Earth Geophysics*. Springer, 2011.

J. Capon. High resolution frequency-wavenumber spectrum analysis. *Proceedings of the IEEE*, page 1408–1418, 1969. doi: 10.1109/PROC.1969.7278.

K. Chambers, J. M. Kendall, and O. Barkved. Investigation of induced microseismicity at Valhall using the Life of Field Seismic array. *The Leading Edge*, 29:290–295, 2010. doi: 10.1190/1.3353725.

S. S. Chen, D. L. Donoho, and M. A. Saunders. Atomic decomposition by basis pursuit. *SIAM Journal on Scientific Computing*, 20(1):33–61, 1999.

M. Chmiel, P. Roux, and T. Bardainne. Attenuation of Seismic Noise in Microseismic Monitoring from Surface Acquisition. *77th EAGE Conference and Exhibition 2015: Extended abstract*, 2015. doi: 10.3997/2214-4609.201413014.

M. Chmiel, P. Roux, and T. Bardainne. Extraction of phase and group velocities from ambient surface noise in a patch-array configuration. *Geophysics*, 81:1–10, 2016.

M. Corciulo, P. Roux, M. Campillo, D. Dubucq, and W. A. Kuperman. Multiscale matched-field processing for noise-source localization in exploration geophysics. *Geophysics*, 77:KS33–KS41, 2012. doi: 10.1190/geo2011-0438.1.

H. Cox. Spatial correlation in arbitrary noise fields with application to ambient sea noise. *Journal of the Acoustical Society of America*, 54:1289–1301, 1973.

H. Cox. Multi-rate adaptive beamforming (mrabf). *Sensor Array and Multichannel Signal Processing Workshop. 2000. Proceedings of the 2000 IEEE (2000)*, pages 306–309, 2000.

E. Cros, P. Roux, J. Vandemeulebrouck, and S. Kedar. Locating hydrothermal acoustic sources at Old Faithful Geyser using Matched Field Processing. *Geophysical Journal International*, 187: 385–393, 2011. doi: 10.1111/gji.2011.187.

A. Curtis, D. Nicolson, D. Halliday, J. Trampert, and B. Baptier. Source-receiver interferometry for seismic wavefield construction and ground-roll removal. *Nature Geoscience*, 2(10):700–704, 2009.

I. Das and M. D. Zoback. Long-period, long-duration seismic events during hydraulic stimulation of shale and tight-gas reservoirs — Part 1: Waveform characteristics. *Geophysics*, 78(6): KS107–KS118, 2013.

R. L. Davies, S. Mathias, J. Moss, S. Hustoft, and L. Newport. Hydraulic Fractures: How Far Can They Go? Marine and Petroleum Geology. *Marine and Petroleum Geology*, June, 2012. doi: 10.1016/j.marpetgeo.2012.05.010.

B. de Cacqueray, P. Roux, M. Campillo, S. Catheline, and P. Boué. Elastic-wave iden- tification and extraction through array processing : An experimental investigation at he laboratory scale. *Journal of Applied Geophysics*, 74:81–88, 2011.

S. de Ridder and J. Dellinger. Ambient seismic noise eikonal tomography for near-surface imaging at Valhall. *Leading Edge*, 30:506–512, 2011.

D. de Vos, H. Paulssen, and A. Fichtner. Finite-frequency sensitivity kernels for two-station surface wave measurements. *Geophysical Journal International*, 194:1042–1049, 2013. doi: 10.1093/gji/ggt144.

N. Deichmann and D. Giardini. Earthquakes induced by the stimulation of an enhanced geothermal system below Basel (Switzerland). *Seismological Research Letters*, 80:784–798, 2009. doi: 10.1785/gssrl.80.5.784.

L. Dorbath, L., K. Evans, N. Cuenot, B. Valley, J. Charléty, and Michel Frogneux. Seismic response of the fractured and faulted granite of Soultz-sous-Forêts (France) to 5 km deep massive water injections. *Geophysical Journal International*, 177:653–675, 2009.

D. Draganov, K. Wapenaar, W. Mulder, J. Singer, and A. Verdel. Retrieval of reflections from seismic background-noise measurements. *Geophysical Research Letters*, 34:L04305–1–L04305–4, 2007.

D. Draganov, X. Campman, J. Thorbecke, A. Verdel, and K. Wapenaar. Reflection images from ambient seismic noise. *Geophysics*, 74:A63–A67, 2009.

C. Duguid, Halliday D., and A. Curtis. Source-receiver interferometry for seismic wavefield construction and ground-roll removal. *The Leading Edge*, 30:838–843, 2011.

P. M. Duncan. Is there a future for passive seismic? *First Break*, 23(6):111–115, 2005.

F. Duret, F. Bertin, K. Garceran, R. Sternfels, T. Bardainne, N. Deladerriere, and D. Le Meur. Near-surface velocity modeling using a combined inversion of surface and refracted P-waves. *Leading Edge*, 35(3):946–951, 2016. doi: 10.1190/tle35110946.1.

C. Eckart. The theory of noise in continuous media. *Journal of the Acoustical Society of America*, 25:195–199, 1953.

L. Eisner, B.J. Hulsey, P.M. Duncan, D. Jurick, H. Werner, and W. Keller. Comparison of surface and borehole locations of induced seismicity. *Geophysical Prospecting*, 58:809–820, 2010. doi: 10.1111/j.1365-2478.2010.00867.x.

R. M. Errico. What Is an Adjoint Model? *Bulletin of the American Meteorological Society*, 78: 2577–2591, 1997.

D. M. Evans. The Denver Area Earthquakes and the Rocky Mountain Arsenal Disposal Well. *The Mountain Geologist*, 3:23–26, 1966.

J. F. Evernden. Precision of epicenters obtained by small numbers of world-wide stations. *Bulletin of the Seismological Society of America*, 59:1365–1398, 1969a.

J. F. Evernden. Identification of earthquakes and explosions by use of teleseismic data. *Journal of Geophysical Research*, 74:3828–3856, 1969b.

M. Ewing and F. Press. *Chapter, Geophysik I / Geophysics I in Encyclopedia of Physics*, volume 10/47. Seismic Prospecting, 1956. doi: 10.1007/978-3-642-45855-2_6.

H. Fang, H. Yao, H. Zhangs, and Y.-Ch. Huang. Direct inversion of surface wave dispersion for three-dimensional shallow crustal structure based on ray tracing: methodology and application. *Geophysical Journal International*, 201:1251–1263, 2015.

A. Fichtner, H.-P. Bunge, and H. Igel. Theoretical background for the inversion of seismic waveforms, including elasticity and attenuation. *Physics of the Earth and Planetary Interiors*, 157: 86–104, 2006.

J.-L. Got, J. Fréchet, and F. W. Klein. Deep Fault Plane Geometry Inferred from Multiplet Relative. *Journal of Geophysical Research*, 99(94):375–386, 1994.

P. Gouédard, P. Roux, M. Campillo, and A. Verdel. Convergence of the two-point correlation function toward the green's function in the context of a seismic-prospecting data set. *Geophysics*, 73:V47–V53, 2008a. doi: 10.1190/1.2985822.

P. Gouédard, L. Stehly, F. Brenguier, M. Campillo, Y. Colin de Verdière, E. Larose, L. Margerin, P. Roux, F. J. Sánchez-Sesma, N. M. Shapiro, and R. L. Weaver. Crosscorrelation of random fields: Mathematical approach and applications. *Geophysical Prospetcing*, 56:375–393, 2008b. doi: 10.1190/1.2985822.

V. Grechka, A. De La Pena, E. Schissele-Rebel, E. Auger, and P.-F. Roux. Relative location of microseismicity. *Geophysics*, 80(6):WC1–WC9, 2015. doi: 10.1190/geo2014-0617.1.

M. Guillouet, A. Berthaud, T. Bianchi, G. Pignot, S. Mahrooqi, and J. Shorter. Recovery of Blended data - A Sparse Coding Approach for Seismic Acquisition Normal access. *78th EAGE Conference and Exhibition 2016, Extended Abstract*, 2016.

M. Hallo. Microseismic Surface Monitoring Network Design - Sensitivity and Accuracy. *74th EAGE Conference and Exhibition incorporating EUROPEC 2012*, 2012. doi: 10.3997/2214-4609.20148336.

T. Hastie, R. Tibshirani, and J. H. Friedman. *The Elements of Statistical Learning*. Springer, 2001.

T. H. Heaton. Engineering Seismology Notes. `http://www.its.caltech.edu/~heatont/Eng_Seism_Notes/ch5_surfacewaves.pdf`, 2005.

D. Hohl and A. Mateeva. Passive seismic reflectivity imaging with ocean bottom cable data. *SEG Technical Program Expanded Abstracts 2006*, pages 1560–1564, 2006. doi: 10.1190/1.2369819.

F. B. Jensen, W. A. Kuperman, M. Porter, and H. Schmidt. *Computational Ocean Acoustics*. Springer, 2011.

V. Jones. Interaction of Radiation and Matter. `https://archive.org/details/flooved2930`, 2000.

H. Kao and S.-J. Shan. The source-scanning algorithm: Mapping the distribution of seismic sources in time and space. *Geophysical Journal International*, 157:589–594, 2004.

H. B. Koerner and J. C. Carrol. Use Of The Noise Log As A Downhole Diagnostic Tool. *Conference Paper: Middle East Technical Conference and Exhibition, 25-28 February, Bahrain*, 1979.

W. A. Kuperman and G. Turek. Matched field acoustics. *Mechanical Systems and Signal Processing*, 11:141–148, 1997. doi: 10.1006/mssp.1996.0066.

J. C. Lagarias, J. A. Reeds, M. H. Wright, and P. E. Wright. Convergence Properties of the Nelder-Mead Simplex Method in Low Dimensions. *SIAM Journal of Optimization*, 9(1):112–147, 1998.

J. D. Lakings, P. M. Duncan, C. Neale, and T. Theiner. Surface based microseismic monitoring of a hydraulic fracture well stimulation in the Barnett Shales. *SEG Technical Program, Expanded Abstracts, 605–608*, page 605–608, 2006. doi: 10.1190/1.2370333.

E. Larose, A. Derode, M. Campillo, and M. Fink. Imaging from one-bit correlation of wide-band diffuse wavefield. *IJournal of Applied Physics*, 95:8393–8399, 2004.

F. C. Lin, M. H. Ritzwoller, J. Townend, S. Bannister, and M. Savage. Ambient noise Rayleigh wave tomography of New Zealand. *Geophysical Journal International*, 170:649–666, 2007. doi: 10.1111/j.1365-246X.2007.03414.x.

F.-Ch. Lin and M. H. Ritzwoller. Empirically determined finite frequency sensitivity kernels for surface waves. *Geophysical Journal International*, 182:923–932, 2010. doi: 10.1111/j.1365-246X.2010.04643.x.

F.-Ch. Lin, M. H. Ritzwoller, and R. Snieder. Eikonal tomography: surface wave tomography by phase front tracking across a regional broad-band seismic array. *Geophysical Journal International*, 177(3):1091–1110, 2009. doi: 10.1111/j.1365-246X.2009.04105.x.

Q. Liu and J. Tromp. Finite-Frequency Kernels Based on Adjoint Methods. *Bulletin of the Seismological Society of America*, 96:2383–2397, 2006. doi: 10.1785/0120060041.

O. I. Lobkis and R. L. Weaver. On the emergence of the Green's function in the correlations of a diffuse field. *Journal of the Acoustical Society of America*, 110:3011–3017, 2001.

S. Maxwell. *Microseismic Imaging of Hydraulic Fracturing: Improved Engineering of Unconventional Shale Reservoirs*. Distinguished Instructor Series no 17, 2014. ISBN 978-1-56080-315-7.

S. C. Maxwell, M. Jones, D. Cho, and M. Norton. Understanding Hydraulic Fracture Variability Throught Integration of Microseismicity and Reservoir Characterization. *EAGE Extended Abstract: Third Passive Seismic Workshop –Actively Passive!, 27-30 March, 2011, Athens, Greece*, page PAS03, 2011.

A. Mordret, M. Landes, N. M. Shapiro, S. C. Singh, P. Roux, and O. I. Barkved. Near-surface study at the Valhall oil field from ambient noise surface wave tomography. *Geophysical Journal International*, ggt061, 2013. doi: 10.1093/gji/ggt061.

K. Nishida. Two-dimensional sensitivity kernels for cross-correlation functions of background surface waves. *Comptes Rendus Geoscience*, 343:584–590, 2011.

R. Nowack and W.-P Chen. Source-receiver reciprocity and empirical Green's functions from chemical blasts. *Bulletin of the Seismological Society of America*, 89(2):538–543, 1999.

B. Olofsson. Marine ambient seismic noise in the frequency range 1-10 Hz. *The Leading Edge*, 29:418–435, 2010. doi: 10.1190/1.3378306.

M. Pastori, M. Buia, A. Masciarelli, G. Tortini, F. Pradalié, T. Bianchi, H. Millet, S. Trabelsi, W. Oueslati, and P. Herrmann. Maximizing Information Content of Seismic Data through Optimized Acquisition Design - A Case History from South Tunisia. *EAGE Conference and Exhibition 2016 Vienna, Austria, 30 May – 2 June 2016 , Extended Abstract*, page We LHR4 02, 2016.

A. Paul and M. Campillo. Extracting the Green function between two stations from coda waves. *American Geophysical Union, Fall Meeting, Abstracts*, page D610, 2001.

D. Pei. *Modeling and inversion of dispersion curves of surface waves in shallow site investigations*. PhD thesis, University of Nevada, 2007.

M. Pollow. *Directivity Patterns for Room Acoustical Measurements and Simulations*. Logos Verlag Berlin GmbH, 2015.

J.-J. Postel, J. Meunier, and T. Bianchi. Reduced Vibroseis cycle time technique increases land crew productivity. *First Break*, 23(2), 2005.

P. Roux. Passive seismic imaging with directive ambient noise: application to surface waves and the San Andreas Fault in Parkfield. *Geophysical Journal International*, 179:367–373, 2009. doi: 10.1111/j.1365-246X.2009.04282.x.

P. Roux and M. Fink. Green function estimation using secondary sources in a shallow water environment. *Journal of the Acoustical Society of America*, 113(3):1406–1416, 2003.

P. Roux and W.A. Kuperman. Extracting coherent wavefronts from acoustic ambient noise in the ocean. *The Journal of the Acoustical Society of America*, 116:1995–2003, 2004.

P. Roux, K. G. Sabra, W. A. Kuperman, and A. Roux. Ambient noise cross-correlation in free space: theoretical approach. *Acoustical Society of America*, 117:79–84, 2005. doi: 10.1121/1.1830673.

P. Roux, A. Roueff, and M. Wathelet. The San Andreas Fault revisited through seismic-noise and surface-wave tomography. *Geophysical Research Letters*, 38:L13319, 2011. doi: 10.1029/2011GL047811.

P. Roux, C. Marandet, B. Nicolas, and W. A. Kuperman. Experimental measurement of the acoustic sensitivity kernel. *The Journal of the Acoustical Society of America*, pages EL38–EL44, 2013.

P. Roux, L. Moreau, A. Lecointre, G. Hillers, M. Campillo, Y. Ben-Zion, D. Zigone, and F. Vernon. A methodological approach towards high-resolution surface wave imaging of the San Jacinto Fault Zone using ambient-noise recordings at a spatially dense array. *Geophysical Journal International*, 206:980–992, 2016. doi: 10.1093/gji/ggw193.

P.-F. Roux, J. Kostadinovic, T. Bardainne, E. Rebel, M. Chmiel, M. Van Parys, R. Macault, and L. Pignot. Increasing the accuracy of microseismic monitoring using surface patch arrays and a novel processing approach. *First Break*, 32:95–101, 2014.

J. T. Rutledge and W. S. Phillips. Case history hydraulic stimulation of natural fractures as revealed by induced microearthquakes, Carthage Cotton Valley Gas Field, east Texas. *Geophysics*, 68:441–452, 2003.

K. G. Sabra, P. Gerstoft, P. Roux, W.A. Kuperman, and M. Fehler. Extracting time domain Green's function estimates from ambient seismic noise. *Geophysical Research Letters*, 32:L03310, 2005. doi: 10.1029/2004GL021862.

K. G. Sabra, A. Srivastava, F. L. di Scalea, I. Bartoli, P. Rizzo, and S. Conti. Structural health monitoring by extraction of coherent guided waves from diffuse fields. *Journal of the Acoustical Society of America*, 123:EL8–EL13, 2008.

F. J. Sanchez-Sesma, J. A. Perez-Ruiz, M. Campillo, and F. Luzon. Elastodynamic 2D Green function retrieval from cross-correlation: canonical inclusion problem. *Geophysical Research Letters*, 33(13):L13305, 2006. doi: 10.1029/2006GL026454.

J. Scales and R. Snieder. What is noise? *Geophysics*, (63):1122–1124, 1998.

M. Schmidt. Least Squares Optimization with L1-Norm Regularization, 2005.

G. T. Schuster, J. Yu, J. Sheng, and J. Rickett. Interferometric/daylight seismic imaging. *Geophysics*, 157:38–852, 2008.

N. M. Shapiro and M. Campillo. Emergence of broadband Rayleigh waves from correlations of the ambient seismic noise. *Geophysical Research Letters*, 31:L07614, 2004. doi: 10.1029/2004GL019491.

N. M. Shapiro and M. H. Ritzwoller. Monte-carlo inversion for a global shear velocity model of the crust and upper mantle. *Science*, 151:88–105, 2002.

N. M. Shapiro, M. Campillo, L. Stehly, and M.H. Ritzwoller. High-resolution surface-wave tomography from ambient seismic noise. *Science*, 307:1615–1618, 2005. doi: 10.1126/science.1108339.

P. M. Shearer. *Introduction to Seismology*. Cambridge, 2009.

R. E. Sheriff and L. P. Geldart. *Exploration Seismology, 2nd Edition*. Cambridge University Press, 1995.

E. Slob, D. Draganov, and K. Wapenaar. Interferometric electromagnetic Green's functions representations using propagation invariants. *Geophysical Journal International*, 169(1):60–80, 2007. doi: 10.1111/j.1365-246X.2006.03296.x.

R. Snieder. Extracting the Green's function from the correlation of coda waves: a derivation based on stationary phase. *Physical Review E*, 69, 2004. doi: 10.1103/PhysRevE.69.046610.

A. Tarantola. *Inverse Problem Theory*. 1987.

A. Tarantola. Theoretical background for the inversion of seismic waveforms, including elasticity and attenuation. *PAGEOPH (Pure and Applied geophysics)*, 128:365–399, 1988.

R. Tibshirani. Regression shrinkage and selection via the lasso, 1994.

J. Tromp, C. Tape, and Q. Liu. Seismic tomography, adjoint methods, time reversal and banana-doughnut kernels. *Geophysical Journal International*, 160:195–216, 2005.

J. Tromp, Y. Luo, S. Hanasoge, and D. Peter. Noise cross-correlation sensitivity kernels. *Geophysical Journal International*, 183:791–819, 2010.

H. J. van Heijst and J. Woodhouse. Measuring surface-wave overtone phase velocities using a mode branch stripping technique. *Geophysical Journal International*, 131:209–230, 1997.

J. Vandemeulebrouck, P. Roux, and E. Cros. The plumbing of Old Faithful Geyser revealed by hydrothermal tremor. *Geophysical Research Letters*, 40:1989–1993, 2013.

S. C. Walker. Coherence and interference in diffuse noise: On the information and statistics associated with spatial wave correlations in directional noise fields. *Journal of the Acoustical Society of America*, 131(3):1987–98, 2012.

K. Wapenaar. Retrieving the elastodynamic Green's function of an arbitrary inhomogeneous medium by crosscorrelation. *Physical Review Letters*, 93:254301–1– 254301–4, 2004.

K. Wapenaar. Nonreciprocal Green's function retrieval by cross-correlation. *Journal of the Acoustical Society of America*, 120(1):EL7–EL13, 2006.

K. Wapenaar, J. van der Neut, and E. Ruigrok. Passive seismic interferometry by multidimensional deconvolution. *Geophysics*, 73:A51–A56, 2008.

K. Wapenaar, D. Draganov, R. Snieder, X. Campman, and A. Verdel. Tutorial on seismic interferometry: Part 1 — Basic principles and applications. *Geophysics*, 75:A195–A209, 2010. doi: 10.1190/1.3457445.

M. Wathelet, D. Jongmans, and M. Ohrnberger. Surface wave inversion using a direct search algorithm and its application to ambient vibration measurements. *Near Surface Geophysics*, 2: 211–222, 2004.

R. L. Weaver. Information from seismic noise. *Science*, 307:1568–1569, 2005.

R. L. Weaver and O. I. Lobkis. Ultrasonics without a source: Thermal fluctuation correlations at MHz frequencies. *Physical Review Letters*, 87:134301, 2001.

R. L. Weaver and O. I. Lobkis. Fluctuations in diffuse field correlations and the emergence of the Green's function in open systems. *The Journal of the Acoustical Society of America*, 117: 3432–3439, 2005.

R. J. Wombell, R. Smith, P. Zwartjes, T. van Dijk, N. Benjamin, T. Wah Hong, O. Khakimov, R. Cramp, A. McCarthy, and M. Bulteau. South Oman Salt Basin - High-Density Wide-Azimuth, Land Seismic Acquisition and Processing. *EAGE Subsalt Imaging. Workshop: Focus on Azimuth, Cairo, Egypt. Expanded abstracts*, 2009.

J. H. Woodhouse and Y. K. Wong. Amplitude, phase and path anomalies of mantle waves. *Geophysical Journal International*, 87:753–773, 1986. doi: 10.1111/j.1365-246X.1986.tb01970.x.

Y. Yang and D. W. Forsyth. Regional tomographic inversion of the amplitude and phase of Rayleigh waves with 2-D sensitivity kernels. *Geophysical Journal International*, 166: 1148–1160, 2006. doi: 10.1111/j.1365-246X.2006.02972.x.

K. Yoshizawa and B. L. N. Kennett. Determination of the influence zone for surface wave paths. *Geophysical Journal International*, 149(2):440–453, 2002.

C. J. Young, E. P. Chael, M. M. Withers, and R. C. Aster. A comparison of the highfrequency (>1 Hz) surface and subsurface noise environment at three sites in the United States. *Bulletin of the Seismological Society of America*, (86):1516–1528, 1996.

0. Zhebel and L. Eisner. Simultaneous microseismic event localization and source mechanism determination. *Geophysics*, 80(1):KS1–KS9, 2014.

Y. Zhou, F. A. Dahlen, and G. Nolet. Three dimensional sensitivity kernels for surface wave observables. *Geophysical Journal International*, 158:142–168, 2004.